Università degli Studi di Trieste

XXV Ciclo del Dottorato di Ricerca in Fisica

In search of selective excitations for studying out-of-equilibrium properties in strongly correlated electron systems and high temperature superconductors

Settore scientifico-disciplinare: FIS/03

Dottorando

Fabio Novelli

Coordinatore

Prof. Paolo Camerini

Supervisore

Prof. Fulvio Parmigiani

Co-Supervisore

Dr. Daniele Fausti

Anno Accademico 2011/2012

Contents

Chapter 1

Introduction

The beloved Italian actor Massimo Troisi once said that he was not able to read all the good books, because he was only one reader against a multitude of writers. A physicist approaching the problem of high temperature superconductivity can easily feel the same.

The phenomenon of superconductivity was discovered in 1911 by Kamerlingh Omnes: the electrical resistance of mercury drops to zero below $4.2\,K$. In the following years the superconducting phase has been identified in other metallic elements and alloys, and a variety of experiments were performed both to unravel the fundamental physical mechanisms and to search for innovative applications. In 1957 Bardeen, Cooper, and Schrieffer formulated a theory capable to explain the superconducting phenomena so far observed. In particular, the superconductivity originates from an effective attractive interaction, mediated by phonons, between electrons and the consequent formation of pairs, that condense in the bosonic sense below a sufficiently low critical temperature T_C[1]. Besides offering an elegant and comprehensive framework, the BCS theory imposes a fundamental limit to the value of T_C of few tens of Kelvin and the dream of room temperature superconductivity seemed doomed. Nontheless, superconductors based on copper oxide compounds with critical temperatures higher than the liquid nitrogen one were discovered in 1986[2]. After 26 years[3], the high temperature superconductivity phenomena remain an essentially unsolved problem[4].

The copper-oxide based high temperature superconductors (HTSC) are obtained by "doping" selected parent compounds, characterized by crystal structures with $Cu-O$ planes separated by insulating layers. Single particle band theory predicts that an incomplete electronic shell, as the d shell of the copper in the cuprates, develops into an half filled band, i.e. in a metal. On the contrary, the parent compounds of the cuprates are electrical insulators with a gap of few eV. This is due to the strong electron-electron interaction that opens a gap in the density of states and the material turns into an insulator (Mott-Hubbard insulator). In particular, the cuprates are insulators of "charge-transfer" (CT). The electronic excitation at low energy involves a

transfer of charge between distinct lattice sites, i.e. from the ligand (oxygen) to the metal (copper).

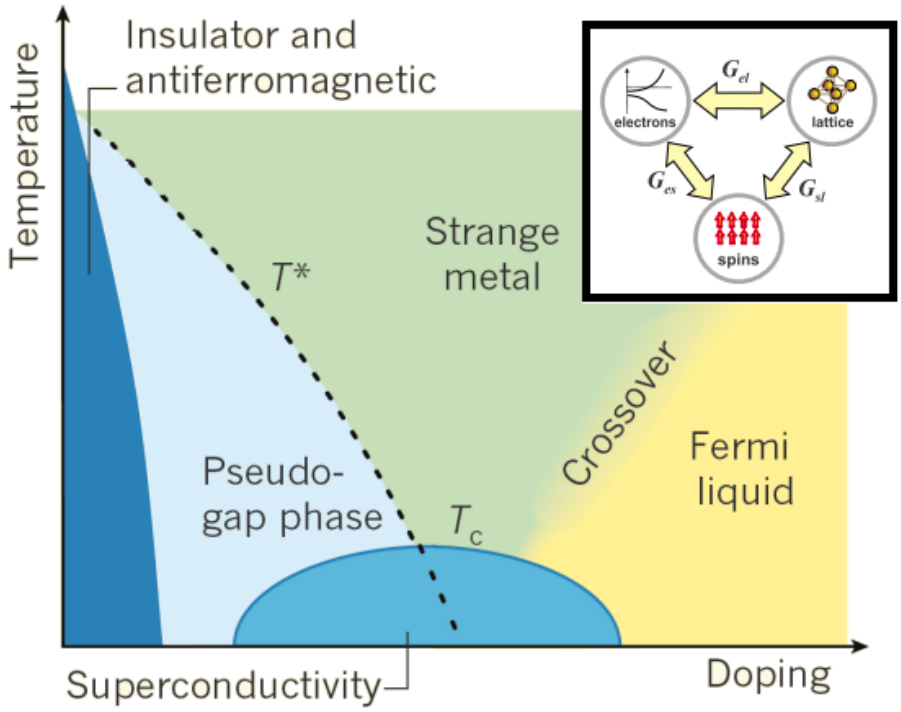

Figure 1.1: Simplified phase diagram of the cuprates upon doping the parent Mott-insulating compound. Insert: pictorial view of the interacting degrees of freedom. Adapted from [5] and [6].

The typical phase diagram of the cuprates plots the hole doping on the x axis, the temperature on the y axis (Fig.1.1). The parent compound is found at zero doping, is a CT insulator, and displays anti-ferromagnetic order below a certain temperature. For low dopings the insulating phase is replaced by a "strange metal"[1] at high temperature, by the "pseudo-gap phase" at intermediate temperatures ($T_C < T < T^*$), and by the superconducting phase below T_C. Besides being conductive, the pseudo-gap phase displays a depression in the optical conductivity at low frequency, related to a partial or incomplete gap in the density of states[7]. At higher dopings the pseudo-gap phase disappears, replaced by a metallic phase at high temperature and a superconducting phase below T_C. This region of the phase diagram, called "overdoped", is qualitatively explained with simpler theoretical models that accounts for weak effects of electronic correlation[7, 8]: the metal shows Fermi-liquid behavior, while the superconducting phase is BCS-like[4, 8].

The cuprates are only one family of strongly correlated electrons systems

[1]By strange metal we intend a bad conductor whose properties cannot be properly described starting from the single particle band theory. This is due to the strong electrons correlation.

(SCES). In general, SCES display rich phase diagrams with competing phases such as the metallic, insulating, and superconducting ones in the cuprates. The phase diagrams of SCES are the result of the complex interaction between the electronic, vibrational, and magnetic degress of freedom within the material (see insert in Fig.1.1). These different "baths" of electrons, phonons, and magnons respond to the external stimula with different characteristic timescales[9].

In this thesis we studied SCES by ultra-fast laser-based spectroscopy resolved in time and energy. The spectral content of the laser pulses used here has been manipulated through non-linear optical effects, allowing to perform optical experiments with pulses either in the THz, NIR, or visible range.

Time-resolved studies are performed through the "pump-probe" technique. In a pump-probe experiment an intense laser pulse ("pump") is used to drive the material out of equilibrium, and another weak pulse ("probe") detects how the system recovers its equilibrium optical properties as a function of the time delay between the pump and the probe pulses.

In simple systems the effects of the pump consist in the ultra-fast heating of the material: the pump pulses photo-excite electric dipoles that leave the electronic subsystem in an excited state, which subsequently dissipate the excess energy into lattice vibrations. In this framework the pump-probe technique is used to perform "quasi-equilibrium" studies, i.e. to obtain information on the ground state of the material by separating in the time-domain the different contribution of the quasi-particles involved.

However, it is also possible to selectively populate (deplete) a particular electronic state. This could bring the system in a metastable state not thermally accessible. The basic idea is to drive the phase transformation by means of ultra-short light pulses impulsively injecting a large number of excitations. The photo-excitation within time windows shorter than the characteristic relaxation times drives the matter into highly "off-equilibrium" transient regimes characterized by anomalous energy distribution between electrons, ions, and spins. This can strongly perturb the interaction among the different degrees of freedom and can thereby result in the formation of metastable "phases" not always accessible through thermodynamic transformations.

Transition metal oxides (TMOs) have a central role in the field of photo-induced phase transitions. The rich phase diagram of many TMOs is, in general, the result of an intricate interplay among electrons, phonons, and magnons that often makes TMOs very sensitive to the fine tuning of parameters such as the pressure, the magnetic field, the temperature, and the doping[10]. The same sensitivity makes TMOs the ideal playground to design experiments where the interactions between ultra-short light pulses and matter can trigger the formation of transient phases with specific, sometimes exotic, physical properties.

In order to study the selective excitation mechanisms in TMOs, we adopted time-resolved techniques that combine broadband probes in the visible range

with either optical or far-infrared pumps (Ch.4). Such long wavelength pump pulses have been extensively employed to trigger selective excitations, as will be discussed in Ch.2. The time evolution of the electronic degree of freedom has been studied in details by means of broadband optical probes (Ch.3).

In particular, the puzzling optical properties of the Mott insulator YVO_3 (Ch.5) have been clarified by time-resolved optical experiments based on white-light probe and $1.65\,eV$ pump. A novel quasi-bound excitonic Hubbard excitation named Hubbard exciton has been identified. These results represent, to our knowledge, the first direct measurement of a kinetic energy based transition in strongly correlated electrons systems.

In a different set of time-resolved experiments the dynamics of the charge-transfer edge in the parent compound of $La_{2-x}Sr_xCuO_4$ has been unveiled (Ch.6). We proved that pumps in the extrema of the optical range ($1\,eV$ or $3\,eV$) can induce different optical responses in the La_2CuO_4. This result, if confirmed, calls for the revision of many optical pump-probe experiments on HTSC, where the pump effects are simply treated as ultra-fast heating of the electronic bath.

Furthermore, we have performed time-resolved optical experiments on optimally doped YBCO focused to address the problem of the interacting electronic and vibrational baths (Ch.7). These experiments proved that the Ba and the Cu vibrational modes, at THz frequencies, are coupled in a different way to the superconducting condensate. The Cu mode is independent whereas the Ba mode is intimately related to the thermal or photo-excited population of Cooper pairs.

In the last chapter, we study the mixed regime of matter-light interaction in GaAs through THz pump and broadband probe spectroscopy. We detect a novel regime of quasi-saturation of the dynamical Franz-Keldysh effect, where "memory" effects are surprisingly important (Ch.8). We suggest that this novel regime will be of relevance for ultra-fast optical gating devices.

Chapter 2

State of the art

In this chapter we will briefly review the state of the art of selective excitations in strongly correlated electronic systems by means of time-resolved optical experiments. At first we will introduce the time-resolved studies and recall some noticeable experiments where free charges are excited by light pulses. Hence, we will browse through the vibrational control of material properties, and introduce the non-equilibrium phenomena.

2.1 Time-resolved studies of strongly correlated electronic systems

Transition metal oxides (TMOs) are the prototype of strongly correlated electrons systems. The complex interactions between the electronic, vibrational and magnetic degrees of freedom are responsible for the rich phase diagram of many TMOs. The phase diagram of the cuprates, shown in Fig.2.1, is probably one of the most cited among TMOs. Strongly correlated electrons systems can be qualitatively described with the help of a simple model containing separate, but interacting, reservoirs or baths[6, 9], i.e. electrons, lattice, and spins (insert in Fig.2.1). These reservoirs are connected by interactions of different nature and effciency. As different baths interact on different timescales[6], time-resolved experiments have been extensively exploited to study the different contribution of each degree of freedom to the transient response of the system[9].

In a naive picture, the TMOs display complex free energy surfaces vs. the populations of electronic, vibrational or magnetic energy levels. This is sketched on the left in Fig.2.2. Time-resolved experiments can be used to study both the quasi-equilibrium state of the system or photo-induce phase transition into metastable non-thermal phases. In quasi-equilibrium studies the system is weakly perturbed, and the temporal evolution towards the equilibrium state allows to study the different baths. Moreover, after the ultra-fast excitation of quasi-particles, the matter can be driven into transient states with physical

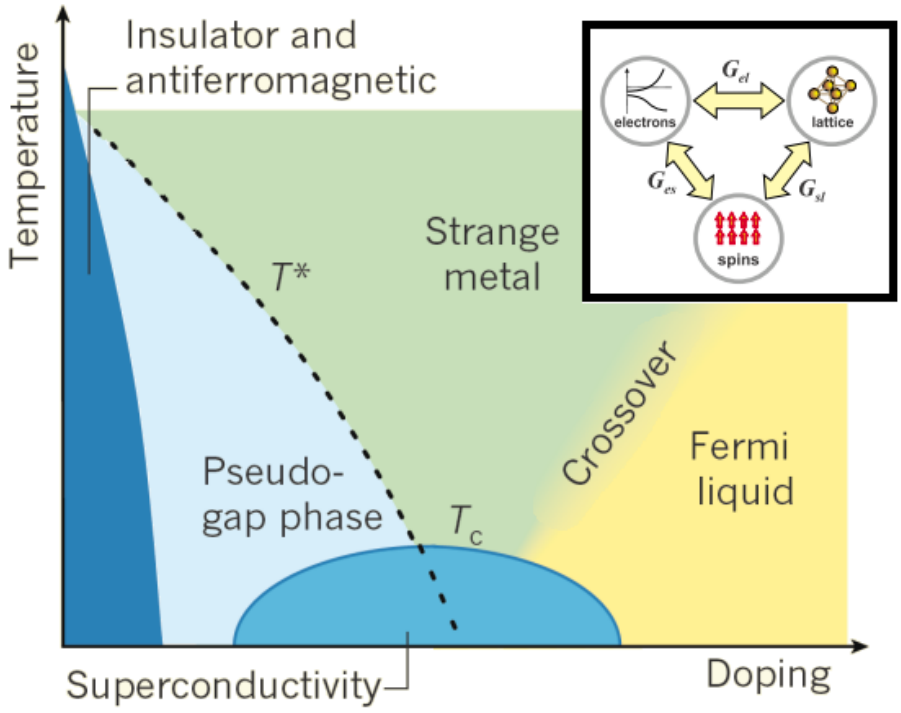

Figure 2.1: Simplified phase diagram of the cuprates upon doping the parent Mott-insulating compound. Insert: pictorial view of the interacting degrees of freedom. Adapted from [5] and [6].

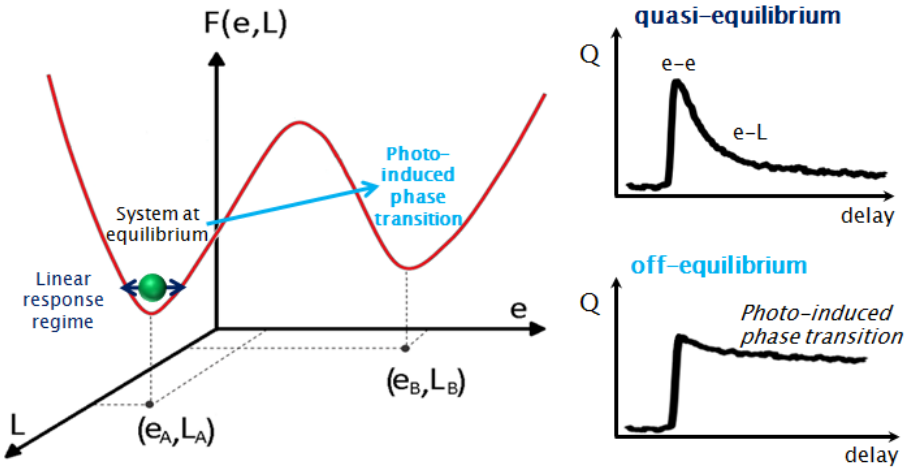

Figure 2.2: Pictorial view of quasi-equilibrium and off-equilibrium pump-probe studies. Left: energy surface of a strongly correlated electrons system as a function of electronic and lattice baths. On the right the temporal evolution of the physical quantity Q associated to the system under investigation is reported. Top right: quasi-equilibrium studies, performed for "weak" pump perturbation. Bottom right: photo-induced non-thermal phase transition, obtained by proper photo-irradiation.

properties possibly different than the equilibrium ones. Such metastable phases can be accessed on the ultra-fast timescale, while their relaxation is dominated by the thermalization processes among the electronic, vibrational and magnetic degrees of freedom.

Most of the studies dedicated to address the role of the different degrees of freedom in determining the equilibrium physical properties are performed in the so-called "linear regime". By linear regime we indicate quasi-equilibrium studies performed for pump pulses that induce variations in the response of the system that are linear with the pump intensity. A typical result of such an experiment is shown in Fig.2.3, where a physical parameter Q, that maps the time-evolution of the response of the system, exhibits different dynamics as a function of the pump-probe delay time. These dynamics are representative of the interaction timescales of the different degrees of freedom. For example an EM field interacts first with the electrons inducing then the electron-electron (e-e) and electron-lattice (e-L) interactions along with, on longer time scale, the lattice thermalization (L)[9] (Fig.2.3).

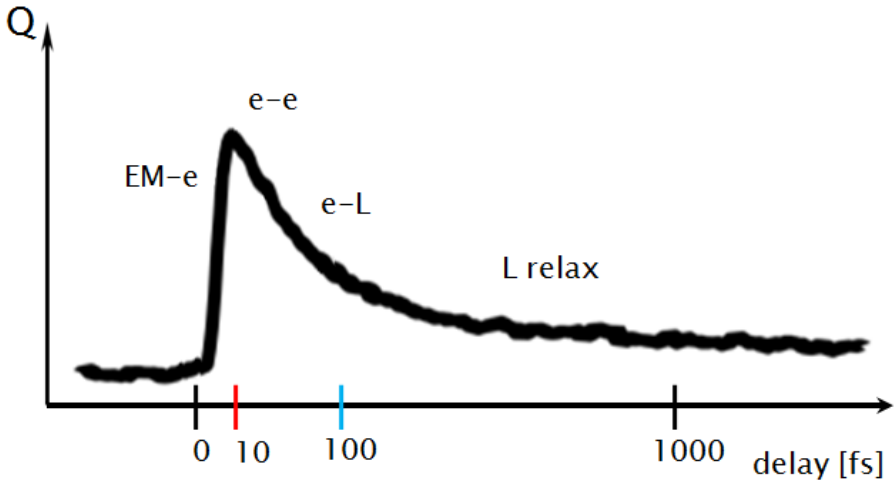

Figure 2.3: Sketch of the temporal evolution of the physical quantities of a strongly correlated electron system after "weak" pump perturbation (quasi-equilibrium studies).

As shown in Fig.2.1, the phase diagrams of TMOs are characterized by competing phases, such as antiferro- and para-magnetic, or metallic and insulating. These phases are accessible for example by the fine tuning of pressure, magnetic field, temperature, or doping[10]. Hence, the proper tailoring of the pump pulses may drive transformations among the competing phases, or even inducing metastable states not accessible adiabatically. The non-equilibrium regime lies above a treshold fluence and the transient respose is highly non-linear, in contrast to quasi-equilibrium processes. A large number of experiments show the possibility to change the physical properties of TMOs on ultra-fast timescales by photo-exciting the free carriers. A vast variety of transient metastable phases has been reported ranging through the non-thermal structural phases in cuprates[11], transport phase transition in manganites and

V-based oxides[12–14], till the non-thermal suppression of superconductivity in the cuprates[15–18].

We have performed several time-resolved measurements on strongly correlated electrons materials. In particular, on both quasi-equilibrium phases and selective excitation mechanisms. In the following of this chapter we will review part of the literature on selective excitations and phase control in optical pump-probe experiments.

2.2 Vibrational control of material properties

Near- and far-infrared electromagnetic pulses can directly couple to the low energy phonon modes of the crystals driving the atoms far from their equilibrium states. This large field-driven distortion can lead to significant changes of the electron correlation and, thereby, to the formation of different electronic ground states.

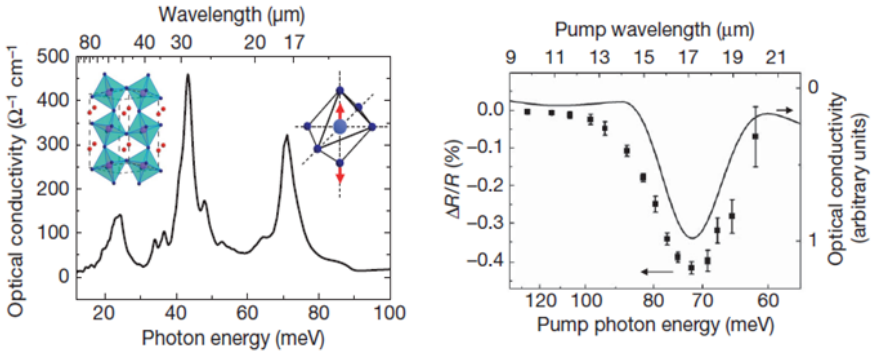

Figure 2.4: The resonant excitation of the $Mn-O$ stretching mode results in massive changes of the electronic properties[19].

In a seminal paper, Rini et al.[19] revealed that the resonant excitation of a $Mn-O$ stretching mode can lead to the formation of a metallic state in insulating $Pr_{0.7}Ca_{0.3}MnO_3$ (PCMO). As shown in Fig.2.4 this work gave the first experimental evidence of optical control of the electronic properties by field driven vibrational excitation. The resonant excitation of the $Mn-O$ stretching mode reduces the degree of distortion of the crystal, therefore increasing the width of the electronic band. This result, in turn, brings an effective reduction of the electronic correlations leading to the formation of a metallic phase, whereas at equilibrium $Pr_{1-x}Ca_xMnO_3$ is insulating for all dopings, i.e. for all the x values. With a similar excitation scheme Tobey et. al. achieved the non-thermal melting of the orbital order in $La_{0.5}Sr_{1.5}MnO_4$[20].

The important message brought across by these pioneering works is that the electronic ground state of solids, whose properties are dominated by strong electronic correlation, can sometimes be controlled by selective vibrational excitation.

2.3 Non-equilibrium high-temperature superconductivity

Among TMOs the most intriguing properties are shown by the family of the cuprates, where the formation of collective quantum states, such as superconductivity, has been reported for temperature up to $150\,K$. So far, the superconducting phase has been widely studied at equilibrium, mainly through optical spectroscopy[21], angle-resolved photoemission[2] and STM techniques[22], obtaining important but non-conclusive results. Detailed reviews on the equilibrium studies on HTSC can be found elsewhere[2, 7, 8, 23–25], while we focus here to the non-equilibrium studies.

Ultra-fast laser sources, producing sub $100\,fs$ light pulses, have been exploited to investigate the physics of HTSC in the non-equilibrium regime. In this regime, after the photo-injection of an excess of excitations, the free energy $F_{SC}(T, n)$ can be varied along non-equilibrium pathways by suddenly changing the number of excitations n. Conversely, for thermal phase transitions $n(T, \mu = E_{Fermi})$ is univocally determined by the Fermi-Dirac statistics[29].

As the superconducting gap is related to the total number of excitations, its impulsive suppression can be induced by ultra-short light pulses photo-injecting an excess of free quasi-particles. Even though in a BCS-like scenario we expect no effects of the suppression of the superconducting gap for the optical properties at few eV[1], the transient optical response in $BSCCO$[30] and $YBa_2Cu_3O_{6.5}$[31] reveal strong discontinuities across the superconducting transition. Only recent measurements of the optical conductivity in a broad energy range $(1.3 - 2\,eV)$ allowed to draw a more complete picture of the optical properties as they evolve in the time domain. In these studies the relatively high-energy electronic excitations, involved in the onset of superconductivity, were identified and a crossover of the response between the underdoped and overdoped regions has been found[26] (Fig.2.5a). More recently, the formalism describing the generic interaction of fermionic quasi-particles with bosonic excitations by means of the so-called bosonic function has been extended to non-equilibrium systems and, in combination with broadband time domain experiments, the contributions of the the electronic and phononic glues to the formation of the Cooper pairs has been disentangled[27]. To be fair, we want to recall that P.W. Anderson thinks that the concept of glue is capable to account for HTSC as well as a small mouse is capable to hold two elephants in a fridge[32].

In addition to the quasi-equilibrium properties studied by low fluence excitation, a threshold to induce an instability of the superconducting phase has been identified in the density of photo-excitations in $Bi_2Sr_2Ca_{1-y}Dy_yCu_2O_{8+\delta}$ (Fig.2.5b)[17] and $La_{2-x}Sr_xCuO_4$(Fig.2.5c)[16]. Above the threshold, a non-

[1] In the formation of a condensate a fraction of the spectral weight "falls" into a delta at zero frequency. In a BCS scenario all the spectral weight going into the condensate is taken from energy scales comparable to the energy of the superconducting gap.

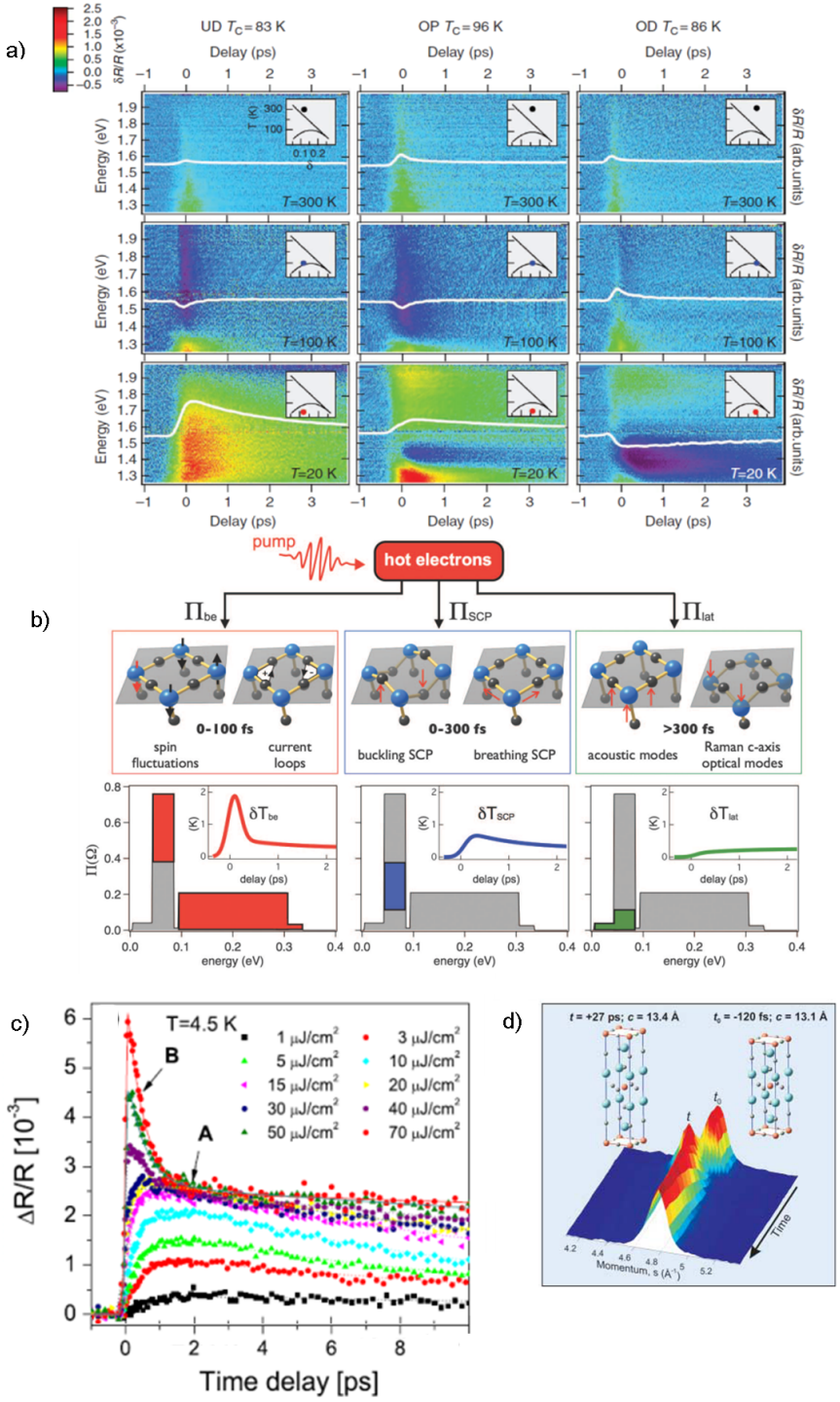

Figure 2.5: (a) Studies of the transient reflectivity in the low excitation limit across the superconducting phase[26] and (b) at room temperature[27]. Photo-induced melting of the superconducting phase[16] and structural transitions studied by electron diffraction in the high fluence limit (c,d)[11, 28].

thermal phase transition from the superconducting state to a new metastable one is induced on the *ps* timescale. At even higher fluence, electron diffraction studies have revealed the presence of a structural distortion possibly related to the formation of Cooper pairs[11, 28].

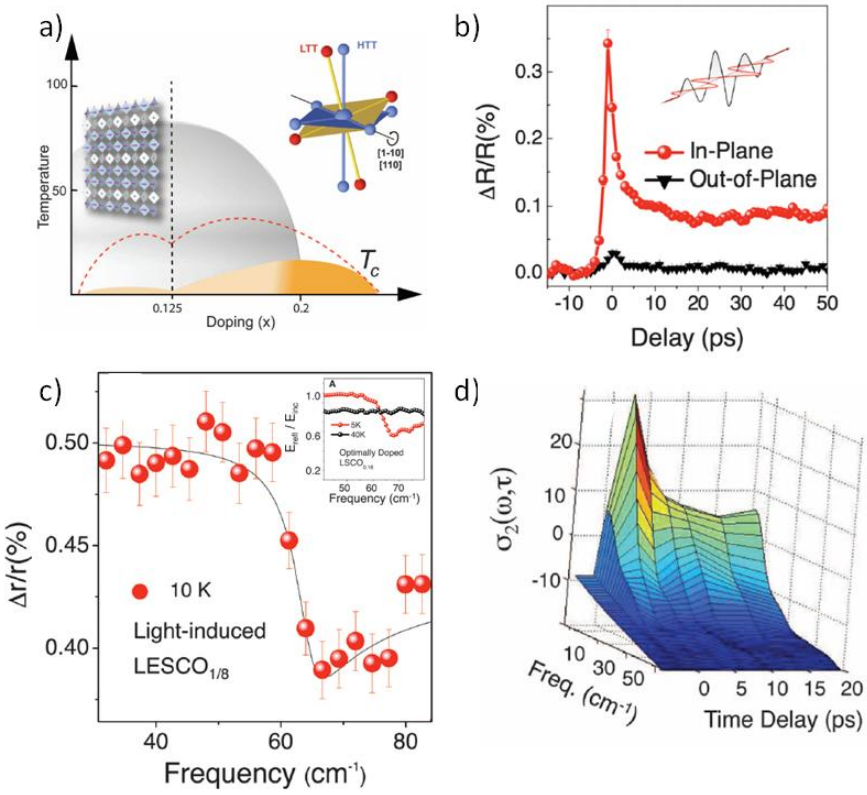

Figure 2.6: The resonant excitation of the $Cu-O$ phonon mode in non-superconducting stripe-ordered LESCO (a) results in the ultrafast formation a superconducting state. The metastable phase is achieved only with resonant in-plane excitation (b). The insert of (c) shows the response of optimally doped $La_{1.84}Sr_{0.16}CuO_4$ within the superconducting phase (red) and above the critical temperature (black). The resonance indicative of a superconducting behaviour appears in the photo-induced phase (main panel in (c)). The superconducting properties, indicated by a divergence in σ_2 at low frequency, appear within the experimental resolution of $2\,ps$ (d).

2.4 Phonon-driven formation of quantum coherent phases

Infrared pumps can perturb the vibrational or magnetic background without increasing significantly the electronic temperature. This gives the possibility of tailoring the properties of the baths that interact with the electrons and, hence, to trigger a change in the electronic ground state.

As shown in Fig.2.6, the resonant excitation of a $Cu-O$ stretching mode in non-superconducting stripe ordered $La_{1.675}Eu_{0.2}Sr_{0.125}CuO_4$ (LESCO) leads

to the formation of a new quantum coherent electronic ground state, resulting into a transient three-dimensional superconducting phase[33]. The emergence of coherent interlayer transport was evidenced by the appearance of a Josephson plasma resonance (JPR) in the c-axis optical properties[2]. Superconductivity emerges within the time resolution of the experiments, i.e. in less than 2 ps.

Making this evidence even more intriguing, recent reports indicate a tendency towards a quantum coherent state across all the pseudogap phases in underdoped YBCO[35]. A systematic study of the effects of similar excitations in the pseudogap phase in the cuprates could possibly lead to the formation of a superconducting state at ambient temperature[36]. A recent paper by Baskaran[37] offers a possible explanation, considering that the coherence of a THz pulse can be *transferred* into the non-condensed Cooper pairs above T_C, bringing the system into a metastable superconducting phase. This "superradiant theory"[37] opens to exotic new scenarios that require further studies.

2.5 Far infrared control of superconductivity

Rather than exploring the possibilities opened by the presence of competing phases, sub-gap infrared fields have been employed to manipulate the superconducting state directly. Intense THz pulses can force strong currents in optimally doped $La_{2-x}Sr_xCuO_4$, resulting in a modulation of the interlayer tunnelling. Ultra-fast oscillations between superconducting and resistive states have been obtained[38](Fig.2.7c and b).

At equilibrium, a fingerprint characterizing the superconducting state is given by the presence of a finite spectral weight[3] at nominally "0" frequency, which corresponds to a $1/\omega$ dependence in the imaginary part of the conductivity (σ_2) (Fig.2.7a, left panel). By applying an intense THz field it is possible to inhibit 3D superconductivity and induce oscillations between a resistive and superconducting response (Fig.2.7). This achievement paves the way to experiments where, by means of broadband probes, it will be possible to study the optical properties of the resistive phase "underneath" superconductivity and, allegedly, clarify the origin of the anomalous spectral weight transfer to high energy observed in the superconducting transitions in the cuprates[39].

The main message brought across by these results is that the interaction between a coherent electromagnetic field and electrons "in or about-to-form" a quantum coherent state can be used to manipulate their behaviour. Superconductivity could be induced in non-superconducting samples by means of vibrational excitation and inhibited by driving strong currents in the system.

Strating from several generation schemes, we developed FIR sources to be

[2]The JPR is a general feature of cuprate superconductors that is well understood by noting that the 3D superconductivity can be explained by Josephson coupling between capacitive coupled stacks of quasi two-dimensional superconducting layers[34].

[3]For the definition of spectral weight and other useful optical quantities see Ch.3.

used as pump pulses in time-resolved experiments (Ch.4). By combining THz pumps with boradband white-light probes, we measured the transient response of YVO_3, La_2CuO_4, $YBCO$, and $GaAs$ with phase-resolution over a broad energy range (Ch.8).

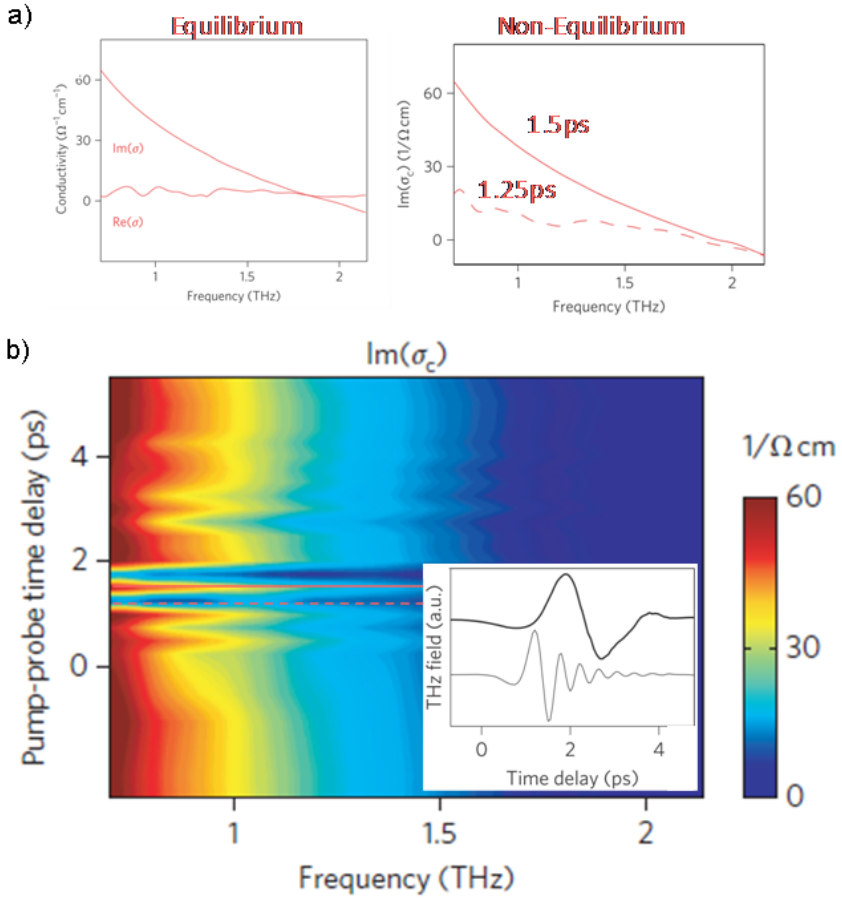

Figure 2.7: The superconducting response is indicated by the low frequency divergence of σ_2 (a) (left). The evolution of σ_2 as a function of the applied electromagnetic field is reported in (b): the main panel shows the low frequency response of σ_2, and the insert depicts the THz fields uses to pump and to probe the response. The figure (a) on the right shows two curves at $1.25\,ps$ and $1.5\,ps$.

Chapter 3

Differential optical properties

In this chapter we introduce the fundamental physical parameters governing the optical properties of the crystalline materials, along with the phenomenological models suitable to describe such quantities, and eventually the important physical relations that link the wanted information to the optical response of a system. These aims are achieved following two approaches suitable to extract information in the frequency and time domains.

3.1 Optical constants of solids

The macroscopic optical properties of a material are directly linked to the electronic degree of freedom of the system. In fact, from a microscopic point of view, an optical excitation originates from an electronic transition between the energy levels within the matter. The detailed knowledge of the optical response of the matter provides unique information about the underlying electronic structure. In the following, starting from the Maxwell's equations and a simplified solid medium, we will introduce the most relevant physical quantities describing the optical response of the medium, such as the conductivity, the index of refraction, the absorption coefficient, the penetration depth, the dielectric function, and the reflectivity.

The Maxwell's equations in a homogeneous and non-magnetic material with no external charges and currents are[1]

$$\begin{aligned} \nabla \cdot \boldsymbol{E} &= 4\pi\rho \\ \nabla \cdot \boldsymbol{B} &= 0 \\ \nabla \times \boldsymbol{E} &= -\frac{1}{c}\frac{\partial \boldsymbol{B}}{\partial t} \\ \nabla \times \boldsymbol{B} &= \frac{1}{c}\frac{\partial \boldsymbol{E}}{\partial t} + \frac{4\pi}{c}\boldsymbol{J} \end{aligned} \tag{3.1}$$

where ρ and $\boldsymbol{J}$ are, respectively, the internal charge density and the internal current density. Here, we consider a solution of this system of equations in

the form of transverse electromagnetic waves of given angular frequency ω propagating along z with electric field $\boldsymbol{E}(\boldsymbol{r},t) = E(z)e^{-i\omega t}$ and current density $\boldsymbol{J}(\boldsymbol{r},t) = J(z)e^{-i\omega t}$ along x, and with magnetic field $\boldsymbol{B}(\boldsymbol{r},t) = B(z)e^{-i\omega t}$ along y. Hence, $\nabla \cdot \boldsymbol{E} = 0$ and from eqs.3.1 we obtain

$$\frac{d^2E(z)}{dz^2} = -\frac{\omega^2}{c^2}E(z) - \frac{4\pi i\omega}{c^2}J(z). \tag{3.2}$$

When the average distance travelled by the carriers is small if compared to the extent of spatial variation of the electric field the "local-response" approximation holds[1]. In the local-response regime the current density at a given point of the material is equal to the value of the electric field at the same point multiplied by the complex frequency-dependent optical conductivity $\widetilde{\sigma(\omega)}$

$$J(z) = \widetilde{\sigma(\omega)}E(z). \tag{3.3}$$

Within this approximation, eq.3.2 can be recast as

$$\frac{d^2E(z)}{dz^2} = -\frac{\omega^2}{c^2}\left(1 + \frac{i4\pi\widetilde{\sigma(\omega)}}{\omega}\right)E(z). \tag{3.4}$$

This equation has a solution of the form $E(z) = E_0 e^{i\frac{\omega}{c}\widetilde{n(\omega)}z}$. $\widetilde{n(\omega)}$ is the complex refractive index, equal to $1 + \frac{i4\pi\widetilde{\sigma(\omega)}}{\omega}$, with the real part $n(\omega)$ that is the conventional refractive index and the imaginary part $k(\omega)$ that is the extinction coefficient. $k(\omega)$ is related to the penetration depth $\delta(\omega)$ of the radiation in the medium, defined as the distance at which the field amplitude is $1/e$ of the initial value. The absorption coefficient $\alpha(\omega)$ as function of $\delta(\omega)$ and $k(\omega)$ is given by

$$\alpha(\omega) = \frac{2}{\delta(\omega)} = \frac{4\pi k(\omega)}{\lambda}, \tag{3.5}$$

where λ is the wavelength of the electromagnetic radiation. The complex dielectric function of a material, $\widetilde{\epsilon(\omega)} = \epsilon_1(\omega) + i\epsilon_2(\omega)$, as obtained from the square of the index of refraction, is given by

$$\begin{cases} \epsilon_1(\omega) = n^2(\omega) - k^2(\omega) \\ \epsilon_2(\omega) = 2n(\omega)k(\omega) \end{cases} \tag{3.6}$$

Finally, the reflectivity $R(\omega)$ at normal incidence written as a function of the index of refraction or the dielectric function is

$$R(\omega) = \left|\frac{1 - \sqrt{\widetilde{\epsilon(\omega)}}}{1 + \sqrt{\widetilde{\epsilon(\omega)}}}\right|^2 = \frac{(n(\omega)-1)^2 + k^2(\omega)}{(n(\omega)+1)^2 + k^2(\omega)} \tag{3.7}$$

3.1.1 Lorentz model

The Lorentz model links the macroscopic optical quantities to the microscopic structure of the medium[1, 40]. Considering a bound electron with mass m and charge $-e$ subject to an elastic force, $m\omega_0^2\boldsymbol{r}$, and in the presence of an electric field $\boldsymbol{E}(\boldsymbol{r},t) = \boldsymbol{E}_0 e^{i(\boldsymbol{q}\cdot\boldsymbol{r}-\omega t)}$, the equation of motion is

$$m\frac{d^2\boldsymbol{r}}{dt^2} + m\Gamma\frac{d\boldsymbol{r}}{dt} + m\omega_0^2\boldsymbol{r} = -e\boldsymbol{E}(\boldsymbol{r},t), \tag{3.8}$$

where $m\Gamma\frac{d\boldsymbol{r}}{dt}$ is the term accounting for the radiation energy losses. If the displacements of the electrons are much smaller than the wavelength of the driving field (i.e. the local-response approximation holds), it can be shown[1] that the dielectric function is

$$\widetilde{\epsilon(\omega)} = 1 + \frac{\omega_P^2}{(\omega_0^2 - \omega^2) - i\Gamma\omega}, \tag{3.9}$$

where $\omega_P = \sqrt{\frac{4\pi Ne^2}{m}}$ is the plasma frequency and N the density of electrons. Note that the imaginary part of eq.3.9 is the well-known lorentzian function. Noteworthy eq.3.9 is consistent with the quantum mechanical results obtained for a bound single particle electronic structure[40, 41]. For the present case, ω_0 is the transition frequency of an electron between two bands separated by an energy $\hbar\omega_0$, while the plasma frequency can be directly related to the electric dipole transition matrix elements[41].

The Lorentz model describes not only the interband transitions but also the response of unbound charges perturbed by an electromagnetic field. By taking $\omega_0 = 0$ we obtain the so-called Drude term that describes the intraband contribution to the dielectric function. Hence, the dielectric function of a metal in the ground-state with M accessible bands can be modeled as

$$\widetilde{\epsilon(\omega)} = \epsilon_\infty - \frac{\omega_{P,0}^2}{\omega^2 + i\Gamma_0\omega} + \sum_{i=1}^{M}\frac{\omega_{P,i}^2}{(\omega_i^2 - \omega^2) - i\Gamma_i\omega} \tag{3.10}$$

where ϵ_∞ is a phenomenological parameter that accounts for the other bands or, equivalently, for the oscillators outside of the measured range. Obviously the same equation holds for an insulator, apart from the absent Drude term.

The extended Drude model

The Drude-Lorentz model has proven to be adequate to describe a vast number of experimental results on metals and insulators, and even on systems characterized by weak electron-electron interactions (i.e. Fermi liquids[7]) that are neglected in the derivation of eq.3.10. However, the Drude contribution to the dielectric function is often inadequate[42] for materials where the electronic

degree of freedom is coupled with some bosonic excitations, or where many-body effects are important. In order to describe these systems[43] the extended Drude model (EDM) introduces a complex frequency-dependent scattering rate

$$\widetilde{\Gamma(\omega)} = \Gamma(\omega) + i\omega\Lambda(\omega). \tag{3.11}$$

The real part of eq.3.11 takes into account the spectral distribution of the scattering centers, while the imaginary term describes the mass-enhancement of the charge-carriers due to many-body interactions ($\Lambda(\omega) = 1 - m^*(\omega)/m$). In the EDM the intraband contribution to the dielectric function is

$$\frac{\overline{\omega}^2_{P,0}(\omega)}{\omega^2 + i\overline{\Gamma}_0(\omega)\omega}, \tag{3.12}$$

with $\overline{\omega}^2_{P,0}(\omega) = \frac{\omega^2_{P,0}}{1-\Lambda(\omega)}$ and $\overline{\Gamma}_0(\omega) = \frac{\Gamma(\omega)}{1-\Lambda(\omega)}$: the main difference with respect to the Drude-Lorentz model is that the single lorentzian peak centered at $\omega = 0$ is substituted by an infinite set of lorentzians each one describing $\widetilde{\epsilon(\omega)}$ in the proximity of a particular frequency ω with scattering rate $\Gamma(\omega)$ and effective mass $m^*(\omega)$.

Other interband contributions

The Lorentz model predicts that the absorpion lineshapes of the interband transitions are lorentzian functions of the frequency. Quite often these functions fail to describe the optical response of the system. For example, in amorphous materials the gaussian functions are generally more suitable: in case of structural disorder[44] or inhomogenous environment[45], the random distribution of excitations around the main frequency leads to an optical response which is better described by the gaussian lineshape. As we will see in the next paragraph, the real and imaginary parts of the complex quantities that describe the optical response of a material are bound by the causality principle. In order to fulfill this requirement, when gaussian functions describe the imaginary part of the dielectric function, we must use a sum of Dawson's functions for $\epsilon_1(\omega)$[44]

$$\begin{aligned} \epsilon_1(\omega) &= \frac{2G}{\sqrt{\pi}}\left[D\left(\frac{2\sqrt{ln2}(\omega+\omega_G)}{\Gamma_G}\right) - D\left(\frac{2\sqrt{ln2}(\omega-\omega_G)}{\Gamma_G}\right)\right] \\ \epsilon_2(\omega) &= G\left(e^{-4ln2\frac{(\omega-\omega_G)^2}{\Gamma_G^2}} - e^{-4ln2\frac{(\omega+\omega_G)^2}{\Gamma_G^2}}\right) \end{aligned} \tag{3.13}$$

where $D(x) = e^{-x^2}\int_0^x e^{t^2}dt$ is the Dawson's function, G is the amplitude of the gaussian peak, Γ_G the width, and ω_G the central frequency.

A further lineshape used in the literature is the so-called Tauc-Lorentz, first introduced to address the bandgap of amorphous semiconductors[46]. This function is particularly useful in fitting the sharp absorption edge of some

largely debated transition metal oxides[47, 48] and, moreover, has the advantage to have a "*gap*" parameter that quantifies the threshold for optical excitations. The functional form of the Tauc-Lorentz oscillator is

$$\begin{gathered}\epsilon_2(\omega) = \frac{1}{\omega}\frac{A\omega_{TL}\Gamma_{TL}(\omega - gap)^2}{(\omega^2 - \omega_{TL}^2)^2 + \omega^2\Gamma_{TL}^2} \;\; if \;\; \omega > gap, \\ \epsilon_2(\omega) = 0 \;\; elsewhere,\end{gathered} \tag{3.14}$$

with A amplitude, ω_{TL} central frequency, and Γ_{TL} scattering rate. The Kramers Kronig consistent functional form for $\epsilon_1(\omega)$ has the Jellison's form and can be found in Ref.[49, 50].

3.1.2 The Kramers and Kronig transformations

Since $\widetilde{\epsilon(\omega)}$, $\widetilde{n(\omega)}$, $\widetilde{\sigma(\omega)}$ are causal response functions, i.e. characterize a system where the output depends only on past and instantaneous inputs, their real and imaginary parts are not independent but mutually related by the integral relations of Kramers and Kronig (KK)[40]. The Kramers-Kronig relations for the dielectric function $\widetilde{\epsilon(\omega)}$ are

$$\begin{aligned}\epsilon_1(\omega) &= \epsilon_\infty + \frac{1}{\pi}P\int_{-\infty}^{+\infty} d\omega' \frac{\epsilon_2(\omega')}{\omega' - \omega} \\ \epsilon_2(\omega) &= -\frac{1}{\pi}P\int_{-\infty}^{+\infty} d\omega' \frac{\epsilon_1(\omega') - \epsilon_\infty}{\omega' - \omega}\end{aligned} \tag{3.15}$$

where P is Cauchy's principal value.

Provided that the optical data are collected over a significant energy range and reasonable assumptions for the high and low energy tails are made (cfr. Appendix G p.249 of [40]), the KK integral relations represent a powerful tool. The KK allow to infer about both the real and the imaginary parts of the dielectric function from raw optical data. The causality relation between the amplitude $\sqrt{R(\omega)}$ and the phase $\rho(\omega)$ of the complex reflectivity $\widetilde{R(\omega)} = \sqrt{R(\omega)}e^{i\rho(\omega)}$ is

$$\rho(\omega) = \frac{\omega}{\pi}\int_0^\infty d\omega' \frac{ln[R(\omega')/R(\omega)]}{\omega^2 - \omega'^2}. \tag{3.16}$$

From $R(\omega)$ and $\rho(\omega)$ it is possible to obtain $\epsilon_1(\omega)$ and $\epsilon_2(\omega)$

$$\begin{aligned}\epsilon_1(\omega) &= \frac{(1 - R(\omega))^2 - 4R(\omega)sin^2\rho(\omega)}{1 + R(\omega) - 2\sqrt{R(\omega)}cos^2\rho(\omega)} \\ \epsilon_2(\omega) &= \frac{4(1 - R(\omega))\sqrt{R(\omega)}sin\rho(\omega)}{1 + R(\omega) - 2\sqrt{R(\omega)}cos^2\rho(\omega)}\end{aligned} \tag{3.17}$$

3.1.3 Sum rules

The response functions of any material obey numerous sum rules[7]. The f-sum rule for the optical properties of solids states that the indefinite integral of $\sigma_1(\omega)$, or equivalently of $\omega\epsilon_2(\omega)$, is a conserved quantity since the total charge is conserved

$$\int_0^\infty d\omega\omega\epsilon_2(\omega) = 4\pi \int_0^\infty d\omega\sigma_1(\omega) = \frac{\pi 4\pi N e^2}{2m} = \frac{\pi\omega_P^2}{2}. \tag{3.18}$$

The integral value is often called "spectral weight" or "oscillator strength".

In practice, the optical data are collected only over a limited range of wavelengths, hence the sum rules are frequently defined in terms of an effective frequency-dependent number of electrons[7, 40],

$$N_{eff}(\omega) = \frac{2m}{\pi e^2} \int_0^\omega d\omega'\sigma_1(\omega'), \tag{3.19}$$

which has the meaning of the effective number of electrons interacting with the electromagnetic field. For example, if the optical response of the system is characterized by two interband transitions, it is generally possibile to choose reasonable integration extrema in eq.3.19 and calculate the spectral weights, i.e. the number of carriers, associated to each band separately. However, in systems where quasi-free electrons dominate the optical properties in the form of intraband transitions, caution must be taken in chosing the frequency limit of the Drude component. This is particularly important in strongly correlated electrons systems where the zero-frequency Drude peak is suppressed and spectral weight is transferred to the "incoherent contribution" at higher energies[7].

The concept of spectral weight can be related to the kinetic energy of the charge carriers. For a single band system described within the tight-binding model[7, 51, 52], the total intraband spectral weight is proportional to the kinetic energy K_{band} of the carriers

$$\int_0^{\omega_c} d\omega\sigma(\omega) = -\frac{\pi e^2}{2\hbar^2} K_{band}, \tag{3.20}$$

where ω_c is the proper cutoff frequency for the free-electron response. In this framework the ratio of K_{exp}, obtained from optical data, over the kinetic energy K_{band}, calculated from band-structure models neglecting electronic correlations, can be used to quantify the "level" of electronic correlations within the system[7]. Fig.3.1 shows a classifications of materials based on this criterion: simple metals and Fermi liquids have $\frac{K_{exp}}{K_{band}} \approx 1$, while in strongly correlated systems the aforementioned incoherent peak is present and $\frac{K_{exp}}{K_{band}} << 1$ (Fig.3.1).

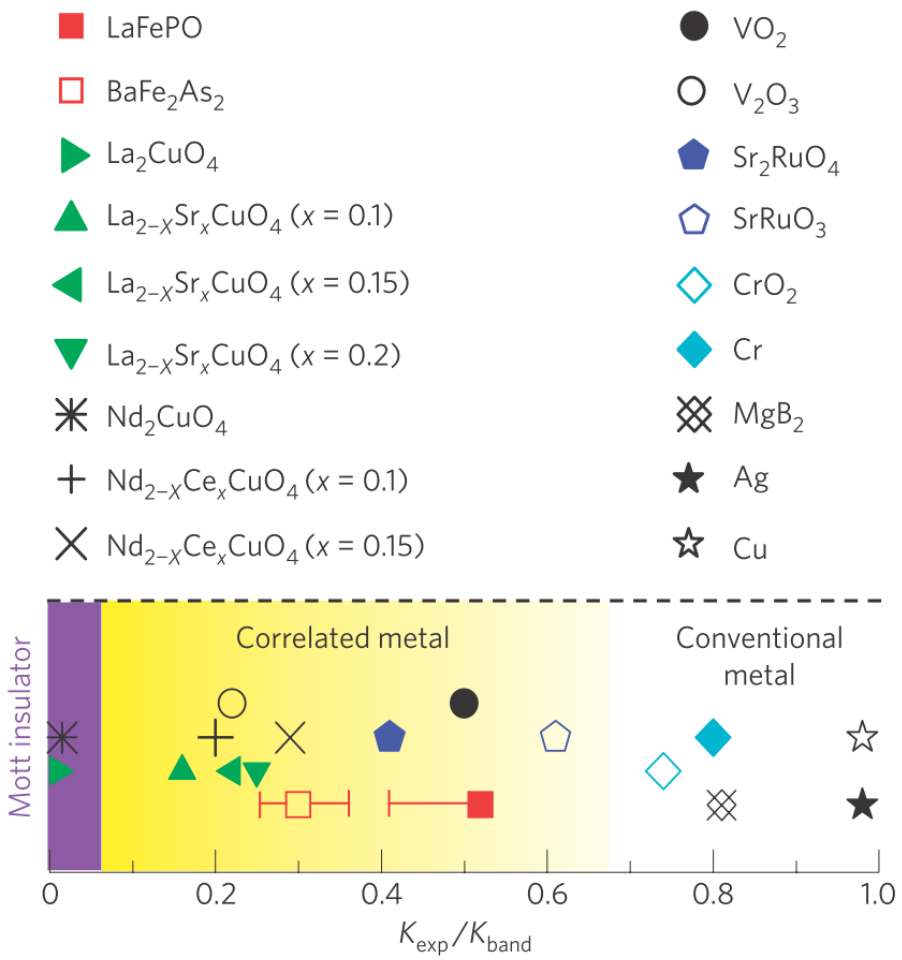

Figure 3.1: Ratio of the experimental kinetic energy K_{exp} and the kinetic energy from band theory K_{band} for various high-temperature superconductors (cuprates, pnictides), some simple metals, Mott insulators, and BCS superconductors. From [53].

3.2 Differential optical constants

Since the argument of this thesis is studying in the time and frequency domains the physics of materials driven far from equilibrium by ultra-short optical pulses, here we anticipate few time-dependent reflectivity measurements in order to introduce some basic concepts. A typical measurement is reported in Fig.3.2, where the x-axis is the time delay between the ultra-short pump and probe pulses, the y-axis is the energy of the probe, and the colour scales represent the amplitude of the pump-induced relative variation of the reflectivity $(R^*(\omega,t) - R_0(\omega))$ normalized to the static reflectivity $R_0(\omega)$, being $R^*(\omega,t)$ measured at the time delay t after photo-excitation.

In order to extract significant physical quantities, as the time-evolution of the spectral weight of each probed band, out of the time-resolved measurements we developed two approaches: i) the differential fit of the time domain data; ii) the Kramers-Kronig analysis. Both these approaches are based on the detailed knowledge of the static reflectivity $R_0(\omega)$. In the following, we will elucidate the two approaches making use of the time domain reflectivity measurements reported in Fig.3.2 on the parent compound of cuprates, La_2CuO_4.

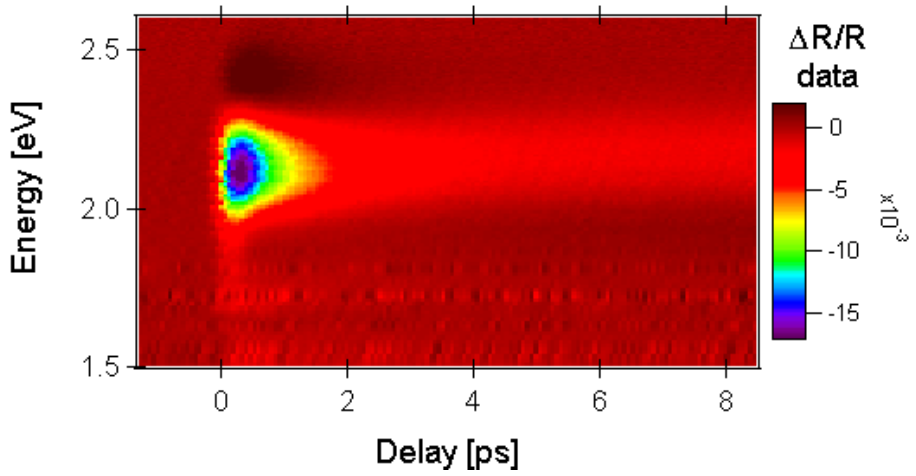

Figure 3.2: Typical $\Delta R/R$ data collected in our lab. Time-delay, probed energy and relative variations of the reflectivity at almost normal incidence are reported. This particular measurement has been performed at $130\,K$ on La_2CuO_4 with $\approx 400\,nm$ pump in the linear regime (for further details see Ch.6).

3.2.1 Differential fits

In this thesis we performed analysis of the transient reflectance data by means of differential Drude-Lorentz models. In order to proceed with the differential approach we first fit the static optical reflectivity. For La_2CuO_4 we matched the reflectivity data[48, 54] to obtain a static reflectivity $R_0(\omega)$ over a broad energy range $(0.01 - 12\,eV$, Fig.3.3). The reflectivity has been fitted using

one Tauc-Lorentz function and twelve Lorentz oscillators to describe the optical features in the IR-UV spectral range. Once the full set of parameters (central frequencies, amplitudes and lifetimes) describing the static optical properties are obtained, we duplicate the model for the static data and define

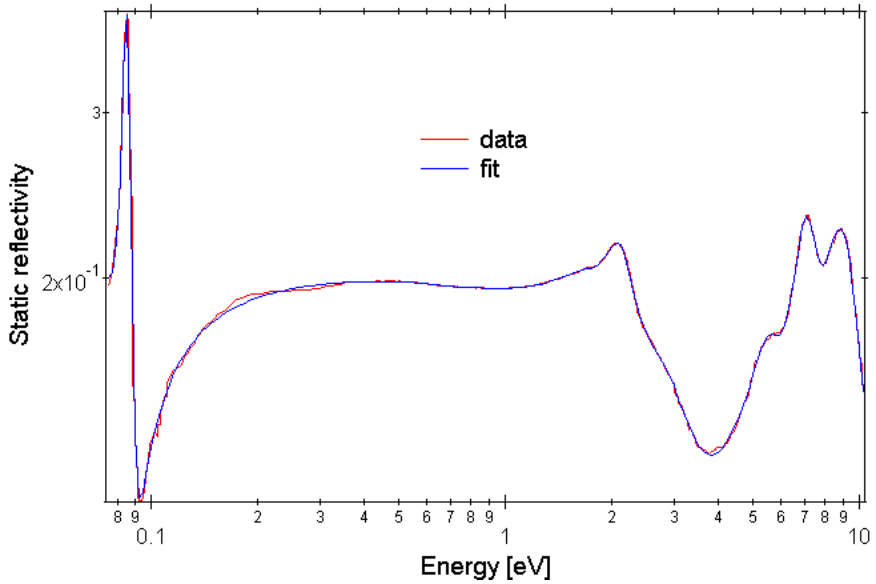

Figure 3.3: Log-log static reflectivity of La_2CuO_4 at $130\,K$, as obtained from the literature. In blue the fit with the Lorentz model is reported (see text).

a variational model $R^*(\omega, t)$ which describes the pump-perturbed reflectivity at time t. We fit the measured $\Delta R(\omega, t)/R_0(\omega)$ with a differential model $(R^*(\omega, t) - R_0(\omega))/R_0(\omega)$, allowing some of the parameters in $R^*(\omega, t)$ to vary in order to reproduce the frequency-dependent transient at each pump-probe delay. In this way the temporal evolution of the quantities that describe the Lorentz model can be obtained: the plasma frequency of the charge-transfer oscillator is reported in Fig.3.5. We stress that caution must be taken for this analysis. The correlations between the parameters as well as the number of varying parameters must be minimized, and also the reflectivity outside of the measured range should be reasonable. A typical fit with "cuts" in the time and frequency domains is shown in Fig.3.4.

3.2.2 Kramers-Kronig analysis

Another approach is based on the relations of Kramers and Kronig constraining the real and imaginary part of the optical constants. At first we need the static optical reflectivity $R_0(\omega)$ over a broad energy range. We fit $R_0(\omega)$ with a Drude-Lorentz model and obtain the static $\epsilon_1(\omega)$ and $\epsilon_2(\omega)$. Notice that we need to fit the static reflectivity because the time-resolved $\Delta R(\omega, t)$ data are within the noise level of the unperturbed reflectivity $R_0(\omega)$. From the static model of $R_0(\omega)$ and the pump-probe data $\Delta R(\omega, t)/R_0(\omega) = (R^*(\omega, t) -$

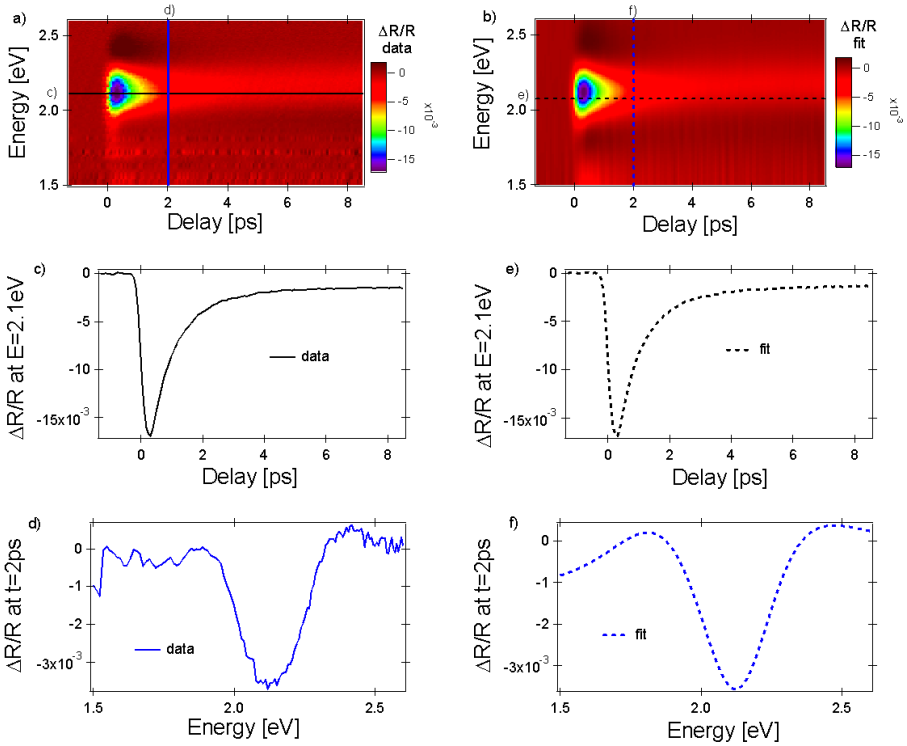

Figure 3.4: Time-resolve data (a) and fit (b). Selected "horizontal" or fixed-energy cuts are showns (c,e) and also "vertical" or energy-dependent ones (d,f).

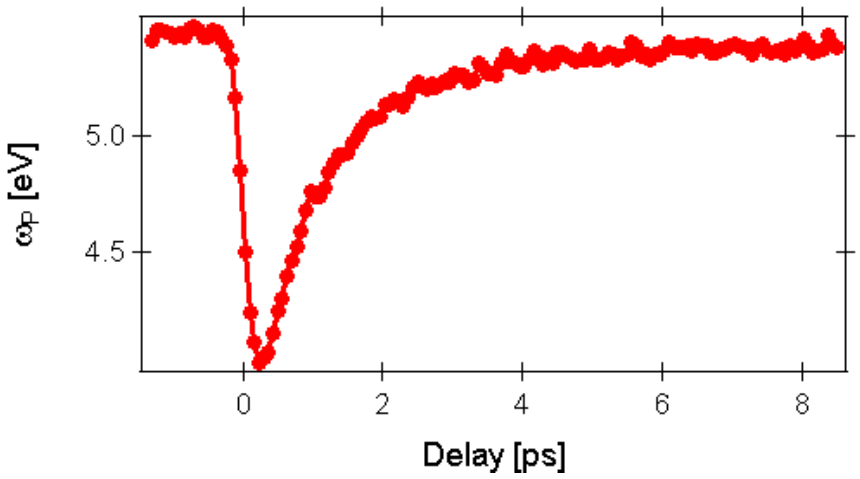

Figure 3.5: Temporal dependence of the plasma frequency of the $\approx 2\,eV$ peak obtained from the differential fits (Fig.3.4).

$R_0(\omega))/R_0(\omega)$ we can readily calculate the pump-perturbed $R^*(\omega,t)$. Finally, from $R^*(\omega,t)$ and eqs.3.16,3.17 we can calculate the real and imaginary part of the complex dielectric functions as a function of pump-probe delay and probed energy, $e_1^*(\omega,t)$ and $e_2^*(\omega,t)$. Notice that $R^*(\omega,t)$ is known over a much smaller spectral range than $R_0(\omega)$. Hence, the KK analysis is fair only if the pump-perturbed reflectivity is negligible outside the probed range. Nonetheless, this approach has the advantage of being model-independent: the calculation of the spectral weight variation of the probed oscillators is straightforward.

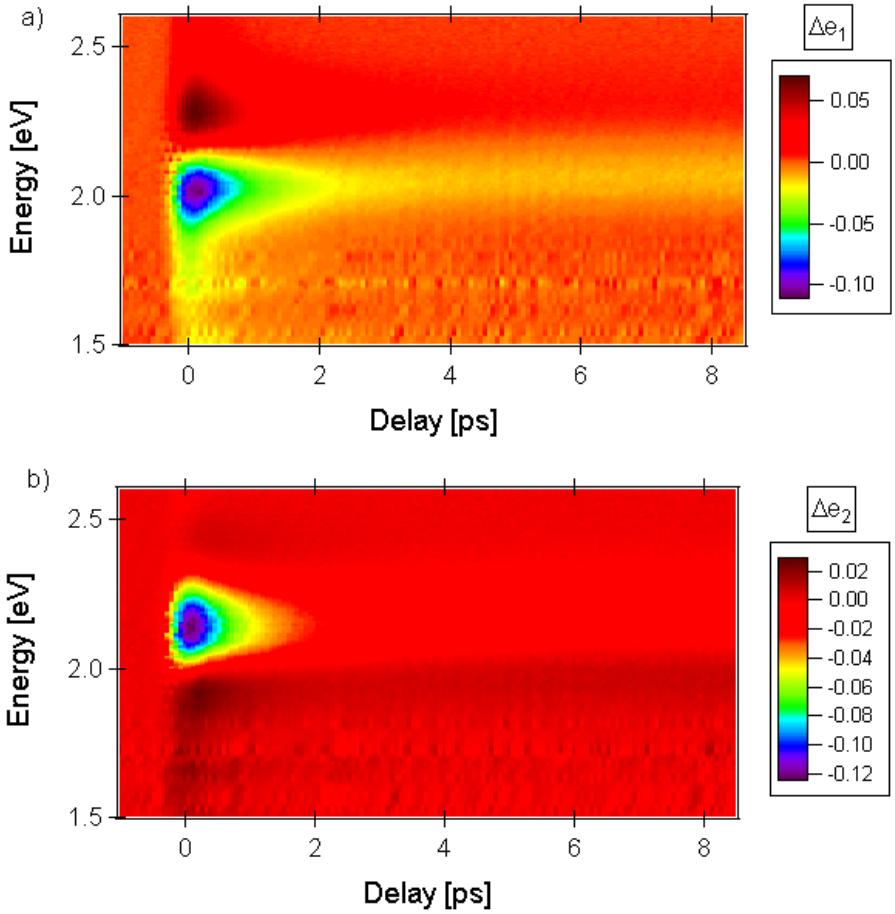

Figure 3.6: Variations in time and frequency domains of the real (a) and imaginary (b) parts of the dielectric function of La_2CuO_4 at $130\,K$.

Chapter 4

Experimental techniques

In this chapter we will introduce the basics of time-resolved terahertz spectroscopy, along with the generation techniques, and the detection by electro-optical sampling. Hereafter, we will briefly introduce our pump-probe experiments and describe both pump and probe pulses. The appendix reports the mathematical models used for terahertz (THz) data analysis, the benchmark measurements performed, and the ultra-short laser sources.

4.1 THz time-domain spectroscopy

The terahertz portion of the electromagnetic spectrum ranges from $0.4\,meV$ ($0.1\,THz$) to $125\,meV$ ($30\,THz$), is non-ionizing, generally highly penetrating in any non-metallic material, and provides noticeable chemical specificity. For these reasons, THz radiation has been employed for medical imaging[55], telecommunications, electronics, security[56], quality control and, moreover, for studying the condensed matter[57]. In particular, light at terahertz frequencies allows to study the strongly correlated electrons systems, as the peculiar physical properties of those systems are related to the low energy excitations of the phonon, spin, and orbital degrees of freedom.

Sources of continuous THz radiation are the backward oscillators[58] (from $0.2\,THz$ to $1\,THz$), quantum cascade lasers ($1.9\,THz$[59], $100\,THz$[60]), CO_2 lasers ($30\,THz$) and the globars. Globars, that emit blackbody spectra, can cover the whole range of terahertz radiation, however the brilliance of these sources is seriously limited because of the Stephan-Boltzmann law to frequencies higher than about $20\,THz$. Unfortunately, the portion of the electromagnetic spectrum ranging from $2\,THz$ to $10\,THz$ is hardly accessible in static experiments. On the other hand, the advent of pulsed sources as accelerators and lasers opened the field of the time-domain terahertz spectroscopy (TDS), allowing for the study of the optical properties of matter in the whole terahertz range. The field of THz spectroscopy rapidly evolved in the last years and various attemps have been made towards pump-probe configurations, where THz

pulses are not used only as a spectroscopic probe but also as a mean to drive matter into transient states. With these purposes, various schemes to generate intense THz pulses have recently become available. We will briefly review the most common ones.

Free electron laser based THz sources, sometimes afflicted by jitter problems that force to perform single-shot electro-optic detection with chirped sampling beams[61], exploit, among others, the phenomenon of "coherent transition radiation" (CRT) that occurs when relativistic electrons cross the boundary between two media of different dielectric constant, generally vacuum and a dirty metal[1]. Accelerator-based sources generally aim at tailoring the THz pulses into tunable and narrow-band ones, for example by slicing the electron bunch[63, 64]. In this framework, within 2015 the TeraFERMI beamiline in Trieste would hopefully become operational with interesting THz pulse parameters: $< 100\,fs$ shaping, mJ pulses, $20\,THz$ bandwidth, and $> 10\,MV/cm$ are at reach[2].

We used either FEL and laser-based sources of pulsed terahertz radiation in order to perform THz pump-probe experiments on strongly correlated electrons systems. Among the FEL experiments, we participated to a beamtime at HZDR in Dresden aimed at studying the complex interaction between the magnetic and vibrational degrees of freedom within $CuGeO_3$ in the spin-Peierls phase. However, the FEL measurements we performed will not be presented here. In the following we focus on laser-based THz sources only. It is possible to generate transient terahertz fields starting from ultra-short pulses of laser light by biasing semiconductors or exploiting non-linear effects in electro-optic media.

4.1.1 THz generation

Consider a slab of material excited at normal incidence by a time-dependent optical pulse. The electromagnetic radiation $E_{rad}(t)$ emitted from the slab in the "far-field" limit, i.e. when the spatial position at which the field is detected is much larger than the ratio of the dimension of the emitter over the emitted wavelength[65], follows from the Maxwell's equations[66]

$$E_{rad}(t) \propto \left(\frac{\partial \boldsymbol{J}}{\partial t} + \frac{\partial^2 \boldsymbol{P}}{\partial t^2} \right) \tag{4.1}$$

where $\boldsymbol{J}$ is the time-varying isotropic conduction current and $\boldsymbol{P}$ the polarization, both induced by the time-dependent photo-excitation. Hence, by proper selection of medium and excitation pulse, it is possible to tune the emitted electromagnetic radiation in the terahertz range: the two principal techniques are based on photo-switching and non-linear optical effects.

[1] G.L. Carr at [62]
[2] A. Perucchi at [62]

The photo-switching consists in shining ultra-short above-gap laser pulses on a biased semiconductor antenna: free photo-carriers ($\boldsymbol{J}(t) \neq 0$) are created and exhibit a time-dependent behaviour due to both the time-varying exciting pulse and the proper relaxation dynamics of the material. This is at the basis of commercial antennas, whose mechanism is sketched in Fig.4.1, that are used for the generation and the detection of pulses of THz radiation. The emitted power does not scale very well with the source laser intensity, as the bias cannot overcome the breakdown field in the semiconducting medium used ($\approx 400\,kV/cm$ in $GaAs$[67]) and, moreover, the thermal induced breakdown phenomenon needs to be considered[67].

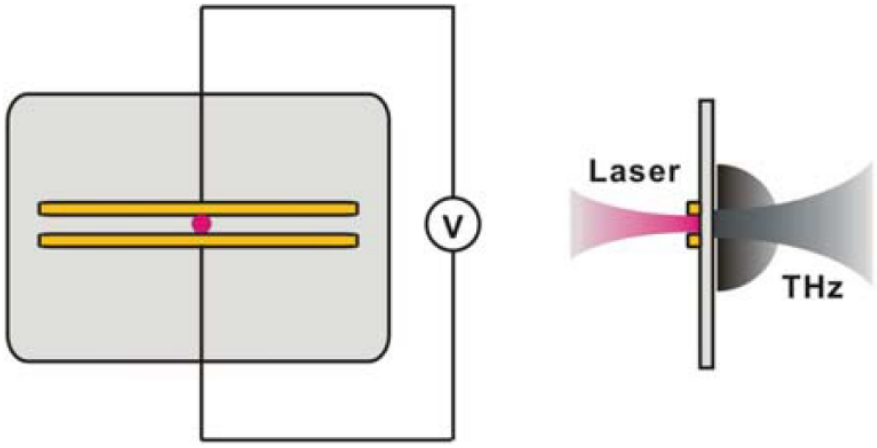

Figure 4.1: Sketch of the generation of terahertz radiation from an antenna, from [67].

From eq.4.1 we notice that a photo-induced variation of the polarization $\boldsymbol{P}(t)$ can result in emission of THz light: the non-linear optical effects can also play a revelant role. In particular, the second order non-linear process of optical rectification is exploited in many non-linear media as $ZnTe$[68], $GaSe$[69], $LiNbO_3$[70] and even organic crystals ($DAST$[71]). As the ultra-short laser pulse is time-dependent and has a duration of the order of $\approx 100\,fs$, the rectified term corresponds to the envelope of the optical pulse. Being the bandwith of the laser of a few meV, light pulses in the THz region can be emitted. In other words the following conditions of phase and wavevector matching between the incoming electromagnetic waves, 1 and 2, involved in the non-linear process, must be fulfilled

$$\begin{cases} \omega_1 - \omega_2 = \Omega_{THz} \\ k_1 - k_2 = k_{THz} \end{cases} \tag{4.2}$$

where Ω_{THz} and k_{THz} are, respectively, frequency and wavevector of the generated terahertz radiation. If we consider an optical pulse with a bandwidth of few meV, i.e. 1 and 2 are the "tails" of the mode-locked laser pulse, and

divide the first equation by the second one we obtain $\frac{\partial\omega}{\partial k} = \frac{\Omega_{THz}}{k_{THz}}$, which is the condition of velocity matching between the group velocity of the laser pulse and the phase velocity of terahertz radiation within the non-linear electro-optic crystal

$$v_g^{opt} = v_{ph}^{THz}. \tag{4.3}$$

This condition corresponds to zero-phase difference, $\delta\phi = 0$, between ordinary and extraordinary waves in a non-linear birefringent material with optical axis parallel to the impinging surface of the optical pulses[72]

$$\delta\phi = \frac{2\pi}{\lambda_{THz}} d(n_g^{opt} - n_{ph}^{THz}), \tag{4.4}$$

where n_g^{opt} is the group index of refraction of the optical pulse, n_{ph}^{THz} the index of refraction for THz light, d the thickness of the medium, and λ_{THz} the THz wavelength. Note that eqs.4.2,4.3,4.4 are general and applies to both generation and detection of THz pulses.

In order to choose the non-linear crystal that optimizes the generation process we shall consider the following properties of the material: the electro-optic coefficient, the absorption coefficient of both optical and THz waves, and the coherence length of the optical rectification process, defined as the thickness of the material at which the dephasing equals π[68]. Moreover, the frequency of the phonon modes inhibits the generation efficiency due to self-absorption within the non-linear crystal and the band-gap needs to be, ideally, more than twice the excitation energy of the laser pulse to prevent both single- and two-photon absorptions (free carriers inhibit the propagation of terahertz radiation in the medium). Some parameters are reported in Tab.4.1. Following

Table 4.1: Physical properties of some non-linear birefringent materials useful for THz generation. r is the electro-optic constant, d_C the coherence lenght calculated for a $\approx 800\,nm$ laser pulse and a rectified term at $1\,THz$, d_{THz} the penetration depth of $\approx 300\,\mu m$ electromagnetic radiation, TO the frequency of the first infrared active phonon, and gap the optical band-gap. Note that all the properties are listed for $1\,THz$ except for DAST ($0.8\,THz$).

	r $[pm/V]$[73]	d_C $[\mu m]$[74]	d_{THz} $[mm]$[74]	TO $[THz]$	Gap $[eV]$
$GaAs$	1.43	254	20	8[75]	1.43
GaP	0.97	455	50	11[76]	2.26
$ZnTe$	4.04	3750	7.7	5.3[76]	2.25
$GaSe$	1.7	1071	20	7.1[77]	2.02[78]
$LiNbO_3$	30.9	55	0.6	4.5[79]	4.2[80, 81]
$DAST$	77	185	0.2	1.1[82]	2.5[83]

these considerations we notice that $ZnTe$ is one of the most favorable non-linear crystals to generate THz radiation starting from ultra-short pulses of laser light with central energy of about $1.55\,eV$. The detailed analysis of the tensorial electro-optical properties can be founde elsewhere[66, 67]. Here we limit ourselves to recall that, in order to achieve the best conversion efficiency,

it is important to choose the proper crystal cutting and orientation: solving eq.4.1 for normal incidence on the 110 surface of a $ZnTe$ crystal we obtain[67]

$$E_{THz} \propto rE^2 \left[sin^2\theta \left(1 + 3cos^2\theta\right)\right]^{\frac{1}{2}} \tag{4.5}$$

$$\chi = atan(2cot\theta) \tag{4.6}$$

where θ is the angle comprised between the laser polarization and the optical axis of the $ZnTe$, χ is the one between the direction of the propagation of the terahertz radiation and the optical axis along the 001 direction.

We mention that is possible to generate THz radiation by focusing both first and second harmonic ultra-short laser pulses in a gas with, respectively, wavelengths $\approx 800\,nm$ and $\approx 400\,nm$: this is the so-called plasma generation technique (Fig.4.2). The non-linear effect of four-wave mixing has been

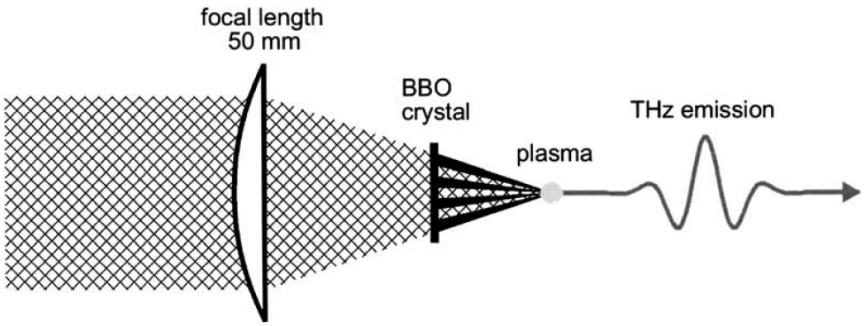

Figure 4.2: Sketch of the optical elements needed to generate THz radiation in the "plasma generation scheme", from [76].

proposed[84] as the source of a photo-induced variation of polarization $\boldsymbol{P}$ that emits THz radiation. However, as it is crucial to overcome the plasma generation edge[85], also ponderomotive effects are important[86]. The detailed physical mechanism underneath this generation scheme is beyond the scope of this thesis. A simple picture (Fig.4.3) that mimicks the plasma generation technique permits to grasp the basic working principle: the fundamental laser pulses generate free charges that are accelerated by the phase-matched second harmonic beam (the phase-matching of the second harmonic to the fundamental in plasma air can be obtained by placing a coverslip between the BBO and the focus[84]). Conversion efficiencies, η, of the laser energy into THz energy up to $2 \cdot 10^{-6}$[86] have been reported, which allowed for the generation of fields as high as $10\,kV/cm$[86].

4.1.2 THz detection

THz pulses are commonly detected with the so-called electro-optical sampling technique (EOS). EOS is the inverse process of the optical rectification: a THz pulse is mixed with an infrared laser pulse in a non-linear medium. The THz pulse perturbs the polarization of the electro-optical crystal by Pockel's

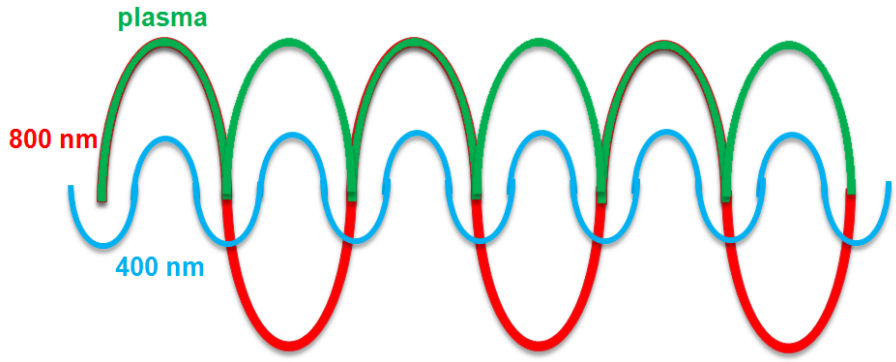

Figure 4.3: Heuristic interpretation of the physical mechanism for THz generation from the plasma scheme. The fundamental harmonic, $\approx 800\,nm$, generates a plasma in air. The second harmonic pulses act as a bias field that forces the free charges in oscillation. The terahertz radiation is emitted in the relaxation process.

effect, inducing a variation in the birefringence of the electro-optical medium. When the THz pulse ($\approx 1\,ps$) and the optical one ($\approx 50\,fs$, called "sampling") co-propagate in the non-linear medium, the polarization of the optical pulse is tilted of an angle that is proportional to the amplitude of the applied terahertz field. By varying the temporal delay between the sampling and the terahertz pulses it is possible to detect the time-dependent variation of the electric field. This is achievable, for example, by using a quarter wave-plate ($\lambda/4$) after a $1\,mm$ thick $ZnTe$ to turn the polarization into circular when no THz field is applied. Hence a Wollaston prism after the $\lambda/4$ separates the polarization into the parallel and perpendicular components. The intensities of the two polarizations are detected by two diodes, whose difference in voltage is acquired by a lock-in amplifier locked at the frequency of a mechanical chopper placed in the optical path of the THz beam. When the THz radiation impings on the $ZnTe$ crystal in temporal coincidence with the sampling pulse, the polarization of the sampling pulse will be rotated, thus the polarization will turn from circular to elliptical after the $\lambda/4$ and the two photo-diodes will be unbalanced of a quantity related to the amplitude of the THz field. If the THz-induced ellipticity is small, the diodes will give a signal proportional to the amplitude of the terahertz field. Finally, by varying the temporal delay between sampling and THz pulse it is possible to detect the time-dependence of the THz field. In particular, the ordinary and extra-ordinary components of the probe beams will be dephased of a quantity $\delta\phi$ that is proportional to the difference between the index of refraction, δn, along the ordinary and extra-ordinary axis (cfr. eq.4.4 and [72]). It can be shown[67] that

$$\delta n(t) \propto \frac{1}{2} n_{opt}^3 r E_{THz}(t) \tag{4.7}$$

where n_{opt} is the unperturbed index of refraction of the non-linear medium, r the electro-optic constant and $E_{THz}(t)$ the time-dependent amplitude of the terahertz field. From eqs.4.4,4.7 the phase mismatch acquired by the THz

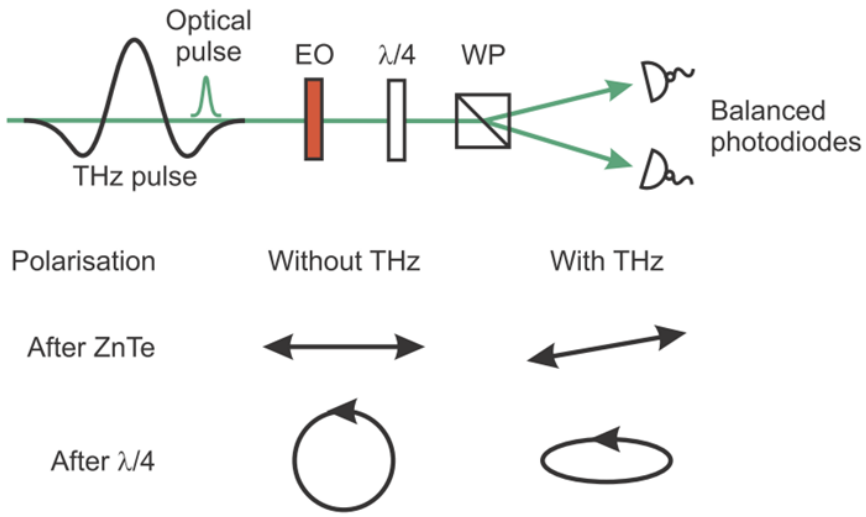

Figure 4.4: Sketch of the electro-optical sampling technique, from [87].

radiation of wavelength λ_{THz} through the thickness d of a non-linear crystal is

$$\delta\phi(t) = \frac{\pi d n_{opt}^3 r E_{THz}(t)}{\lambda_{THz}}. \tag{4.8}$$

In the case of $1\,mm$ thick $ZnTe$ pumped with $\approx 800\,nm$ ultra-short laser pulses, $\delta\phi$ is on the order of $0.5°$ for an applied field of $100\,kV/cm$. A typical terahertz field detected by EOS is reported in Fig.4.5a. The corresponding fast Fourier transform shows the spectral content of the single-cycle THz pulses (Fig.4.5b).

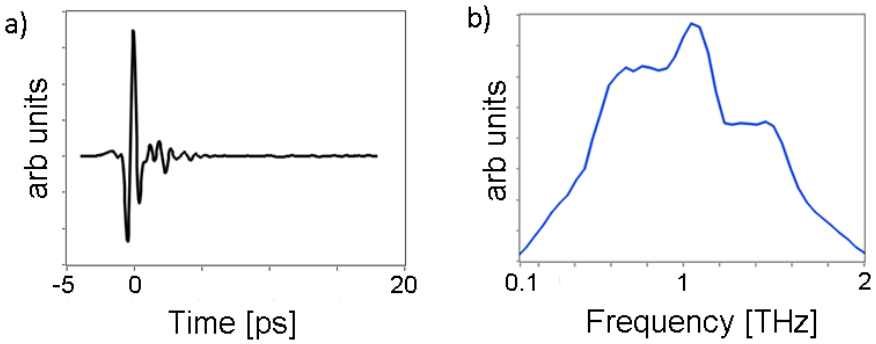

Figure 4.5: a) Typical THz field generated in purged nitrogen atmosphere by optical rectification in $1\,mm$ thick 110-oriented $ZnTe$ crystal. The atmosphere is controlled in order to suppress the absorption and re-emission from air. b) Amplitude of the FFT of the time-dependent field, evidencing its spectral components.

4.2 Pump-probe experiments

A pump-probe experiment consists in perturbing the static properties of a sample and detect in the time-domain its relaxation dynamics. This technique has proven to be extremely powerful to study complex materials characterized by strong electron-electron interactions, as it permits either to disentangle temporally the interaction between the different degrees of freedom within the system[17, 26, 27], or to photo-induce novel, intriguing non-thermal states of matter[18–20, 33]. In our case an intense ultra-short "pump" laser pulse perturbs the sample with fluences ranging between $10\,\mu J/cm^2$ and $10\,mJ/cm^2$ and wavelengths either in the terahertz or optical regions of the electromagnetic spectrum. The "probe" pulse, at least 50 times weaker in intensity, is composed by either single-colour or broadband optical pulses, generated by super-continuum, or $\approx 1\,ps$ THz radiation. By collecting the probed signal as a function of pump-probe delay it's possible to map the relaxation dynamics in the time-domain with a resolution limited only by the time-extent of the pump and probe pulses (from $10\,fs$ to $1\,ps$, according to the different wavelengths of the pump pulses).

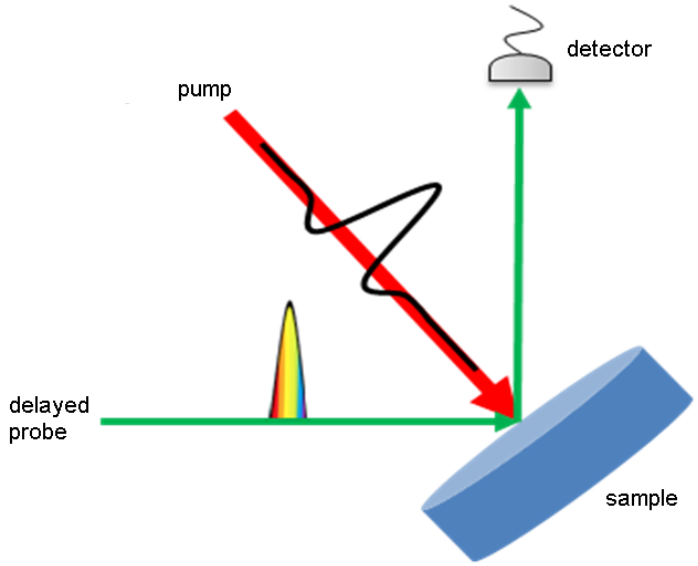

Figure 4.6: Sketch of a pump-probe experiment. As an example, the pump is a $\approx 1\,ps$ THz pulse, while the probe is broadband. The detector summarizes all the optical and electronic elements needed for data acquisition.

4.2.1 Intense THz pulses: tilted-front generation

In order to obtain pulses of THz radiation that can be effectively used as pump in laser-based pump-probe experiments we exploit the tilted wavefront generation scheme[74]. In a non-linear crystal where the NIR light propagates faster respect to THz light, the phase-matching can be achieved by "slowing

down" the NIR light in the direction of THz propagation. Such effective slowing can be attained by tilting the wavefront of the NIR laser pulses. A crystal with high eletro-optical coefficient ($168\,pm/V$[74]) and with a suitable relation between the index of refraction for the THz and NIR light is stoichiometric lithium niobate ($s - LiNbO_3$) doped with MgO in order to prevent photo-damaging[88]. It is possible to tune the wavefront tilt angle γ in order to fulfill the matching condition between the phase velocity of the THz radiation, which propagates perpendicular to the wavefront, and the group velocity of the NIR pulses

$$v_{NIR}cos(\gamma) = v_{THz}, \tag{4.9}$$

or

$$n_{THz}cos(\gamma) = n_{NIR}, \tag{4.10}$$

where n_{THz} is the index of refractin of for THz radiation and n_{NIR} the group index of refraction for NIR light. The situation of quasi phase-matching is pictorially shown in Fig.4.7a. In practice, as sketched in Fig.4.7b, we use a grating to tilt the wavefront of the ultra-short laser pulses. The polarization of the incident beam before the grating is kept horizontal (perpendicular to the grating's rows) in order to maximize the reflection efficiency ($\geq 65\%$ at $800\,nm$[3]). Then is rotated by 90° to match the orientation of the optical axis of the crystal, which in Fig.4.7b is perpendicular to the plane of the page.

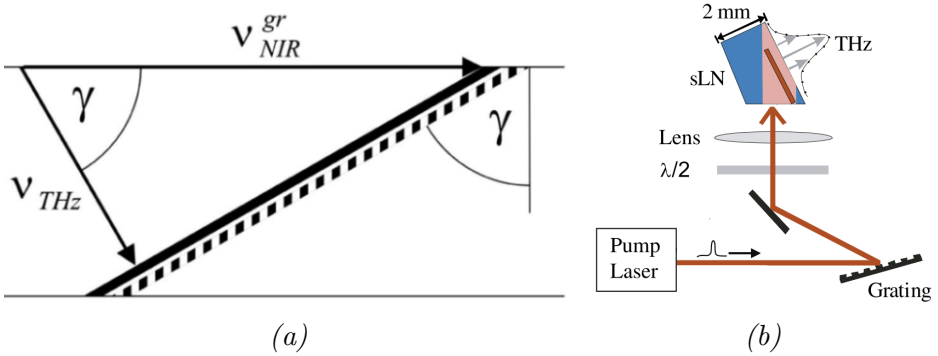

Figure 4.7: a) Illustration of velocity matching using tilted-pulse-front excitation. THz wave (bold line) generated in $LiNbO_3$ crystal by the tilted wavefront of the pump pulse (dashed bold line). In order for the two to remain in phase during propagation, the projection of the pump pulse velocity vector along the direction of the THz propagation should be equal to the magnitude of THz phase velocity. From [74]. b) Sketch of the optical elements required to generate intense THz radiation from pulsed laser sources. Adapted from [70].

In order to ensure that the tilting angle γ within the electro-optical medium acquires the correct value, it is necessary to consider the mismatch between the index of refraction of the crystal and of its surroundings. Fig.4.8 shows that the projection of the wavefront on the plane perpendicular to the propagation direction of the electromagnetic radiation is conserved going from a medium

[3]Thorlabs GR25-1850 user manual

to another, hence

$$\frac{tan(\gamma)}{p} = \frac{tan(\gamma^*)}{p^*}, \tag{4.11}$$

where γ is the effective tilting angle and γ^* the one outside the crystal. Inasmuch as $p = p^*/n$, where n_{NIR} is the index of refraction at $800\,nm$ of the non-linear medium and for simplicity $n_{air} \approx 1$, we obtain

$$tan(\gamma) = \frac{tan(\gamma^*)}{n_{NIR}} \tag{4.12}$$

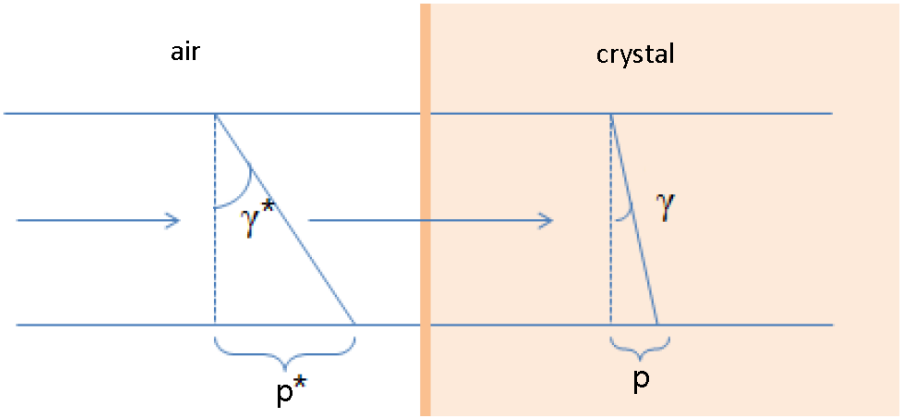

Figure 4.8: Tilted wavefront inside and outside the electro-optical crystal.

Prism vs. grating

The angular dispersion D of an optical element is defined as the amount of variation of the emergy ray angle $b(\lambda)$ on the incident wavelength λ

$$D = \frac{db(\lambda)}{d\lambda}. \tag{4.13}$$

This is related to the wavefront tilting angle γ by the general relation[89, 90]

$$\tan\gamma = \lambda D. \tag{4.14}$$

$b(\lambda)$ as a function of the incident angle a is

$$b_G(\lambda) = arcsin\left[mG\lambda - \sin(a)\right], \tag{4.15}$$

$$b_P(\lambda) = a - \alpha + arcsin\left[\sin(\alpha)\sqrt{n^2(\lambda) - \sin^2(a)} - sin(a)\cos(\alpha)\right], \tag{4.16}$$

where m is the diffraction order, G the number of rows in a millimeter, α the apex angle of the prism, $n(\lambda)$ the index of refraction, and the subscripts "G" and "P" are shorthands for *grating* and *prism* respectively. For a grating, a and b refers to the normal to the plane of the grating. For a prism, a refers

to the normal to the surface of the prism where the beam enters, while b is the angle departing from the incident direction. Being a independent from the wavelength we obtain

$$\tan\gamma_G = \lambda D_G = \lambda \frac{mG}{\cos\left[b(\lambda)\right]}, \tag{4.17}$$

$$\tan\gamma_P = \lambda D_P = \lambda \frac{\sin(\alpha)\frac{dn^2(\lambda)}{d\lambda}}{\cos\left[b(\lambda) - a + \alpha\right]\sqrt{n^2(\lambda) - \sin^2(a)}}. \tag{4.18}$$

We can express the index of refraction of the prism with the Sellmeier equation

$$n^2(\lambda) = 1 + \frac{B_1\lambda^2}{\lambda^2 - C_1} + \frac{B_2\lambda^2}{\lambda^2 - C_2} + \frac{B_3\lambda^2}{\lambda^2 - C_3} \tag{4.19}$$

where the B_i and C_i are empirical constants. The second derivarive of the index of refraction is

$$\frac{dn^2(\lambda)}{d\lambda} = -\frac{C_1 2\lambda B_1}{(\lambda^2 - C_1)^2} - \frac{C_2 2\lambda B_2}{(\lambda^2 - C_2)^2} - \frac{C_3 2\lambda B_3}{(\lambda^2 - C_3)^2}. \tag{4.20}$$

We restrict now to $\lambda = 0.8\,\mu m$, $m = 1$, $G = 1800\,mm^{-1}$, $\alpha = \pi/3$, $B_1 = 1.73848403$, $B_2 = 0.311168974$, $B_3 = 1.17490871$, $C_1 = 0.0136068604\,\mu m^2$, $C_2 = 0.0615960463\,\mu m^2$ and $C_3 = 121.922711\,\mu m^2$. The emerging wave and tilting angles depend only on the incident angle a

$$b_G(a) = arcsin\left[1.44 - \sin(a)\right], \tag{4.21}$$

$$\tan\gamma_G(a) = \frac{1.44}{\cos\left\{arcsin\left[1.44 - \sin(a)\right]\right\}}, \tag{4.22}$$

$$b_P(a) \approx a - \frac{\pi}{3} + arcsin\left[\frac{\sqrt{3}}{2}\sqrt{3.114 - \sin^2(a)} - \frac{\sin(a)}{2}\right], \tag{4.23}$$

$$\tan\gamma_P(a) \approx \frac{-0.01407}{\cos\left\{arcsin\left[\frac{\sqrt{3}}{2}\sqrt{3.022 - \sin^2(a)} - \frac{sin(a)}{2}\right]\right\}\sqrt{3.022 - \sin^2(a)}}. \tag{4.24}$$

Two factors affect the tilting angle of a beam at wavelength $\bar{\lambda}$ emerging from a dispersive medium, transmitting in vacuum through a telescope and then propagating in a crystal: the demagnification factor N of the telescope and the index of refraction n of the crystal at λ_{NIR}. If γ^* is the wavefront titled angle just out of a prism or grating, the effective γ inside the crystal follows the relation

$$\tan\gamma = \frac{N \cdot \tan(\gamma^*)}{n(\lambda_{NIR})}. \tag{4.25}$$

At $\lambda_{NIR} = 0.8\,\mu m$ for stoichiometric lithium niobate we have $n(0.8\,\mu m) \approx 2.25$, while $n(1\,THz) \approx 4.96$[74]: for this case we can calculate from eq.4.10 the

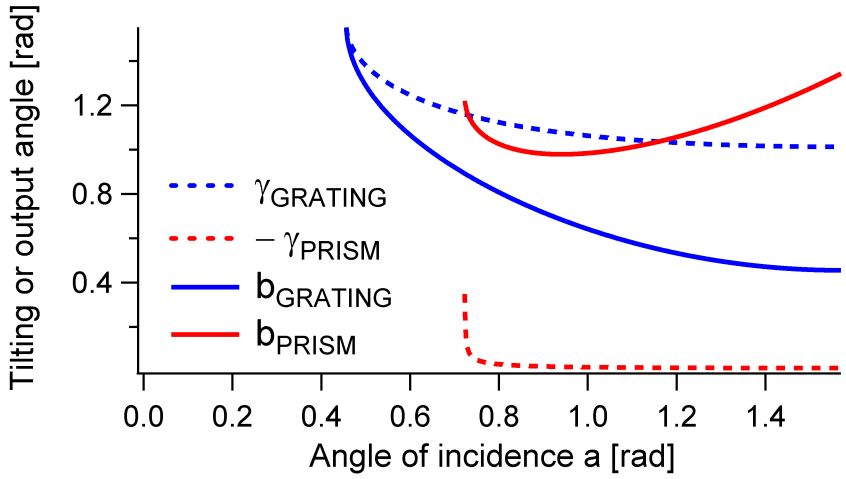

Figure 4.9: Numerical simulation of eqs.4.21-4.24 of output and tilting angles as functions of the incident angle.

tilting angle needed inside the crystal

$$\gamma = arccos\left[\frac{n(0.8\mu m)}{n(1THz)}\right] \approx arccos\left(\frac{2.25}{4.96}\right) \approx 63°, \tag{4.26}$$

hence, from eq.4.25, γ^* and N must satisfy the identity

$$\gamma^* \approx \arctan\left(\frac{4.42}{N}\right). \tag{4.27}$$

For the grating we obtain solutions for $N = 1$ ($\gamma^* \approx 77°$, $a \approx 30°$ and $b \approx 71°$) and for $N = 2$ ($\gamma^* \approx 66°$, $a \approx 43°$ and $b \approx 49°$). This means that we can use a telescope after the grating with maximum demagnification factor of two but we can also use any telescope before the grating that doesn't damage the optics.

For a prism there is no emerging wave when $a \leq 0.722$ (Fig.4.9): for alignment purposes we must move at least 5° away from this edge and thus to $a \geq 0.8$ that corresponds to $N \geq 140$. This very high demagnification brings an almost 20000 times greater fluence on the sample.

In order to decide the optical-tilting system we now briefly discuss the maximum fluence we can shine on $LiNbO_3$. In order to avoid photo-damaging[88], we choose $67\,mJ/cm^2$ as the fluence limit[74]. This explains why the prism is not used, to our knowledge, in the tilted-front generation literature. The grating, on the other hand, has a damage threshold[4] of $350\,mJ/cm^2$. If we use a telescope before the grating we can reduce the FWHM of the spot on the grating down to $0.2\,mm$ ($0.35\,mm$) at $1\,W$ ($3\,W$) at $1\,KHz$ (for details on laser sources see Par.4.3.3).

If the grating is engineered with a regular shape at a precise angle respect to the surface, the first order of diffraction emerges perpendicularly to the local

[4]Thorlabs GR25-1850 user manual

sawtooth profile: the reflection is maximixed for a certain wavelength, which correspond to the blazing angle at with the surface has been engineered. The blazing angle θ_B can be calculate from

$$2sin(\theta_B) = mG\lambda, \tag{4.28}$$

where λ is the wavelength we want to optimize the grating for. For $\lambda = 500\,nm$ we get $\approx 26.74°$, that is the engineered angle of the commercial grating used in our experiments. We note that such a grating is not optimized for high reflection at $800\,nm$. We calculate that the ideal grating should have $1500\,rows/mm$ and should be blazed $800\,nm$ ($\theta_B \approx 36.87°$): the correct tilting angle within $LiNbO_3$ is obtained for the first order of diffraction that emerges at angle 73.11° when the $\approx 800\,nm$ ultra-short laser pulses are incident with an angle of 13.74° (Fig.4.10).

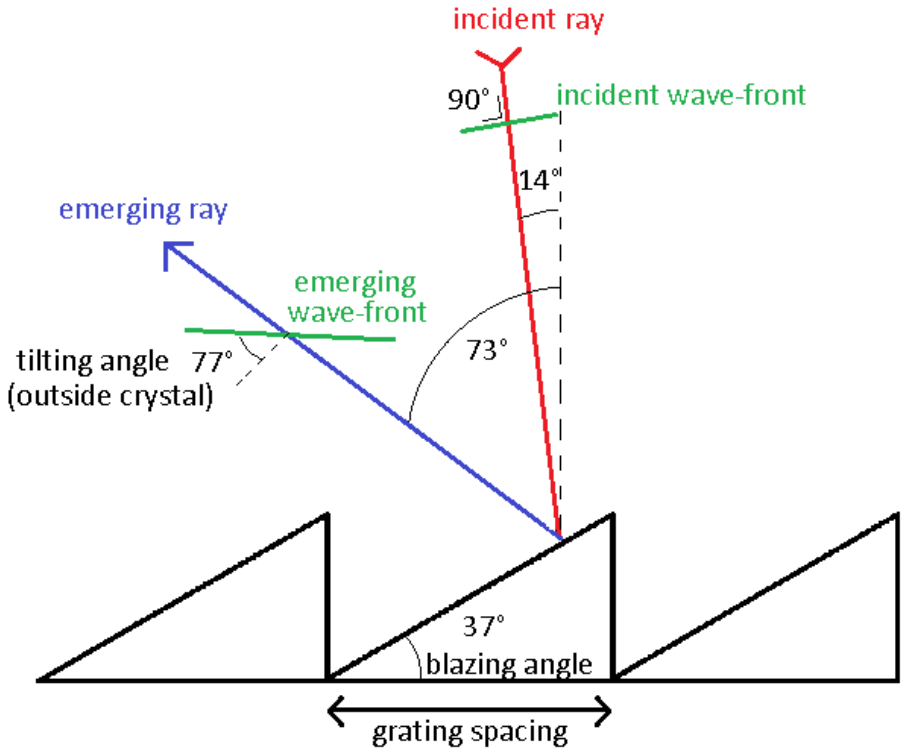

Figure 4.10: Illustration of the ideal grating to be used to generate intense $\approx 1\,ps$ THz field from ultra-short $\approx 800\,nm$ laser pulses. The angle of incidence and of the first order of diffraction are reported, togheter with the blazing and tilting angle outside the MgO-doped $LiNbO_3$. The grating spacing d satisfies the relation $G = \frac{1}{d} = 1500\,rows/mm$.

Characterization

From a highly efficient ($\eta \geq 10^{-4}$) tilted-front generation scheme we obtain $\approx 1\,ps$ single-cycle THz pump pulses with peak amplitudes that exceed $100\,kV/cm$, fluences of more than $10\,\mu J/cm^2$, and with energy per pulse of

about $100\,nJ$. The amplitude of the electric field $E(t)$ as a function of time is estimated from the comparison between the detected EOS traces, that characterize the temporal profile of the THz field, and the integrated power measured with a bolometer[5]. The bolometer is sensitive to electromagnetic radiation with frequencies (wavelengths) between $0.1\,THz$ ($3\,mm$) and $30\,THz$ ($10\,\mu m$) with responsivity equal[6] to $6.55 \cdot 10^4\,V/W$ at the chopping frequency of $5\,Hz$. Considering the losses of three mirrors, three lenses, one half-waveplate and the grating, we can estimate the efficiency of generation

$$\eta = \frac{9\,V}{6.55 \cdot 10^4\,V/W}\frac{1}{1\,W} \approx 1.4 \cdot 10^{-4}, \tag{4.29}$$

that is in agreement with the literature (Tab.4.2).

$[nm]$	$[KHz]$	$[fs]$	Laser $E/pulse$	THz $E/pulse$	$\eta\,[10^{-4}]$	Ref.
800	200	150	$2.3\,\mu J$	$30\,pJ$	0.13	[91]
800	200	170	$2.3\,\mu J$	$100\,pJ$	0.43	[73]
1035	1	300	$400\,\mu J$	$100\,nJ\,(80\,K)$	2.5	[92]
800	1	100	$6\,mJ$	$3.3\,\mu J\,(80\,K)$	7	[70]
800	1	150	$800\,\mu J$		5	[93]

Table 4.2: Summary of papers exploiting the tilted-front generation scheme. $[nm]$ is the central wavelength of the pulsed laser source, $[KHz]$ the repetition rate, $[fs]$ the duration of the laser pulses, $E/pulse$ the energy of each pulse, η the conversion efficiency.

The ultra-fast laser source emits $1\,W$ and works at $1\,KHz$ of repetition rate (Par.4.3.3), hence the maximum energy of each single-cycle $\approx 1\,ps$ THz pulse is $0.14\,\mu J$. In order to calculate the effective field amplitude, we estimate the proportionality constant between the values detected in the time-domain by electro-optical sampling and the field amplitude in kV/cm. The following relation holds

$$0.14\,\mu J = \frac{A\epsilon_0}{2}\int (\alpha e(t))^2\,dt, \tag{4.30}$$

where A is the section of the laser beam, ϵ_0 the dielectric constant of vacuum, α the proportionality constant between the true field, $E(t)$, and the voltage measured by EOS, $e(t)$. From eq.4.30 we obtain

$$\alpha \approx 10^{10}\,m^{-1}. \tag{4.31}$$

The field produced in our tabletop setup is then fully characterized as shown in Fig.4.11a. In order to obtain the frequency components we can Fourier transform the EOS traces and the result is plotted in Fig.4.11b.

[5] Gentec-eo THZ5I-MT-BNC

[6] Calibration file from Gentec-eo, performed with $632.8\,nm$ laser light.

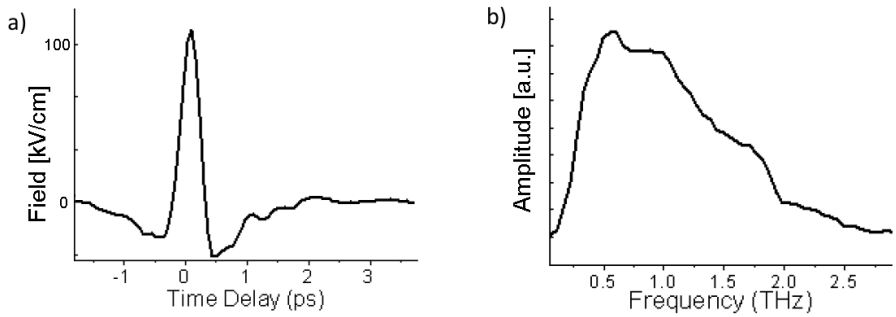

Figure 4.11: a) True amplitude, $E(t)$, of the electric field obtained through high efficient optical rectification in lithium niobate. b) Fourier transform of $E(t)$ that shows the spectral content of the terahertz pulses.

4.2.2 Time-resolved THz spectroscopy

The pulsed nature of the THz sources described earlier offers a direct method to probe the quasi-dc response of a medium without applying electrical contacts. Moreover, THz pulses can be exploited in laser-based pump-probe experiments. In a typical "time-resolved terahertz spectroscopy" (TRTS) experiment the THz fields probe the relaxation dynamics of the sample after photo-excitation by ultra-short optical laser pulses. TRTS measurements have been performed in order to study the sub-picosecond transient photoconductivity of various semiconductors[94–96], superconductors[97], and Mott-insulators[98]. Moreover, this technique has been exploited to study the time-

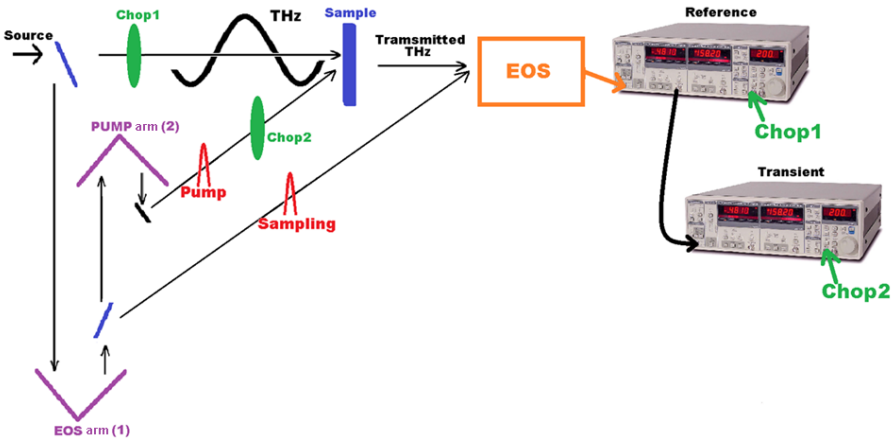

Figure 4.12: Sketch of the time-resolved terahertz spectroscopy setup we developed in our lab in order to perform transmission measurements. $\approx 800\,nm$ pump and sampling beams are red, the $\approx 1\,ps$ THz pulse is black.

dependent perturbation to the low-frequency intermolecular modes during solvation processes[99] and the non-Drude-like dynamics of photo-injected charges into the sintered electrode of a Gratzel's solar cell[100]. A sketch of the setup we use to perform TRTS experiments in transmission is reported in Fig.4.12: the mechanical delay stage "arm 2" sets the temporal delay between the sam-

pling and the pump laser pulses while they are scanned respect to the THz pulse by moving the delay stage "arm 1". From the first lock-in the reference THz pulse is detected, while the pump-induced variation is measured by the second lock-in. We stress that the synchronous scan of pump and sampling pulses avoids artifacts in the measurements[95, 97] that can arise from the fact that the probe and pump pulses have quite different temporal extent[87]. The

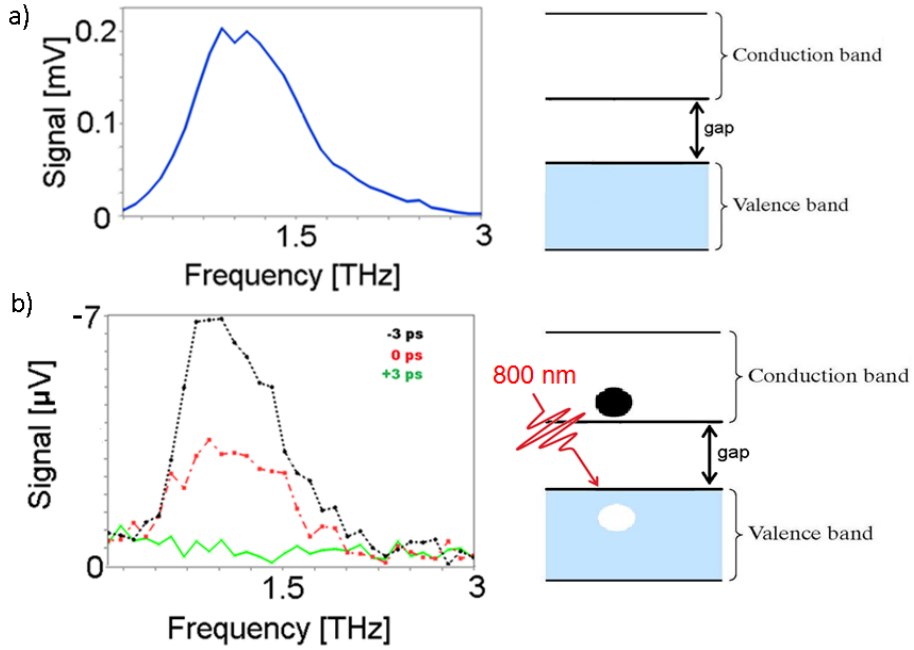

Figure 4.13: Optical pump-THz probe transmission measurements on bulk silicon. a) The FFT amplitude of the reference field detected in the time-domain by the first lock-in (see Fig.4.12). On the right a simple bandgap semiconductor is represented. b) Pump-induced FFT amplitude for three characteristic pump-probe delays: it is evident that when the pump precedes the probe ($t = -3\,ps$), the THz transmission is hindered. On the right, sketch of the pump-induced charge transfer from the valence to the conduction band.

models (see Par.4.3.1) needed to extract the time evolution of the optical constants from a TRTS experiment depends on the experimental apparatus[101]. For the chosen configuration, we suggest that the simplest way to describe the photo-excited response is to recast eq.4.58 as

$$\widetilde{\sigma}(\omega,t) \approx \frac{2}{Z_0 d^*}\frac{\widetilde{E}_S(\omega)-\widetilde{E}^*_S(\omega,t)}{\widetilde{E}^*_S(\omega,t)}, \tag{4.32}$$

where $\widetilde{\sigma}(t)$ is the complex conductivity of the photo-excited medium as a function of the sampling-pump delay t. To a first approximation we assume that the pump perturbes only a thin layer on the surface of the sample of thickness d^*, equal to the penetration depth of the pump pulse. $\widetilde{E}_S(\omega)$ is the Fourier transform of the electro-optically sampled field without the pump pulse, $\widetilde{E}^*_S(\omega,t)$ is the one after photo-exctitation measured at each delay t between the sampling and the pump pulses.

In order to characterize the TRTS setup, we studied the dynamical variation of the optical response of silicon after the excitation with $\approx 800\,nm$ pulses. In Fig.4.13 we show the amplitude of the Fourier transform of the EOS field detected at three characteristic time delays between the pump and the sampling pulses ($-3\,ps$, 0, and $+3\,ps$). It is evident that when the THz field is sampled after the pump arrival ($t = 0$ and $t = -3\,ps$) the photo-induced population of the conduction band induces a drop of transmission over the THz range. On the contrary, when the probe precedes the pump, nothing is detected by the second lock-in ($t = +3\,ps$). This can be easily rationalized in a Drude-like picture, where the free charges photo-excited in the conduction band strongly reflect the electromagnetic radiation at low frequencies.

4.2.3 White light generation

As explained in Ch.3, the measurement of the reflectivity over a broad energy range allows to disentangle the different oscillators involved in the overall optical response of the studied system. Hence we developed probes that cover a wide portion of the optical spectrum. A detailed description of white light generation goes beyond the scope of this thesis and can be found elsewhere[102], we will review the basics in the following. The "super-continuum" generation is based essentialy on four processes: self-focusing, self-phase modulation, raman scattering and four-wave mixing. The self-focusing is a non-linear effect: when a beam of light having a nonuniform transverse intensity distribution propagates through a material for which $n_{Kerr} > 0$ (n_{Kerr} is an optical constant of the material[103]), the material effectively acts as a positive lens. The self-focusing enhances the intensity in the central part of the beam, magnifying the other non-linear effects that concurr in white light generation. The spectral broadening is supported by both raman scattering and four-wave mixing, but the main non-linear effect at the basis of broadband generation is the self-phase modulation.

Self-phase modulation can be explained with the following simple model. Take a laser pulse with an intensity profile $I(t)$ that is gaussian in time

$$I(t) \propto e^{-\frac{t^2}{\tau^2}}, \tag{4.33}$$

with τ proportional to the characteristic FWHM of the gaussian distribution. We know that the index of refraction of a non-linear medium in presence of an intense pulse of radiation is a time-dependent quantity

$$n(t) = n_0 + n_K I(t), \tag{4.34}$$

where K is the shorthand for $Kerr$ and n_0 is the unperturbed index of refraction. Hence the laser pulse follows an optical path that is different from $L_0 = n_0 d$, with d crystal thickness, of the quantity

$$\Delta L(t) = n_K d I(t) \propto n_K d e^{-\frac{t^2}{\tau^2}}, \tag{4.35}$$

that brings a time-dependent dephasing $\Delta\phi(t)$ of the frequency component ω_i of the laser pulse equal to

$$\Delta\phi(t) = -\omega_i \Delta L(t) \propto -\omega_i n_K d e^{-\frac{t^2}{\tau^2}}. \tag{4.36}$$

By definition the frequency of a wave is just the temporal derivative of its phase, hence the frequency of the component ω_i is broadened and time-dependent

$$\Delta\omega_i(t) = \omega(t) - \omega_i = \frac{\partial\Delta\phi(t)}{\partial t} \propto \omega_i n_K d \frac{t}{\tau^2} e^{-\frac{t^2}{\tau^2}}. \tag{4.37}$$

This last equation implies that the different frequency components experience different optical paths, and the frequencies are dispersed temporally leading to the so-called "temporal chirp". If the phase envelope is much longer than the single optical cycles, the relation $t \ll \tau^2$ holds and the exponential function in eq.4.37 is close to one

$$\Delta\omega_i(t) \propto \omega_i n_K d \frac{t}{\tau^2}, \tag{4.38}$$

so the frequency ω_i of the i-th component is transformed in the quantity $\omega(t)$ that is proportional to the time t

$$\omega(t) \propto \omega_i \left(1 + n_K d \frac{t}{\tau^2}\right). \tag{4.39}$$

In other words, the self-phase modulation induces both a broadening of each spectral component of the initial pulse of light and a linear temporal chirp. The raw broadband probe data display a linear temporal chirp on the order of few hundreds of femtoseconds across the $500 - 900\,nm$ range (not shown), and are thus consistent with the previous model.

The broadband pulse is generated from the $\approx 800\,nm$ ultra-short laser source[104], and has a spectral content that extends from $400\,nm$ up to about $1600\,nm$ (Fig.4.14), even though the portion of the spectrum effectively used extends only up to $1000\,nm$.

4.3 Appendix

4.3.1 Models

Here we describe the mathematical models that permits to obtain the optical response of a sample in the THz range. At first, the measurement of the temporal shape $E(t)$ of reflected or transmitted THz fields both of a reference and of the sample must be performed. Hence, by Fourier transforming and an appropriate model, it is possible to obtain the optical properties of the sample without resorting to the Kramers-Kronig relations. To build the model we need at first to recall the Fresnel coefficients that links the amplitude of a time dependent electric field incident on an interface to the reflected ($\widetilde{r}(\omega)$) and

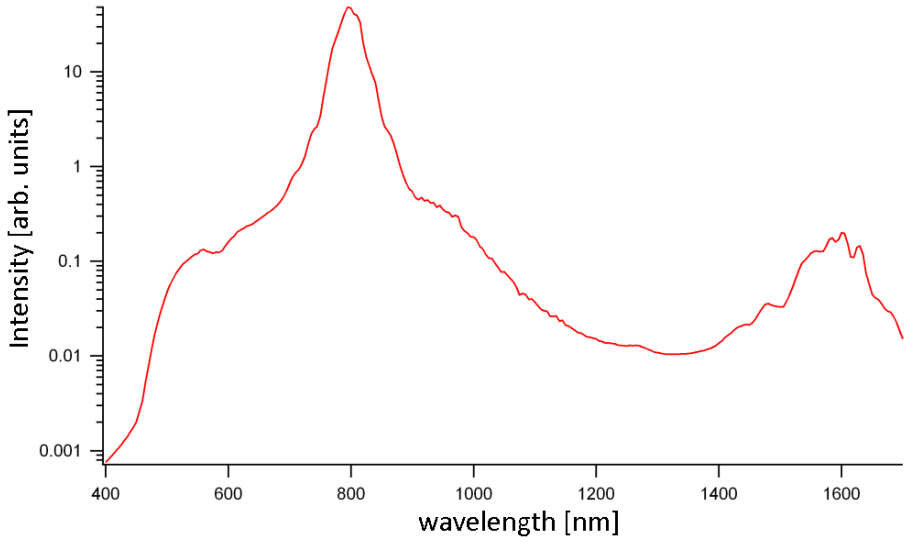

Figure 4.14: Typical spectral distribution of the broadband white light pulses generated in our lab.

transmitted ($\widetilde{t}(\omega)$) ones[72]. For s-polarized waves incident at the interface between two semi-infinite media i and j we have

$$\widetilde{r}_{ij}(\omega) = \frac{\widetilde{E}_{reflected}(\omega)}{\widetilde{E}_{incident}(\omega)} = \frac{\widetilde{n}_i(\omega)\cos(\vartheta_i) - \widetilde{n}_j(\omega)cos(\vartheta_j)}{\widetilde{n}_i(\omega)\cos(\vartheta_i) + \widetilde{n}_j(\omega)cos(\vartheta_j)}, \tag{4.40}$$

$$\widetilde{t}_{ij}(\omega) = \frac{\widetilde{E}_{transmitted}(\omega)}{\widetilde{E}_{incident}(\omega)} = \frac{2\widetilde{n}_i(\omega)cos(\vartheta_i)}{\widetilde{n}_i(\omega)\cos(\vartheta_i) + \widetilde{n}_j(\omega)cos(\vartheta_j)}, \tag{4.41}$$

where $\widetilde{n}_i(\omega) = n_i(\omega) + ik_i(\omega)$ and $\widetilde{n}_j(\omega) = n_j(\omega) + ik_j(\omega)$ are, respectively, the frequency dependent index of refraction of the two media, while ϑ_i and ϑ_t are the incidence and transmission angles. In the following we will assume the general case of a four media system: semi-infinite air/vacuum, sample slab, substrate slab and semi-infinite air/vacuum. Those media are sketched in Fig.4.16 as medium 1, 2, 3, and 4, respectively. Later on, we will frequently refer to "optically thick" and "optically thin" materials. By optically thick we mean a medium in which the rays originated from higher order internal reflections are well separated in time. In this case, by choosing an appropriate (but not too short for the FFT) temporal window, we can get rid of the multiple reflections and consider only the first emerging wave. The opposite case is represented by an optically thin material, in which all the reflected beams arrive at very close, undistinguishable times. As an heuristic rule we can say that a homogeneous slab is optically thick at a certain wavelength when its thickness in millimeters multiplied by its index of refraction is higher than two, while it is optically thin when the same product is lower than one tenth. Intermediate situations should be considered case by case. We now briefly describe the "thick-thick" and "thin-thick" models.

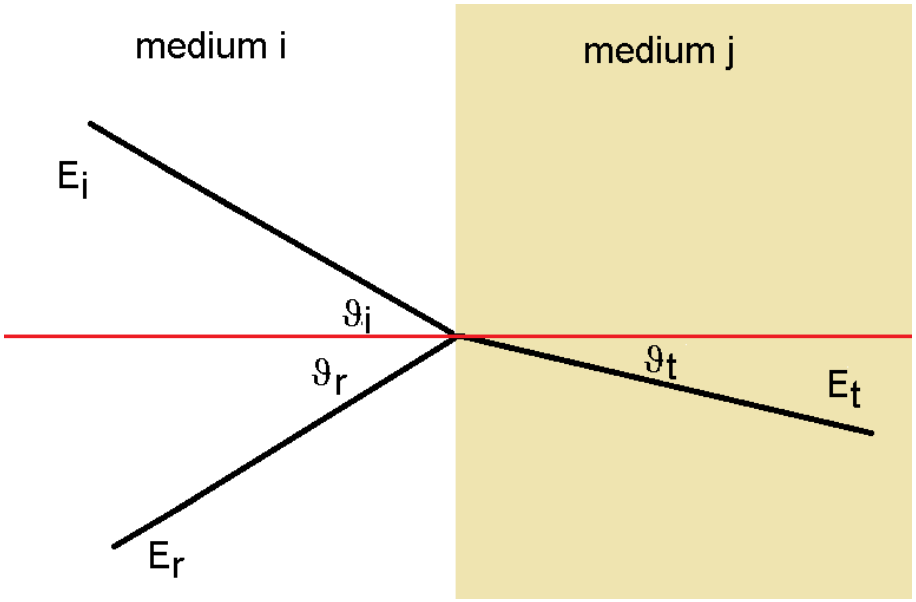

Figure 4.15: Sketch of the reflected and transmitted field amplitudes at the interface between two semi-infinite media.

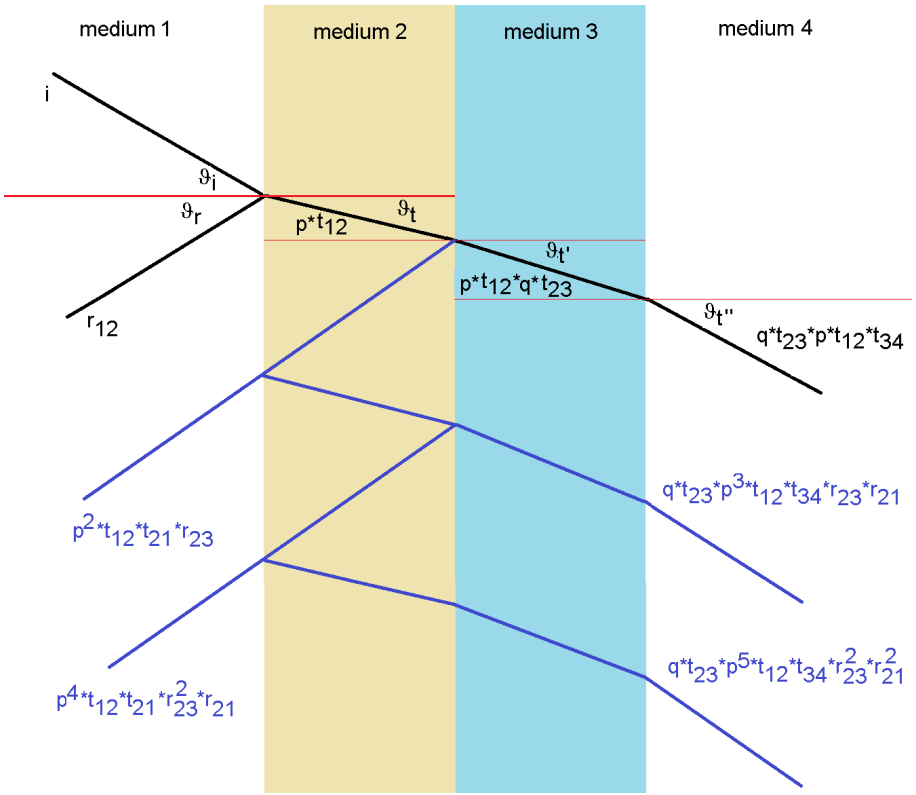

Figure 4.16: Electromagnetic wave impinging on a four materials system ("1234 system"). The black lines represent the first order transmission between all media and the reflection from medium 2. The blue lines represent the second and third order transmissions and reflections of medium 2. The phases acquired by the wave while travelling through medium 2 and medium 3 are p and q, respectively.

The thick-thick model

We first assume that sample and substrate are both optically thick for THz frequencies, in this case the relevant Fresnel relations are

$$R : \frac{\widetilde{E}_{r,Sample}(\omega)}{\widetilde{E}_{r,Reference}(\omega)} = \frac{\widetilde{E}_S(\omega)}{\widetilde{E}_R(\omega)} = \frac{\widetilde{r}_{12}(\omega)}{\widetilde{r}_{1Reference}(\omega)}, \tag{4.42}$$

$$T : \frac{\widetilde{E}_{t,Sample}(\omega)}{\widetilde{E}_{t,Reference}(\omega)} = \frac{\widetilde{E}_S(\omega)}{\widetilde{E}_R(\omega)} = \frac{\widetilde{t}_{12}(\omega)\widetilde{t}_{23}(\omega)e^{i\frac{\omega d}{c}\widetilde{n}_2(\omega)}\widetilde{t}_{34}(\omega)e^{i\frac{\omega D}{c}\widetilde{n}_3(\omega)}}{\widetilde{t}_{13}(\omega)e^{i\frac{\omega d}{c}\widetilde{n}_1(\omega)}\widetilde{t}_{34}(\omega)e^{i\frac{\omega D}{c}\widetilde{n}_3(\omega)}}, \tag{4.43}$$

for reflection (R) and transmission (T) respectively. $\widetilde{E}_{r,Sample}(\omega)$ is the Fourier transform (FT) of the THz field reflected by the sample, $\widetilde{E}_{r,Reference}(\omega)$ the FT of THz reflected by a reference (generally a gold mirror) placed at the exact same position of the sample, $\widetilde{E}_{t,Sample}(\omega)$ the FT of THz transmitted through the 1234 system (Fig.4.16), and $\widetilde{E}_{t,Reference}(\omega)$ the FT of THz transmitted through the "134" system obtained removing the sample (medium 2 is substituted by an extension of medium 1). The thicknesses of sample and substrate are "d" and "D", respectively.

Reflection

From $\frac{\widetilde{E}_S(\omega)}{\widetilde{E}_{gold}(\omega)}\widetilde{r}_{1gold}(\omega) = \widetilde{r}_{12}(\omega) = \frac{\widetilde{n}_1(\omega)\cos(\vartheta_1)-\widetilde{n}_2(\omega)cos(\vartheta_2)}{\widetilde{n}_1(\omega)\cos(\vartheta_1)+\widetilde{n}_2(\omega)cos(\vartheta_2)}$ and assuming $\vartheta_1 = \vartheta_2 = 45°$ and $\widetilde{n}_1(\omega) = 1$ we obtain

$$\frac{\widetilde{E}_S(\omega)}{\widetilde{E}_{gold}(\omega)}\widetilde{r}_{1gold}(\omega) = \frac{1-\widetilde{n}_2(\omega)}{1+\widetilde{n}_2(\omega)}. \tag{4.44}$$

It is possible to describe the reflection of the gold mirror in a simple Drude picture (described in Ch.3): $\widetilde{r}_{1gold}(\omega) = \frac{1-\widetilde{n}_{gold}(\omega)}{1+\widetilde{n}_{gold}(\omega)}$, $\widetilde{n}^2_{gold}(\omega) = \widetilde{\epsilon}_{gold}(\omega) = 1 - \frac{\omega_P^2}{\omega^2+i\Gamma\omega}$ with $\omega_P = 1.3659 \cdot 10^{16} Hz$ and $1/\Gamma = 2.45 \cdot 10^{-14} s$. Assuming for simplicity $\widetilde{r}_{1gold}(\omega) \approx 1$ we have $\frac{\widetilde{E}_S(\omega)}{\widetilde{E}_{gold}(\omega)} \approx \frac{1-\widetilde{n}_2(\omega)}{1+\widetilde{n}_2(\omega)}$, from which

$$\widetilde{n}_2(\omega) \approx \frac{\widetilde{E}_{gold}(\omega) - \widetilde{E}_S(\omega)}{\widetilde{E}_{gold}(\omega) + \widetilde{E}_S(\omega)}. \tag{4.45}$$

As the phase of the reflected THz field depends on the geometry, the main problem in these measurements regards the difficulty to place the reference in the exact same position of the sample. However, it is possible to get rid of the tricky uncertainty in the phase of $\widetilde{E}_{gold}(\omega)$ by evaporating gold on the sample after the measurement of $\widetilde{E}_S(\omega)$.

Transmission

The relevant equation in the transmission of THz radiation for a thick-thick system is

$$\frac{\widetilde{E}_S(\omega)}{\widetilde{E}_R(\omega)} = \frac{\widetilde{t}_{12}(\omega)\widetilde{t}_{23}(\omega)}{\widetilde{t}_{13}(\omega)} e^{i\frac{\omega d}{c}(\widetilde{n}_2(\omega)-\widetilde{n}_1(\omega))}. \tag{4.46}$$

Substituting the Fresnel coefficients for all normal incidences ($\vartheta_1 = \vartheta_2 = \vartheta_3 = 0$) and $\widetilde{n}_1(\omega) = 1$ we get

$$\frac{\widetilde{E}_S(\omega)}{\widetilde{E}_R(\omega)} = \frac{2}{1+\widetilde{n}_2(\omega)} \frac{2\widetilde{n}_2(\omega)}{\widetilde{n}_2(\omega)+\widetilde{n}_3(\omega)} \frac{1+\widetilde{n}_3(\omega)}{2} e^{-\frac{\omega d}{c}k_2(\omega)} e^{i\frac{\omega d}{c}(n_2(\omega)-1)}. \tag{4.47}$$

Once $\frac{\widetilde{E}_S(\omega)}{\widetilde{E}_R(\omega)}$ is measured and $\widetilde{n}_3(\omega)$ is known, the optical constants of the sample are obtained solving numerically the appropriate system of equations obtained from eq.4.47 for each value of the frequency. On the other hand, if we assume a low absorbing or highly refracting material then the $\widetilde{n}_2(\omega)$ and $\widetilde{n}_3(\omega)$ in eq.4.47 can be taken as real. Writing in this case the ratio $\frac{\widetilde{E}_S(\omega)}{\widetilde{E}_R(\omega)}$ as amplitude multiplied phase, $Ae^{i\Delta\phi}$, we get $\Delta\phi \approx \frac{\omega d}{c}(n_2(\omega)-1)$ and $A \approx \frac{2}{1+n_2(\omega)} \frac{2n_2(\omega)}{n_2(\omega)+n_3(\omega)} \frac{1+n_3(\omega)}{2} e^{-\frac{\omega d}{c}k_2(\omega)}$, then

$$n_2(\omega) \approx 1 + \frac{c\Delta\phi}{\omega d} \tag{4.48}$$

$$k_2(\omega) \approx -\frac{c}{\omega d} \ln \frac{A(n_2(\omega)+1)(n_2(\omega)+n_3(\omega))}{2n_2(\omega)(1+n_3(\omega))}. \tag{4.49}$$

In this last case when the substrate is replaced by air/vacuum nothing changes in the expression for $n_2(\omega)$, while $k_2(\omega) \approx -\frac{c}{\omega d} \ln \frac{A(n_2(\omega)+1)^2}{4n_2(\omega)}$.

The thin-thick model

We now assume that the sample is optically thin and the substrate is optically thick. The total reflection, $\widetilde{r}_{total}(\omega)$, in medium 1 and transmission, $\widetilde{t}_{total}(\omega)$, in medium 4 satisfy:

$$\widetilde{r}_{total}(\omega) = \frac{\widetilde{r}_{12}(\omega) + \widetilde{r}_{23}(\omega)e^{i2\frac{\omega d}{c}\widetilde{n}_2(\omega)}}{1 - \widetilde{r}_{23}(\omega)\widetilde{r}_{21}(\omega)e^{i2\frac{\omega d}{c}\widetilde{n}_2(\omega)}}, \tag{4.50}$$

$$\widetilde{t}_{total}(\omega) = \frac{\widetilde{t}_{34}(\omega)e^{i\frac{\omega D}{c}\widetilde{n}_3(\omega)}\widetilde{t}_{12}(\omega)\widetilde{t}_{23}(\omega)e^{i\frac{\omega d}{c}\widetilde{n}_2(\omega)}}{1 - \widetilde{r}_{23}(\omega)\widetilde{r}_{21}(\omega)e^{i2\frac{\omega d}{c}\widetilde{n}_2(\omega)}}. \tag{4.51}$$

Reflection

Recalling that $\widetilde{r}_{total}(\omega) = \frac{\widetilde{E}_S(\omega)}{\widetilde{E}_R(\omega)}\widetilde{r}_{1R}(\omega)$ we can write $\frac{\widetilde{r}_{12}(\omega)+\widetilde{r}_{23}(\omega)e^{i2\frac{\omega d}{c}\widetilde{n}_2(\omega)}}{1-\widetilde{r}_{23}(\omega)\widetilde{r}_{21}(\omega)e^{i2\frac{\omega d}{c}\widetilde{n}_2(\omega)}} = \frac{\widetilde{E}_S(\omega)}{\widetilde{E}_R(\omega)}\widetilde{r}_{1R}(\omega)$. For $\vartheta_1 = \vartheta_2 = \vartheta_3 = 45°$ and $\widetilde{n}_1(\omega) \approx \widetilde{r}_{1R}(\omega) \approx 1$ we get

$$\frac{\widetilde{E}_S(\omega)}{\widetilde{E}_R(\omega)} \approx \frac{\frac{1-\widetilde{n}_2(\omega)}{1+\widetilde{n}_2(\omega)} + \frac{\widetilde{n}_2(\omega)-\widetilde{n}_3(\omega)}{\widetilde{n}_2(\omega)+\widetilde{n}_3(\omega)}e^{i2\frac{\omega d}{c}\widetilde{n}_2(\omega)}}{1 - \frac{\widetilde{n}_2(\omega)-1}{\widetilde{n}_2(\omega)+1}\frac{\widetilde{n}_2(\omega)-\widetilde{n}_3(\omega)}{\widetilde{n}_2(\omega)+\widetilde{n}_3(\omega)}e^{i2\frac{\omega d}{c}\widetilde{n}_2(\omega)}}, \tag{4.52}$$

that can be solved numerically with a method like Newton-Raphson once $\widetilde{n}_3(\omega)$ is known and $\frac{\widetilde{E}_S(\omega)}{\widetilde{E}_R(\omega)}$ has been calculated from the measurements. It's also possible to apply the "thin film" approximation that consists in assuming $\frac{\omega d}{c}\widetilde{n}_2(\omega) \ll 1$:

$$\frac{\widetilde{E}_S(\omega)}{\widetilde{E}_R(\omega)} \approx \frac{1 - \widetilde{n}_3 + i\frac{\omega d}{c}(\widetilde{n}_2 - \widetilde{n}_3 + \widetilde{n}_2^2 - \widetilde{n}_2\widetilde{n}_3)}{1 + \widetilde{n}_3 - i\frac{\omega d}{c}(\widetilde{n}_2^2 - \widetilde{n}_2\widetilde{n}_3 - \widetilde{n}_2 + \widetilde{n}_3)}. \tag{4.53}$$

If we use the general identity $\widetilde{n}_2^2(\omega) = \widetilde{\epsilon}_2(\omega) = 1 + i\frac{\widetilde{\sigma}_2(\omega)}{\omega\epsilon_0}$, omit the other $i\frac{\omega d}{c}$ terms and recall the free space impedance definition $Z_0 = \frac{1}{c\epsilon_0} = 376.7\,\Omega$ we obtain $\frac{\widetilde{E}_S(\omega)}{\widetilde{E}_R(\omega)} \approx \frac{1-\widetilde{n}_3(\omega)-Z_0 d\widetilde{\sigma}_2(\omega)}{1+\widetilde{n}_3(\omega)+Z_0 d\widetilde{\sigma}_2(\omega)}$ and, hence,

$$\widetilde{\sigma}_2(\omega) \approx \frac{1}{Z_0 d}\left(\frac{\widetilde{E}_R(\omega) - \widetilde{E}_S(\omega)}{\widetilde{E}_R(\omega) + \widetilde{E}_S(\omega)} - \widetilde{n}_3(\omega)\right) \tag{4.54}$$

Transmission

Recalling that $\widetilde{t}_{total}(\omega) = \frac{\widetilde{E}_S(\omega)}{\widetilde{E}_R(\omega)}\widetilde{t}_{13}(\omega)e^{i\frac{\omega d}{c}\widetilde{n}_1(\omega)}\widetilde{t}_{34}(\omega)e^{i\frac{\omega D}{c}\widetilde{n}_3(\omega)}$ we can write

$$\frac{\widetilde{t}_{12}(\omega)\widetilde{t}_{23}(\omega)e^{i\frac{\omega d}{c}\widetilde{n}_2(\omega)}}{1 - \widetilde{r}_{23}(\omega)\widetilde{r}_{21}(\omega)e^{i2\frac{\omega d}{c}\widetilde{n}_2(\omega)}} = \frac{\widetilde{E}_S(\omega)}{\widetilde{E}_R(\omega)}\widetilde{t}_{13}(\omega)e^{i\frac{\omega d}{c}\widetilde{n}_1(\omega)}. \tag{4.55}$$

For $\vartheta_1 = \vartheta_2 = \vartheta_3 = 0$ and $\widetilde{n}_1(\omega) = 1$ the last equation reduces to

$$\frac{\frac{2}{1+\widetilde{n}_2(\omega)}\frac{2\widetilde{n}_2(\omega)}{\widetilde{n}_2(\omega)+\widetilde{n}_3(\omega)}e^{i\frac{\omega d}{c}\widetilde{n}_2(\omega)}}{1 - \frac{\widetilde{n}_2(\omega)-1}{\widetilde{n}_2(\omega)+1}\frac{\widetilde{n}_2(\omega)-\widetilde{n}_3(\omega)}{\widetilde{n}_2(\omega)+\widetilde{n}_3(\omega)}e^{i2\frac{\omega d}{c}\widetilde{n}_2(\omega)}} = \frac{\widetilde{E}_S(\omega)}{\widetilde{E}_R(\omega)}\frac{2}{1+\widetilde{n}_3(\omega)}e^{i\frac{\omega d}{c}} \tag{4.56}$$

that can be solved numerically once $\widetilde{n}_3(\omega)$ is known and $\frac{\widetilde{E}_S(\omega)}{\widetilde{E}_R(\omega)}$ has been calculated from the measurements. It's also possible to apply the "thin film" approximation that consists in assuming $\frac{\omega d}{c}\widetilde{n}_2(\omega) \ll 1$:

$$\frac{\widetilde{E}_S(\omega)}{\widetilde{E}_R(\omega)} \approx \frac{(1 + \widetilde{n}_3(\omega))(1 + i\frac{\omega d}{c}\widetilde{n}_2(\omega))}{(1 + i\frac{\omega d}{c})1 + \widetilde{n}_3 - i\frac{\omega d}{c}(\widetilde{n}_2^2 - \widetilde{n}_2\widetilde{n}_3 - \widetilde{n}_2 + \widetilde{n}_3)}. \tag{4.57}$$

Doing now a similar substitution and omission as the one done for reflection we obtain $\frac{\widetilde{E}_S(\omega)}{\widetilde{E}_R(\omega)} \approx \frac{1+\widetilde{n}_3(\omega)}{1+\widetilde{n}_3(\omega)+Z_0 d\widetilde{\sigma}_2(\omega)}$, hence

$$\widetilde{\sigma}_2(\omega) \approx \frac{1+\widetilde{n}_3(\omega)}{Z_0 d} \frac{\widetilde{E}_R(\omega) - \widetilde{E}_S(\omega)}{\widetilde{E}_S(\omega)}. \tag{4.58}$$

4.3.2 Test of the THz time domain spectrometer

In order to develop intense pulses of THz radiation suitable for pump-probe experiments, first we realize a standard THz-TDS setup, along with the software for controlling the experiment and analyzing the data. The setup, based on the generation of THz pulses by focusing first and second harmonic of the $1\,KHz$ pulsed laser source in air, is shown in Fig.4.17. Here, the THz radiation is used as a probe and detected, with and without the sample placed in the marked blue spot, with a delayed laser pulse through electro-optical sampling.

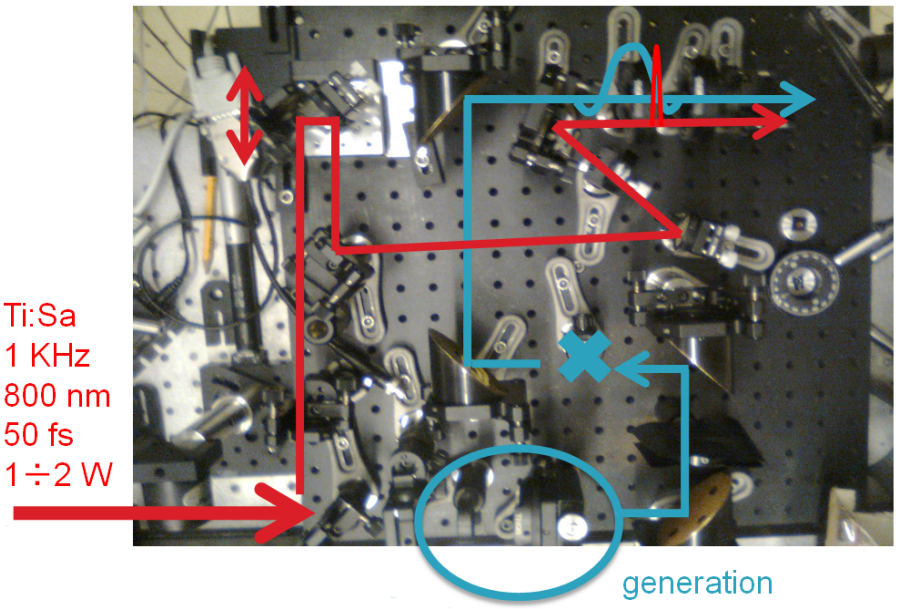

Figure 4.17: terahertz time-domain spectroscopy setup developed in our lab. The THz radiation is generated from a plasma in air and detected by electro-optical sampling as a function of sampling-THz delay. In blue the path of the THz light, in red the path of the $\approx 800\,nm$ pulses. The blue spot marks the position of the sample.

$CuGeO_3$ is an inorganic material that exhibit the spin-Peierls transition at $14\,K$[106, 107] and shows intriguing optical properties in the THz region of the electromagnetic spectrum: an IR-active spin gap at $1.32\,THz$[108, 109] at low temperature marks the spin-Peierls transition, while a $Cu-O$ IR-active vibrational mode is present at about $1.47\,THz$[105]. As test benchmark for the optical system and the analysis approach we developed, we studied the

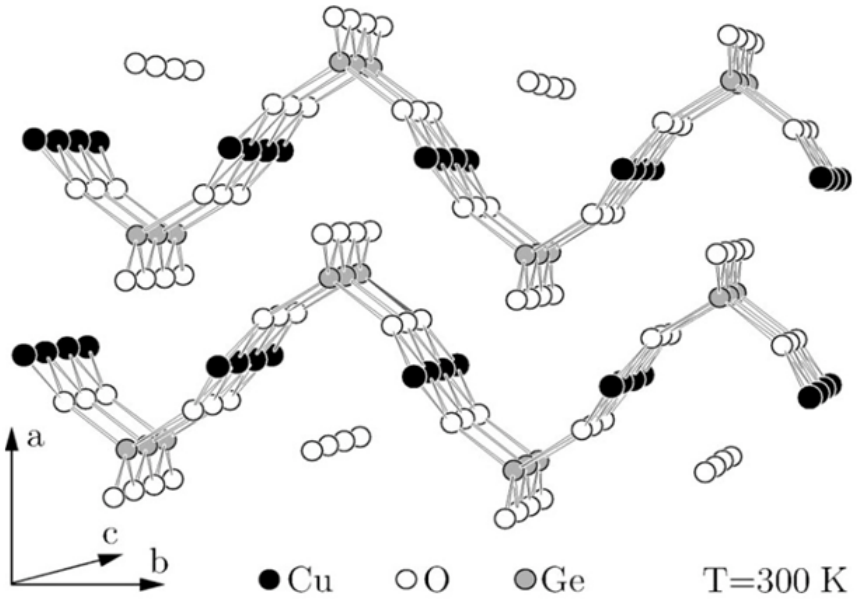

Figure 4.18: Room temperature structure of $CuGeO_3$ from [105].

phononic mode at room temperature. The structure of $CuGeO_3$ is characterized by Cu^{2+} and Ge^{4+} chains parallel to the c axis linked via the oxygen atoms. The layers in the $b-c$ plane are weakly coupled along the a axis (Fig.4.18). When the THz polarization is perpendicular to the chains there is a marked absorption at $\approx 1.5\,THz$ while no such absorption is present when the terahertz radiation is polarized parallel to the chains. In Fig.4.19 the results are reported for a $\approx 10\,\mu m$ thick $b-c$ oriented sample. The "ringing" is attributed to the fact that the simplest model for data extraction has been used ("thick-thick model", eqs.4.48,4.49) that neglects high-order Fresnel coefficients.

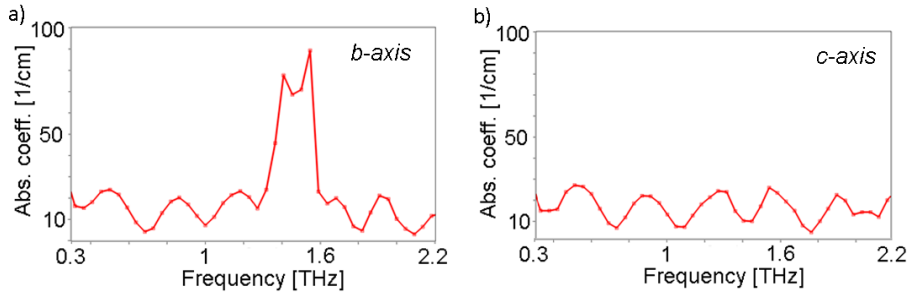

Figure 4.19: Polarization-dependent absorption of terahertz light from copper-germanate.

4.3.3 Ultra-short laser sources

We briefly introduce the two commercial laser systems used to perform the pump-probe experiments. Starting with the high-power and low repetition rate

laser source ($1\,KHz$, $2\,mJ/pulse$) we performed experiments with THz radiation, while a low-power high-repetition rate system ($250\,KHz$, $5\,\mu J/pulse$) has been used for optical/IR pumping. Both systems are composed by an oscillator, that is the source of the highly anisotropic temporal emission, and by an amplification stage.

Mode locking

The oscillator produces the ultra-short pulses through the mode-locking technique. The mode-locking is funded on the properties of an active medium ($Ti{:}Al_2O_3$ in this case) and on the geometry of the cavity: it induces a constant phase-difference between the modes of the resonant cavity, as reported in the heuristic reasoning that follows[110].

Consider the electric field within a cavity as the sum of all the modes sustained by the cavity. In particular, a l-long cavity sustains modes at wavelengths $\lambda = \frac{2l}{m}$ with m integer. The frequency difference $\Delta\nu$ between two nearest modes is

$$\Delta\nu = \frac{\Delta\lambda}{c} = \frac{2l}{c}\left(\frac{1}{m} - \frac{1}{m+1}\right), \tag{4.59}$$

hence, assuming that all the modes oscillate without phase-correlations but with the same amplitude, the total electric field $E(t)$ is

$$E(t) = \sum_{n=-N}^{N} E_0 e^{i(\omega_0 + n\Delta\omega)t + in\phi} = e^{i\omega_0 t} A(N,t), \tag{4.60}$$

where n is the difference between the index of the mode and the one at angular frequency ω_0, and $A(N,t) = \sum_{n=-N}^{N} E_0 e^{in(\Delta\omega t+\phi)}$. The angular frequency $\Delta\omega$ is almost independent of n, in fact if $n_0 >> N$

$$\Delta\omega = \frac{4\pi l}{c}\left(\frac{1}{n_0+n} - \frac{1}{n_0+n+1}\right) = \frac{4\pi l}{c}\frac{1}{(n_0+n)(n_0+n+1)} \approx \frac{4\pi l}{c n_0^2}. \tag{4.61}$$

The sum in eq.4.60 can be rewritten as

$$\sum_{n=-N}^{N} E_0 e^{in\tau} = E_0\left\{\sum_{n=0}^{N} e^{in\tau} + \sum_{n=0}^{N} e^{-in\tau} - 1\right\}, \tag{4.62}$$

where $\tau = \Delta\omega t + \phi$ and the first two terms are geometrical, then

$$A(N,\tau) = E_0 \frac{sin(\tau\frac{2N-1}{2})}{sin(\frac{\tau}{2})}. \tag{4.63}$$

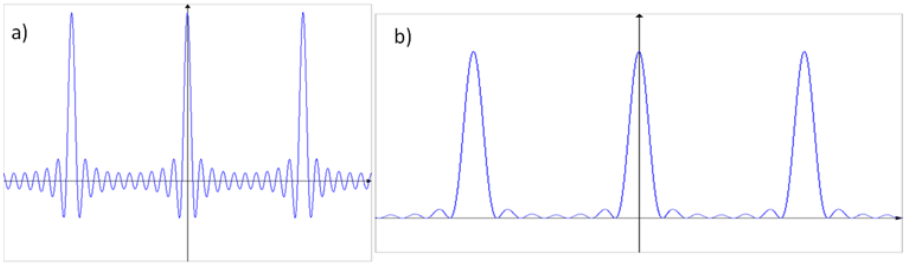

Figure 4.20: In (a) a schematic representation of $A(\tau)$. In b) $A^2(\tau)$ is reported.

Kerr lens mode-locking

$Ti{:}Al_2O_3$ has an intensity-dependent index of refraction, $n = n_0 + n_{Kerr}I$, where I is the light's intensity and n_{Kerr} is positive. n is almost constant, equal to n_0, for small I. The profile $I(x)$ of the transverse intensity of a laser source is generally gaussian and the intensity is higher in the central part of the beam respect to the extrema. Hence, by Kerr-Lens effect, the material has a higher index of refraction in the center and focuses the beam, acting as a lens. Inserting a fenditure at the end of the cavity is possible to optimize the focus of the beam, obtaining ultra-short pulses of laser radiation $(1 - 100\,fs)$.

The amplifier

The chirped-pulse amplification scheme consists of three steps: the stretcher, the amplifier and the compressor. The stretcher has gratings that broaden the laser pulse in the time-domain to minimize the risks of damaging the amplfying crystal. Hence, the pulse is amplified by an active medium ($Ti{:}Sa$). Finally, the pulse is compressed back following a determined optical path across the gratings.

The laser systems

$1\,KHz$ system:

- Coherent Mira oscillator ($Ti{:}Al_2O_3$): $20\,fs$ pulses with $\lambda = 800 \pm 40\,nm$, $350\,mW$ of power at $76\,MHz$ of repetition rate, pumped with Coherent verdi ($Nd{:}YVO_4$, $\lambda = 532\,nm$, and $P = 5\,W$)

- Coherent Legend amplifier ($Ti{:}Sa$): $50\,fs$ pulses with $\lambda = 800 \pm 30\,nm$, $2\,W$ of power at $1\,KHz$ of repetition rate, pumped with Coherent Legend ($Nd{:}YLF$, $\lambda = 527\,nm$, and $P = 20\,W$)

$250\,KHz$ system:

- Mira Seed oscillator ($Ti{:}Al_2O_3$): $50\,fs$ pulses with $\lambda = 800 \pm 40\,nm$, $550\,mW$ of power at $74\,MHz$ of repetition rate, pumped with Coherent verdi V18 ($P = 18\,W$)

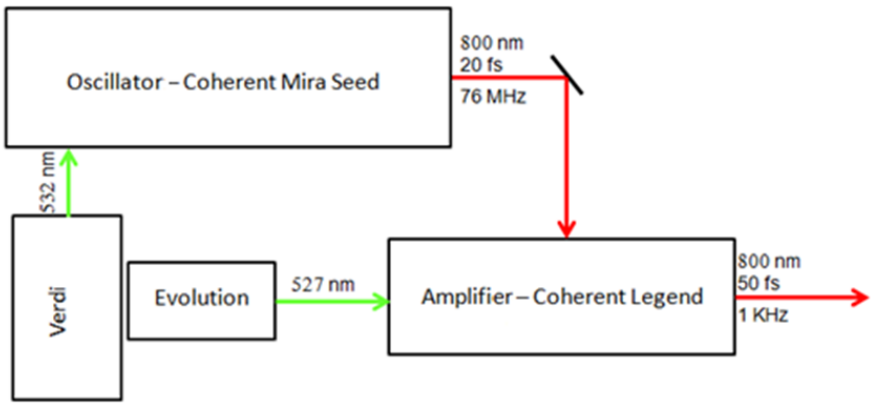

Figure 4.21: Sketch of the $1\,KHz$ repetition rate laser system. Figure from [111].

- Rega 9050 amplifier ($Ti{:}Sa$): $50\,fs$ pulses with $\lambda = 800 \pm 30\,nm$, $1.2\,W$ of power at $< 300\,KHz$ of repetition rate, pumped with Coherent verdi V18 ($P = 18\,W$)
- OPA, λ tunable in the $1100 - 2400\,nm$ range, $P \leq 300\,mW$

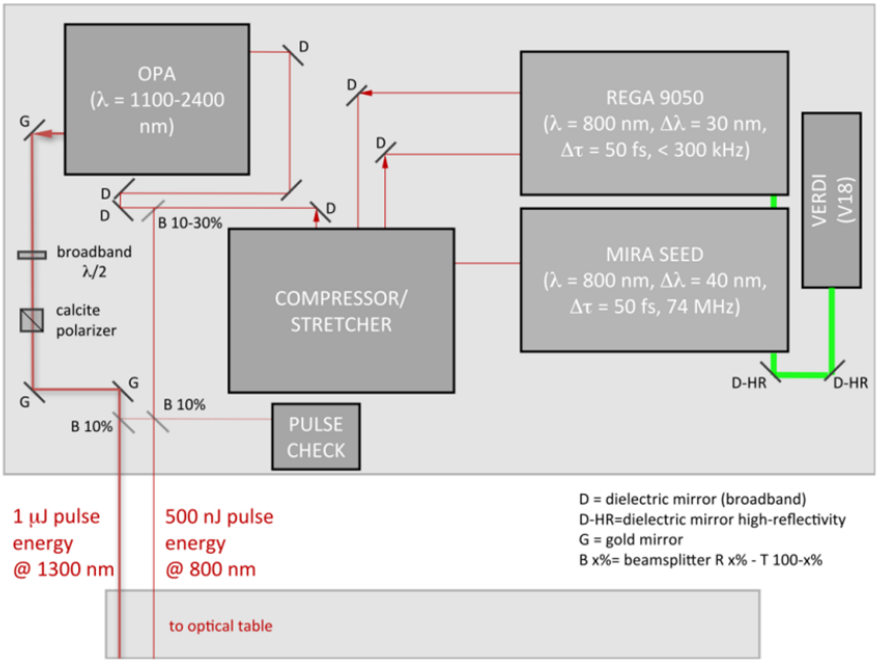

Figure 4.22: Sketch of the $250\,KHz$ laser system. The OPA is used to generate pump pulses in the mid-infrared region of the electromagnetic spectrum. Figure from [112].

Chapter 5

Hubbard exciton revealed by time-domain optical spectroscopy in YVO_3

This chapter begins with an overview on the material under investigation: the Mott insulator YVO_3. In the following we show the pump-probe reflectivity measurements, and we propose a novel methodology for data analysis (see Ch.3). Such analysis allows to separate thermal and non-thermal contribution to the optical transients, and to demonstrate that the total spectral weight (SW) of the two lowest lying optical excitations is conserved. The $1.8\,eV$ transition is hence identified as a kinetic-energy based Hubbard exciton, and a mechanism of spin disorder is proposed to account for the long timescale dynamics observed.

5.1 Introduction

The physical properties of materials characterized by strong electron-electron interactions are determined by the competitive minimization of the potential energy and the kinetic energy of the electrons. While the potential energy is lowest for localized electrons, the tendency to a metallic state increases it at the expense of kinetic energy. The fine tuning of the system parameters results in the exotic ordering phenomena characterizing transition metal oxides (TMOs)[113]. In a Mott-Hubbard insulator the lowest electronic excitation across the gap creates, in the most simple case, an empty site (holon in the lower Hubbard band) and a doubly occupied site (doublon in the upper Hubbard band)[114]. In the single-band Hubbard model, the energy of this transition is solely determined by the on-site Coulomb repulsion between electrons leading to an effective energy cost U. Typically, holon and doublon are not bound to each other, but more composite excited states have been predicted by the extended Hubbard model including non-

local interactions[115–119]. In particular, a new kind of bound state between a holon and a doublon was recently introduced and named Hubbard exciton (HE)[120–123]. While the formation of HEs can be driven by a drop of Coulomb energy[124, 125], as in simple semiconductors, a kinetic energy loss could further stabilize the excitonic state in magnetic environments[122, 126–128]. Non-localized HEs have been extensively studied in the framework of high-temperature superconductivity[129, 130] in relation with the proposed kinetic energy driven formation of the condensate[39, 131, 132].

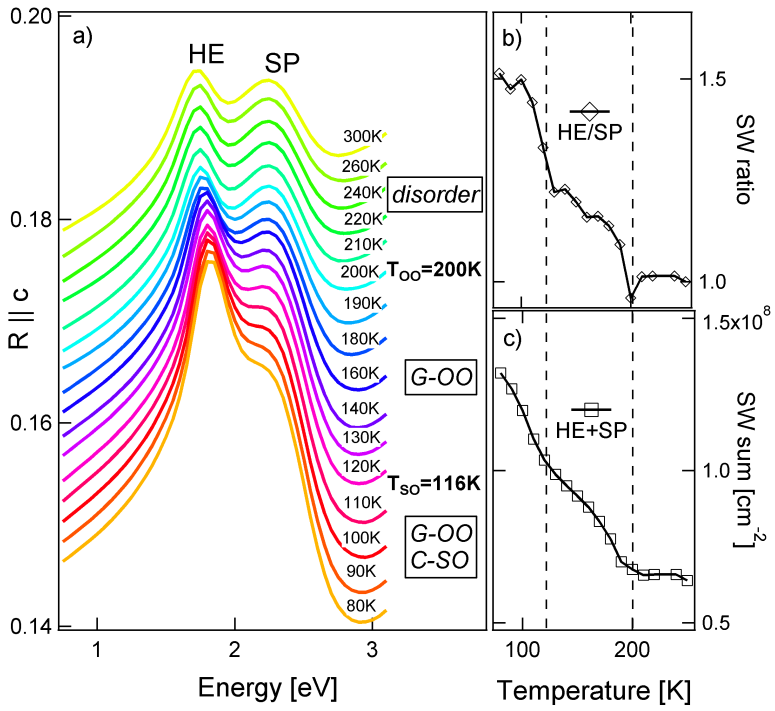

Figure 5.1: Reflectivity for $E||c$ as a function of temperature of YVO_3 obtained by ellipsometry data (a). The ratio between the spectral weight of the excitonic and single particle band (b) increases rapidly while entering the G-OO phase and further increases at the spin ordering temperature. Both the SP and the HE spectral weights raise upon cooling (c). In (b) and (c) the dashed lines represent the transition temperatures towards the orbital ordering (T_{OO}=200 K) and the additional spin ordering (T_{SO}=116 K). In (b) the ratio is normalized to the value at 300 K. Note that the reflectivity measurements in (a) are displaced for clarity from the measurement at 80 K.

In this report we show that an extended HE picture rationalizes the optical properties of YVO_3, a case-study for Mott-insulating TMOs. In this scenario, the optical transition (see Fig.5.1) observed in reflectivity at 2.4 eV reflects the "single-particle" band (SP) whereas the one at 1.8 eV is attributed to an excitonic resonance related to a gain of kinetic energy[47]. Our pump-probe spectroscopic measurements in the 1.65-2.75 eV range allow to determine the temporal evolution of the spectral weight $SW = \int_0^\infty \sigma_1(\omega)d\omega$ in the optical conductivity $\sigma_1(\omega)$ of each absorption band separately. We find that the spectral weight is directly transferred between the two peaks, confirming the excitonic

nature of the low-energy feature. Together with this, we measured both thermal and non-thermal effects and quantified the kinetic energy contribution to the formation of the HE. Our study provides a new methodology, based on both static and time-domain spectroscopy, that can be used to unravel the complex nature of high-energy excitations in insulating TMOs and, more broadly, to study the kinetic energy-based mechanisms in strongly-correlated materials.

Owing to multiple temperature-induced magnetization reversals[133] accompanied by a series of structural[134], magnetic[135], and orbital phase transitions[136], the Mott insulator YVO_3 became a case-study among TMOs. At room temperature YVO_3 has a *Pbnm* orthorhombic crystal structure, where each VO_6 octahedron is tilted and distorted. The V^{3+} ions have a $3d^2$ electronic configuration[137] so that two electrons occupy the t_{2g} orbitals. At 200 K a phase transition to a monoclinic phase ($Pb11$[138] or $P2_1/c$[134, 139, 140]) occurs with G-type orbital order (G-OO). In this state, the d_{yz} or d_{zx} orbitals are alternately occupied both in the *ab* plane and along the *c* axis (Fig.5.2e). While still monoclinic and G-OO, at T_{SO}=116 K a C-type spin order (C-SO) emerges, characterized by an antiferromagentic (AFM) spin configuration in the *ab* plane and ferromagnetic order (FM) along the *c* axis (Fig.5.2f). For further cooling below $T_{Néel}$=77 K a structural, orbital, and magnetic transition occurs: the system recovers the *Pbnm* crystalline structure while the orbital ordering switches to C-type (C-OO) and the spin order to G-type (G-SO)[141–144]. The low-temperature phase will not be further discussed in the following because the crystals tend to break at the low-temperature phase transition often leading to a loss of thermal contact[47] and strong average heating.

5.2 Results

All phase transitions can be identified by monitoring the optical properties of YVO_3. The region of the optical spectra that is particularly sensitive to the orbital physics is the visible range, just above the gap of about 1.6 eV. The two peaks characterizing the reflectivity with energies of 1.8 eV (HE) and 2.4 eV (SP) are largely debated[47, 138, 143–150] and commonly assigned to $d_i^2 d_j^2$-$d_i^1 d_j^3$ transitions between two different V_i and V_j sites[138, 148]. However, the assignment to different multiplets to the peaks observed in the optical data has been controversial[47, 138, 143, 148]. For $E||c$ both excitations at 1.8 and 2.4 eV gain SW with decreasing temperature and approaching the spin ordering transition at T_{SO}=116 K (Fig.5.1c), indicating that they both correspond to the same high-spin multiplet[47]. The SW gain with decreasing temperature is much stronger for the lower peak, which tentatively has been attributed to excitonic behavior. In this scenario, the lower peak is an excitonic resonance, i.e. a nearly bound state within the continuum. This is supported by a comparison of optical data with band-structure calculations and photoemission data[47]. In fact from Hund's rules we expect the kinetic energy contribution to the formation of the Hubbard exciton to be more relevant for parallel alignment

of spins such as along c in the C-SO phase[122].

In order to distinguish the effects of temperature and spin/orbital disorder we performed pump-probe reflectivity measurements. The complex dielectric function $\varepsilon(\omega)$ was measured by ellipsometry, for details see Ref.[47]. The static normal-incidence reflectivity $R(\omega)$ reported in Fig.5.1 was calculated from $\varepsilon(\omega)$. Broadband super-continuum probe experiments combined with an ultrafast optical pump at 1.6 eV were performed on freshly polished ac oriented YVO_3 samples mounted on the cold finger of a helium-flow cryostat. The reflectivity changes as a function of pump-probe delay $\frac{\Delta R}{R}(\omega, t) = \frac{R(\omega,t)-R(\omega)}{R(\omega)}$ induced by 80 fs pump pulses (E_{pump}=1.6 eV, fluence<4 mJ/cm^2, at 40 KHz repetition rate, and polarization parallel to the a axis) were measured as a function of energy (for 1.65 eV $< E_{probe} <$ 2.75 eV) and temperature. The linearity of the response was checked in all phases up to 8 mJ/cm^2.

The three phases are characterized by the different responses summarized in Fig.5.2 for probe polarization parallel to the c axis (see Par.5.5 for the intermediate temperatures). At room temperature, the pump-probe measurements are solely characterized by a very fast negative variation of the reflectivity (decay time $\tau \approx 0.5$ ps) extending over the investigated spectral region (Fig.5.2a). On the contrary, the low-temperature phases are characterized by a more composite optical response with fast and slow components, confirming previously reported single-color measurements[151, 152]. The time-domain reflectivity measurements in the G-OO phase (116 K < T < 200 K) are characterized by a slow negative response centered at 1.94 eV (Fig.5.2b), which gets more pronounced as the temperature is lowered (Fig.5.2c). Finally, entering the C-SO phase (80 K < T < 116 K) a positive variation of the reflectivity appears at energies higher than 2.1 eV.

5.3 Methods

Our time-domain spectroscopic technique offers a direct view on the pump-induced changes of the reflectivity over a broad frequency range. This has significant advantages compared to a single-color pump-probe experiment. It allows, for instance, to determine the time-dependent spectral weight of the different features characterizing the optical response. The observation of a direct transfer of SW between the HE and SP band in YVO_3 is the central experimental result of this study.

We start our analysis from a model for the static data. We fitted ϵ_2 by a sum of six gaussian peaks and a Tauc-Lorentz oscillator for the transition at lower energy (HE), ϵ_1 by the Kramers-Kronig consistent functional form. With those line-shapes, which have been justified and extensively used to address amorphous and locally-disordered materials[45, 153], we obtain static fits of very good quality (Fig.5.3). These are the dielectric expressions used:

$$\epsilon_2(\omega) = L_a(\omega) + L_b(\omega) + ... + L_g(\omega), \tag{5.1}$$

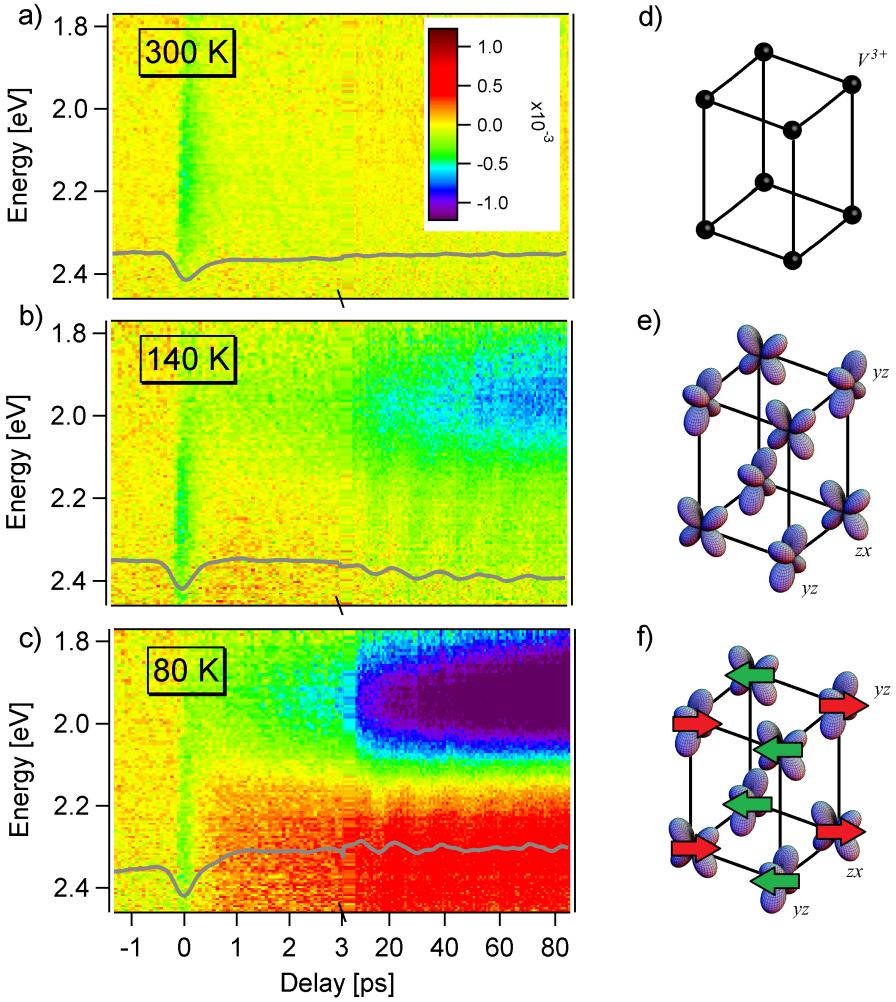

Figure 5.2: Broadband transient reflectivity spectra. Transient reflectivity as a function of energy and pump-probe delay for the three different phases: (a) disordered, T=300 K; (b) G-type orbital order, T=140 K; (c) C-type spin order, T=80 K. Gray lines report the transient reflectivity at the fixed energy of 2.33 eV as retrieved in standard single-color pump-probe measurements. The oscillatory trend has been assigned to acoustic vibrations[151] and will be ignored. For each panel, the respective ordering patterns are sketched on the right hand side (d, e, f).

where $L_a(\omega) = \frac{1}{\omega}\frac{a\omega_a\gamma_a(\omega-gap)^2}{(\omega^2-\omega_a^2)^2+\omega^2\gamma_a^2}$ if $\omega > gap$ and $L_a(\omega) = 0$ elsewhere. $L_c...L_g$ are analogous of

$$L_b(\omega) = b\left(e^{-4ln2\frac{(\omega-\omega_b)^2}{\gamma_b^2}} - e^{-4ln2\frac{(\omega+\omega_b)^2}{\gamma_b^2}}\right), \tag{5.2}$$

where a,b,c... are the amplitudes, ω_i and γ_i the central frequencies and widths for $i = a, b, c....$ The real part of the dielectric function is

$$\epsilon_1(\omega) = 1 + D_a(\omega) + D_b(\omega) + ... + D_g(\omega), \tag{5.3}$$

where $D_a(\omega)$ has the form reported in Jellison's paper[49, 50] and the other terms ($D_b(\omega)...D_g(\omega)$) are the proper sums of Dawson's functions[44]. By simultaneous fitting of both the real and imaginary part of the dielectric constant we were able to obtain a series of continuously-varying parameters. In the c-axis fitting the gaussian centered at 33000 cm^{-1} (≈4 eV) loses SW below 140 K: we left this oscillator free to vary as attempts to block it produces a much worse fit. For the same reason we bind the central frequency of another oscil-

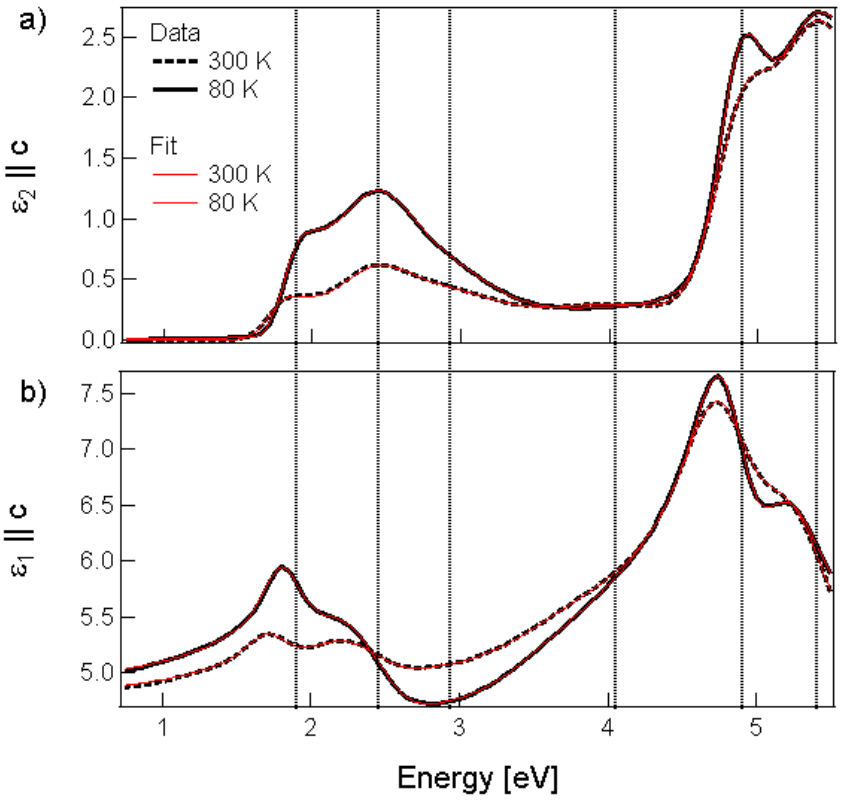

Figure 5.3: Dielectric constant of YVO_3 for $E||c$ at 80 K and 300 K. a) Imaginary and b) real part of the dielectric constant of YVO_3 measured by ellipsometry[47] along the c axis at 80 K and 300 K. The vertical dashed lines mark the positions of the central frequencies of the oscillators used to perform the static fitting procedure (see text).

lator at 23000 cm^{-1} (≈2.9 eV). These assumptions are justified by the overall

good fits of the static optical properties. It should be noted that these approximations, which have been made to have a good description of the static optical properties outside of the interest range for the time domain data, do not affect the outcome of the time-domain fits. This was verified by performing time domain fits with different sets of parameters. The spectral weights have been computed as $\int_0^{23000} \omega\epsilon_2(\omega)d\omega$, with ω in cm^{-1} and $\epsilon_2(\omega)$ composed only of the HE peak or the SP peak.[1]

In order to calculate the pump-induced evolution of the SW of the two bands from the transient reflectivity data, we proceed as follows. We consider the model used to fit the static ellipsometry data, we calculate the equilibrium reflectivity (R_0), and we fit the measured transient reflectance ($\Delta R_{exp}(t)/R_{exp}$) with a differential model $(R(t) - R_0)/R_0$, where $R(t)$ is a model for the perturbed reflectivity obtained by variation of the parameters used to fit the equilibrium data as a function of pump-probe delay t. The values of the oscillators parameters obtained by this fitting procedure at different times are used to calculate the evolution of the spectral weight:

$$\Delta SW(t) = SW^{pumped}(t) - SW^{static}(T), \tag{5.4}$$

where $SW^p(t)$ is calculated from the fitting parameters of $R(t)$ and $SW^s(T)$ is obtained from the static reflectivity at temperature T (both SW are calculated by the numerical intergration described earlier).

Among the 21 parameters used to fit the features in the static $\varepsilon(\omega)$, the minimal set of parameters needed to obtain good differential fits at all temperatures and times contains only the following four: the amplitude, central frequency, and width of the oscillator describing the HE and the amplitude of the SP one. Fig.5.4a,b,c show typical fits obtained for the fast (blue) and slow response (red) in the different phases. The obtained values for the temporal evolution of the oscillator parameters are used to calculate the time-domain evolution of the spectral weight. The variation of the spectral weight for the two bands in time is calculated independently as the difference between the SW calculated for the model at a specific time ($SW^{pumped}_{HE,SP}(t)$) minus the static spectral weight ($SW^{static}_{HE,SP}$) (each spectral weight is calculated by numerical integration of the optical conductivity describing the band).

5.4 Discussion

The time dependence of $\Delta SW(t)$ of HE and SP as a function of the pump-probe delay t is reported in Fig.5.4d,e,f for three representative temperatures. The fast response (t < 3 ps) in all phases is entirely described by a variation of the SP peak while the HE seems to be unaffected by photo-excitation in the first few picoseconds. This evidence can be rationalized as ground state

[1] It should be noted that the SW reported in Ref.[47] are computed from lorentzian lineshapes, giving rise to slightly different absolute values.

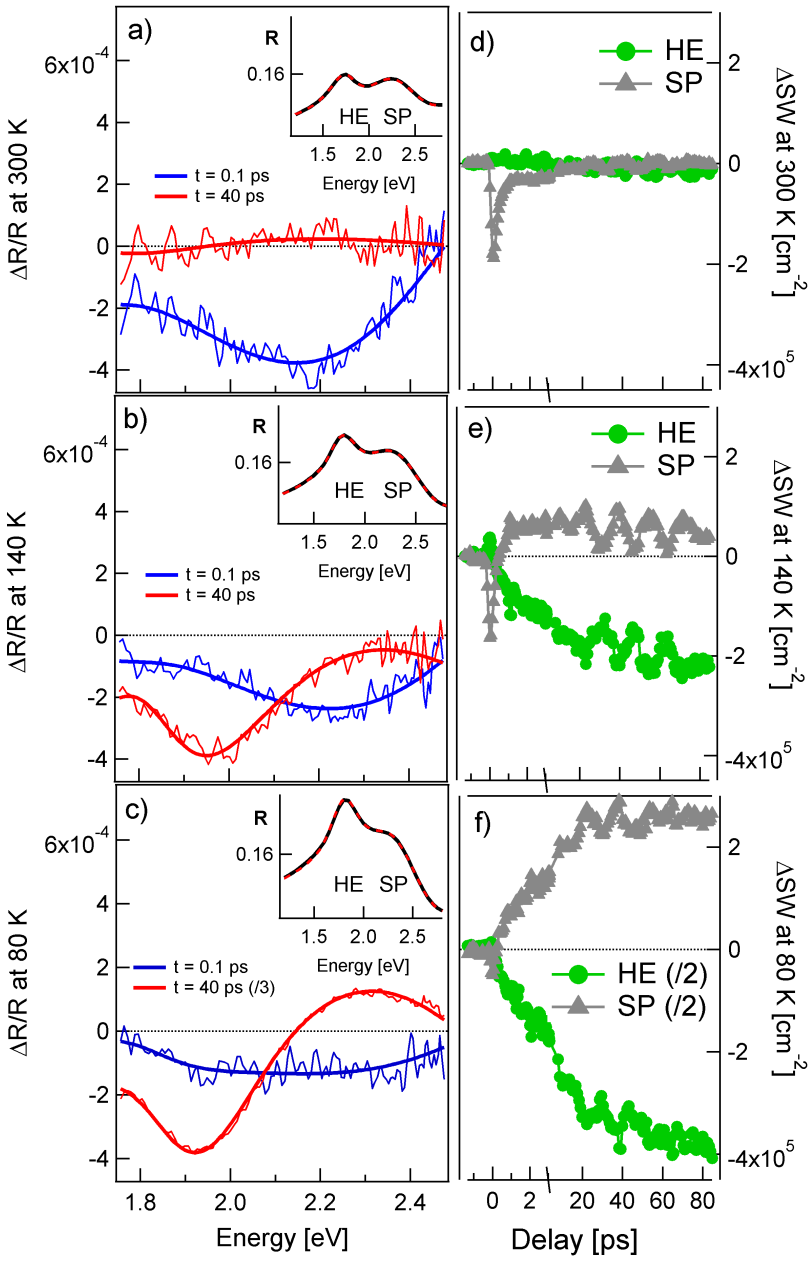

Figure 5.4: From transient reflectivity to spectral weight. The transient reflectance is fitted using a variational approach on the static fit. (a), (b), and (c) depict the transient reflectance for two characteristic times, typical of the "fast" and "slow" dynamics, at 300 K, 140 K, and 80 K, respectively, and the relative variational fit. In the insets the static reflectance for the different phases are reported[47]. (d), (e), and (f) show the time evolution of the SW variations in the different phases (see text).

depletion, confirming that only the higher energy optical transition is of single-particle origin. In fact, if the SP is related to a delocalized excitation and the HE is "more" of localized origin, you expect only the SP to be perturbed "immediately" by pump-excitation. On the other hand the slow response (t > 10 ps), revealed in the orbitally ordered phases, is related to spectral weight changes of both HE and SP bands.

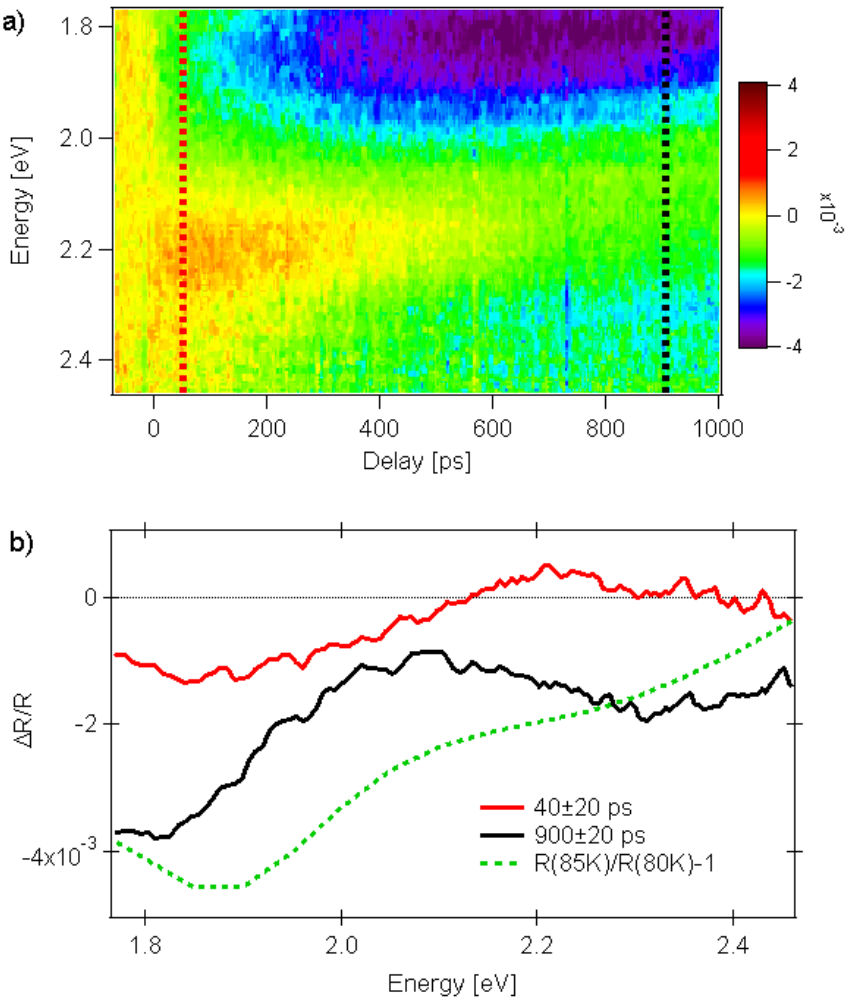

Figure 5.5: Long timescale pump-probe measurement at 80 K. a) Time-domain reflectivity data at 80 K. Note that the fast response visible in Fig.5.2 is absent beacuse of the coarse temporal step used. b) Transient reflectance at t = 40 ps (red curve) and 900 ps (black curve). The expected thermal response $(R^{static}(85\,K) - R^{static}(80\,K))/R^{static}(80\,K)$ is shown for comparison (green curve).

The time-domain response cannot be accounted for by photo-induced heating. The spectral weight of both oscillators increases upon cooling (Fig.5.1) and it is therefore expected that a transient laser-induced heating would result in a decrease of the spectral weight of both SP and HE. However, the time-domain measurements (Fig.5.2) reveal that only the SW of the HE peak

decreases, while the SP band shows the opposite behavior, which rules out a simple heating effect. The non-thermal SW gain of the high-energy oscillator (Fig.5.5) lasts up to ≈ 400 ps and only at longer times the measurements indicate a SW loss for both oscillators. A comparison between green and black curves in Fig.5.5b reveals that 1 ns after photoexcitation the degrees of freedom have not reached the thermal equilibrium.

Following those considerations we analyze the transient spectral weight measured at t > 20 picoseconds (well beyond the electronic relaxation) as resulting from a thermal contribution and a non-thermal one. The thermal contribution to the SW variation of the HE and SP peaks ($SW_{HE}^{static}(T+\Delta T)$ and $SW_{SP}^{static}(T+\Delta T)$) can be calculated by interpolation of the temperature behaviour of the static measurements at $T+\Delta T$, where ΔT is the photo-induced heating obtained from thermodynamic considerations (details in Par.5.5).

The SW variations of non-thermal origin can therefore be calculated subtracting the thermal contribution to the experimental values:

$$\begin{aligned} \Delta SW_{HE}^{non-thermal} &= SW_{HE}^{pumped}(50\,ps) - SW_{HE}^{static}(T+\Delta T) \\ \Delta SW_{SP}^{non-thermal} &= SW_{SP}^{pumped}(50\,ps) - SW_{SP}^{static}(T+\Delta T) \end{aligned} \tag{5.5}$$

for HE and SP respectively, where $SW_i^{pumped}(50\,ps)$ $(i = HE, SP)$ are the means of the measured photo-excited spectral weights at t=50±30 ps after the pump arrival.

The non-thermal components of the pump-driven spectral weight variations at different equilibrium temperatures are reported in Fig.5.6. It is evident that the non-thermal contributions consist of a direct exchange of spectral weight between the HE and SP: this result proves that the two lowest lying optical excitations belong to the same multiplet and that the 1.8 eV transition is of excitonic nature[47]. Moreover, the growth of the photo-induced SW transfer from the HE to the SP in the C-SO phase (Fig.5.6 for T < 116 K) highlighs the kinetic energy contribution to the formation of the HE.

We argue that the spectral weight loss of the HE in favor of the SP is driven by pump-induced spin-disorder (Fig.5.7). Two adjacent and c-oriented orbital chains of YVO_3 in the G-OO/C-SO phase are sketched in the first row of Fig.5.7. The spin order is FM along the c axis ($J_c < 0$) while it is antiferromagnetic in the orthogonal direction ($J_a > 0$). The photo-excitation (a axis polarized) transfers charges between chains, leaving one excess electron on a site and one vacancy on the nearest-neighbor site as depicted in Fig.5.7 (t=0). The magnetic coupling between an excited and a non-excited site along c changes as a consequence of such a charge redistribution (J_c^*). This dramatic perturbation of the spin coupling can be grasped by the following considerations. The Goodenough-Kanamori rules[154], stating that the super-exchange coupling J between half-filled and empty orbitals is negative, are consistent with the FM order observed along the c axis. At simplest, the pump-driven changes in the orbital occupation lead to a switch from FM to AFM exchange coupling. The electronic subsystem relaxes within a few picoseconds (t_1) while

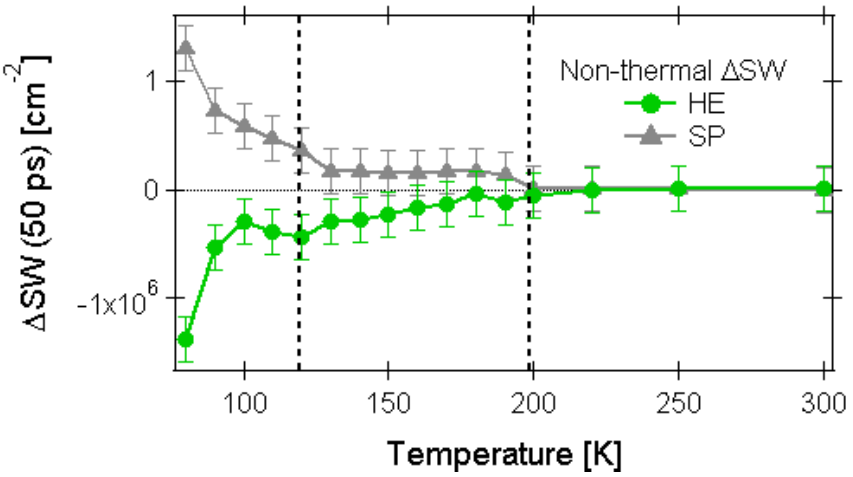

Figure 5.6: Non-thermal spectral weight changes of the HE and SP peaks. The excitonic nature of the low-energy transition is revealed by the direct SW exchange between the two excitations (see text). The error bars are estimated from the fitting procedure.

the spins remain locally perturbed (tilted blue arrows in Fig.5.7 for t=t_1). We argue that, being the orbital angular momentum completely quenched, the coupling mechanism allowing the magnetic subsystem to transfer energy to other degrees of freedom is very weak. Therefore, the local perturbation of the spins diffuses (t_2) leading to spin disorder. This partially suppresses the kinetic energy gain of the HE and leads, subsequently, to a non-thermal spectral weight transfer to the SP peak. A fully thermalized state is achieved only on much longer timescales (> 1 ns) through spin-lattice coupling[152].

In conclusion, here we reveal the nature of the two lowest energy peaks detected in the 1-3 eV optical spectra of the orbitally ordered Mott-insulator YVO_3. This finding was made possible by out-of-equilibrium experiments. The results show how time-domain broadband optical spectroscopies can disentangle the thermal and non-thermal contributions to the optical transients of properly excited states across a Mott-Hubbard gap. In particular, we prove that the total spectral weight is conserved during the de-excitation process, hence revealing that the low-energy feature is a Hubbard exciton, i.e. a resonance or a nearly bound state between a doublon and a holon. This observation, otherwise not conceivable using spectroscopies in the frequency domain, suggests that the optically pump-driven spin-disorder can be used to quantify the kinetic energy gain of the excitons in the ferromagnetic phase.

5.5 Appendix

5.5.1 Time-resolved measurements

We measured the transient reflectivity $\Delta R(t)/R$ as a function of temperature and pump-probe delay in the $1.65-2.75\,eV$ energy-region after excitation with

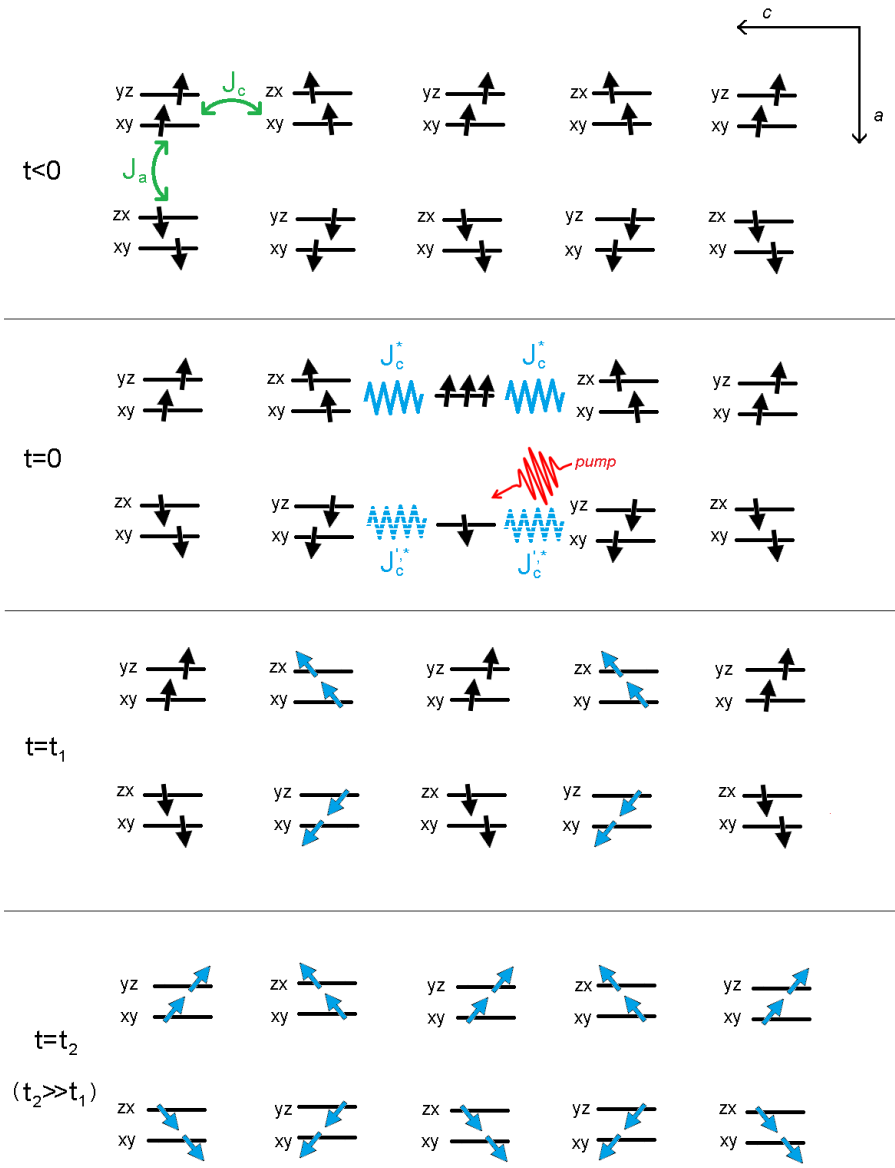

Figure 5.7: Non-thermal spin disorder. YVO_3 is in the G-OO/C-SO phase; t indicates the pump-probe delay (t<0 represents the unperturbed state). The photo-excited holons and doublons perturb locally the magnetic coupling along the FM chain J_c^* ($J_c^{'*}$) (t=0, central site). The photo-excited electrons relax within few picoseconds (t≈t_1) leaving a local perturbation on the spin system. The spin disorder diffuses along the FM chains on a longer timescale (t=t_2) resulting in SW transfer between the HE and SP peaks (see text).

4 mJ/cm^2 of 1.6 eV ultra-short Ti:Sa laser pulses at 40 KHz. The linearity of the response was checked in all phases. Time-domain measurements were performed with the pump parallel to the a-axis (P||a) and probe parallel to c (p||c) up to 1 ns of pump-probe delay. A set of representative measurements is plotted on Fig.5.8. Similar measurements performed with pump parallel to the c-axis (P||c) and probe parallel to the a-axis (p||a) show only a temperature-independent fast decay time (Fig.5.9). Long timescale measurements for P||a and p||c are shown in Fig.5.10.

5.5.2 Time-resolved fitting

We fitted the transient reflectivity in the time and frequency domains by allowing the variation of only 4 parameters out of 21: the optical strength of SP, and the optical strength, width, and central frequency of HE. The most important parameters are the oscillator strength of the SP peak, the oscillator strength and the width of the HE peak. Above 200 K all the transients observed can be described by changing only the strength of the SP peak, while the strength of the HE becomes more and more relevant upon cooling below 200 K. At 80 K, the strength of the SP drops about 1% on the fast timescale ($< 1\,ps$) and increases by about 1% for longer times ($40 - 80\,ps$). The other parameters are necessary to account for the long dynamics below 200 K. The strength and width of HE show a drop lower than 0.5% in the region investigated, while the cental frequency is virtually unchanged at all temperatures ($< 0.02\%$). From the full set of time-dependent parameters obtanied we calculated the spectral weight of each band separately by numerical integration in the $0 - 2.85\,eV$ ($0 - 23000\,cm^{-1}$) range, as described earlier.

It should be noted that the central frequency of the HE for the static data shifts of a few % by changing temperature. This confirms that even though structural distortions may be of relevance in determining the ratio between the SW of HE and SP at equilibrium they are not the main player in the dynamical response.

Non-thermal contribution

At any fixed temperature T, the non-thermal contribution to the variations of the SW of HE and SP can be calculated from static optical properties, the time-resolved data and the laser pump energy, as follows:

$$\Delta SW^{non-thermal}(t) = SW^{pumped}(t) - SW^{static}(T + \Delta T(t)), \qquad (5.6)$$

where $SW^{pumped}(t)$ is the photo-excited SW and $SW^{static}(T + \Delta T(t))$ is obtained by interpolation at $T + \Delta T(t)$ of the static model. $\Delta T(t)$ is the pump-induced heating calculated from a two-temperature model (2TM)[6, 9] for the

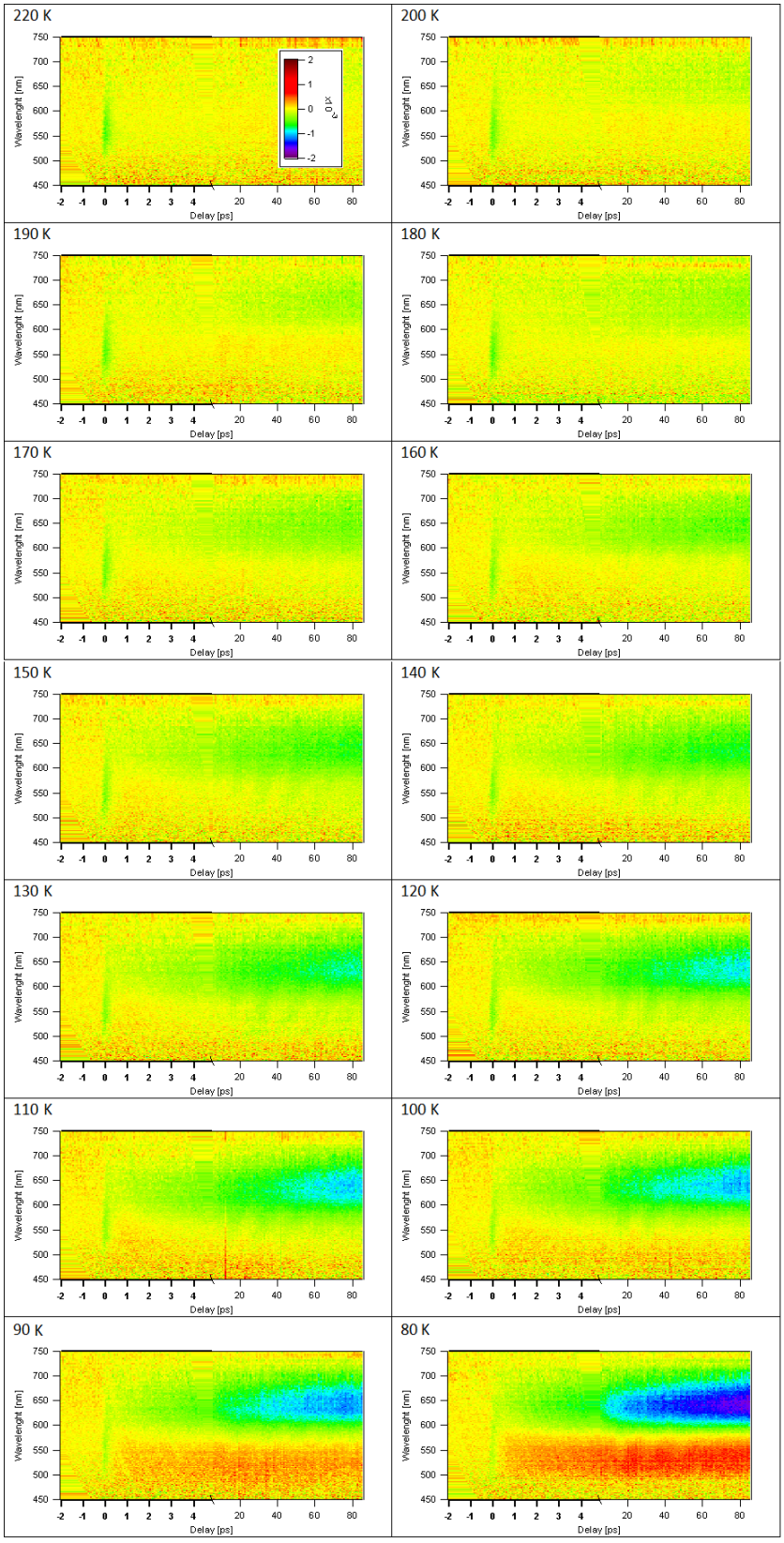

Figure 5.8: Relative variation of the reflectivity in the -2 to 80 ps range, with P||a and p||c.

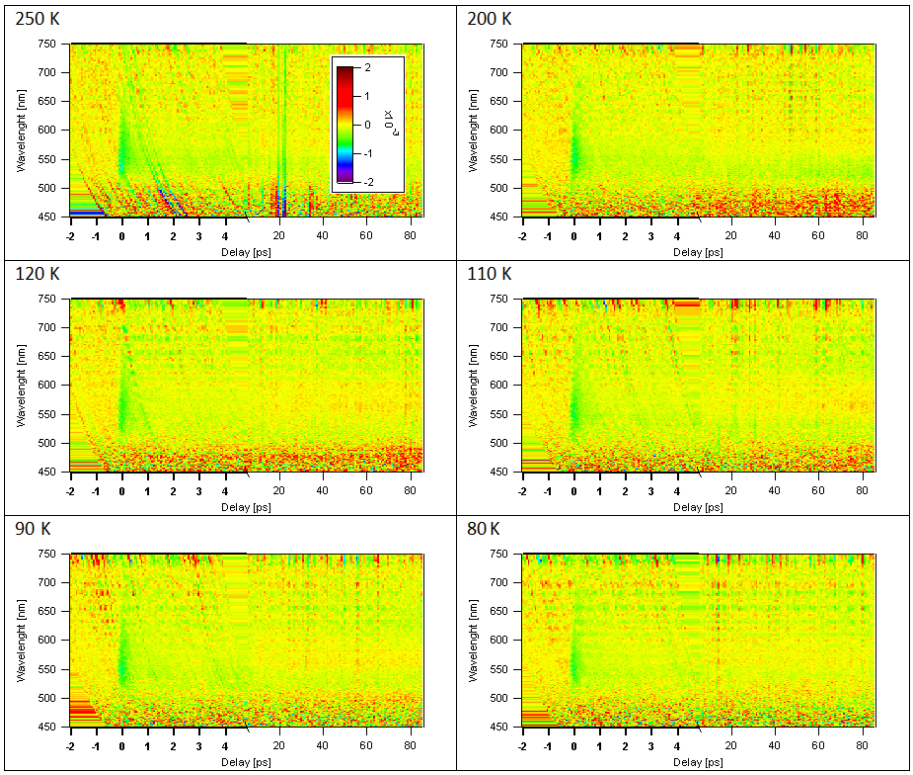

Figure 5.9: Measurements with P||c and p||a.

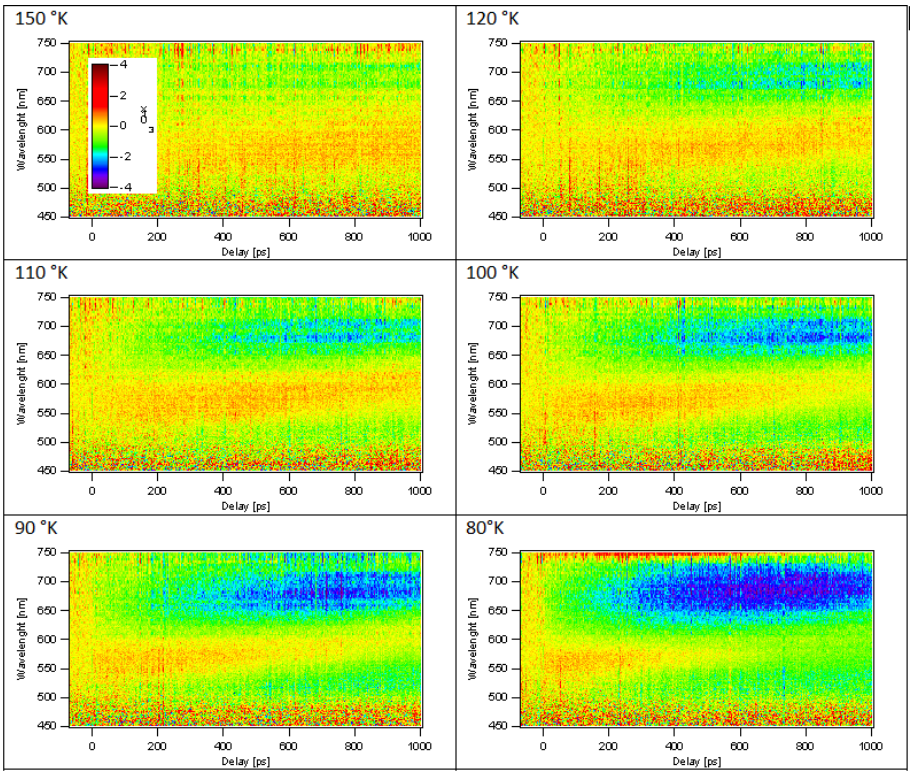

Figure 5.10: Relative variation of the reflectivity in the -40 to 1000 ps range, with P||a and p||c.

lattice (L) and spin (S) degrees of freedom:

$$\begin{aligned} C_L \frac{dT_L}{dt} &= -\gamma(T_L - T_S) + \rho P_{eff}(t) \\ C_S \frac{dT_S}{dt} &= -\gamma(T_S - T_L) + (1-\rho) P_{eff}(t) \end{aligned} \tag{5.7}$$

where C_L and C_S are the heat capacities[134] of the two subsystems, $\gamma = 10^{-5} W/(K \cdot mol)$ and $\rho = 0.93$ are phenomelogical constants describing, respectively, the magnetoelastic coupling[155] and the coupling of the electronic subsystem to the other two. In this model we assume that the pump pulse $P(t)$ photo-excites carriers from the lower Hubbard band (LHB) to the upper Hubbard band (UHB). As the quasi-particles relax, they act as an effective pump $P_{eff}(t)$ for the lattice and spin degrees. The behaviour of T_L and T_S is reported in Fig.5.11 for T=80 K.

The validity of this model is confirmed by comparison, at any temperature, with the expected thermodynamic steady-state temperature increase $\widetilde{\Delta T(T)}$. It is straightforward to write

$$\widetilde{\Delta T(T)} = \frac{Q_{abs} \cdot N_A \cdot V}{S \cdot d \cdot u \cdot C_{mol}} \approx \frac{150}{C_{mol}[J/(mol \cdot K)]}, \tag{5.8}$$

where Q_{abs} is the pump energy absorbed by the sample, N_A the Avogadro's number, V the elementary cell volume, S the sample surface irradiated, d the pump penetration depth, u the number of chemical units in a cell and C_{mol}[134] the temperature-dependent total heat capacity. There is a good agreement between the temperature increase for the two models, as shown in Fig.5.12 (red and black curves). At this point, the 2TM permits to obtain the temporal dependence of the lattice temperature and allows for the calculation of the non-thermal component. The blue dots in Fig.5.12 represent the temperature variations at pump-probe delay $t = 50\,ps$ used to obtain the non-thermal contribution to the variation of the spectral weight (Fig.5.7).

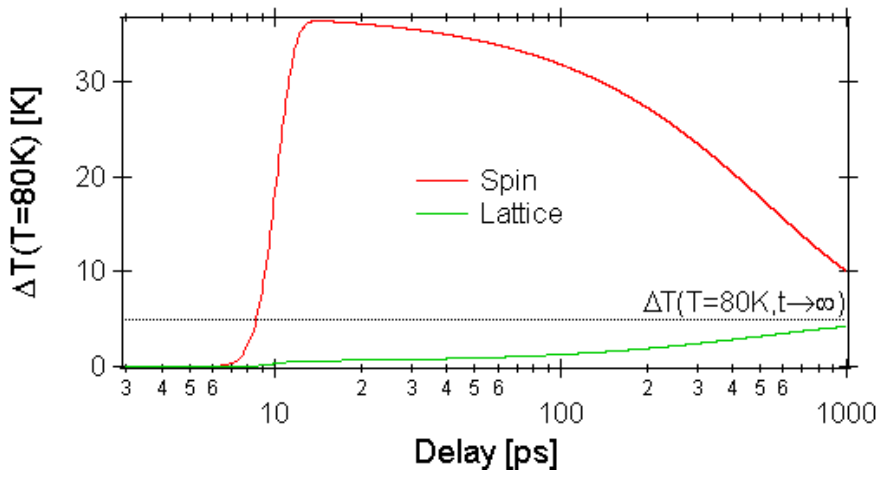

Figure 5.11: Two temperature model for T=80 K. A gaussian $P_{eff}(t)$ with $FWHM = 3\,ps$ is turned on at $t = 10\,ps$. $T_S(t)$ is reported in red, $T_L(t)$ in green while the converging straight line $\Delta T(80\,K, t \to \infty)$ is dotted.

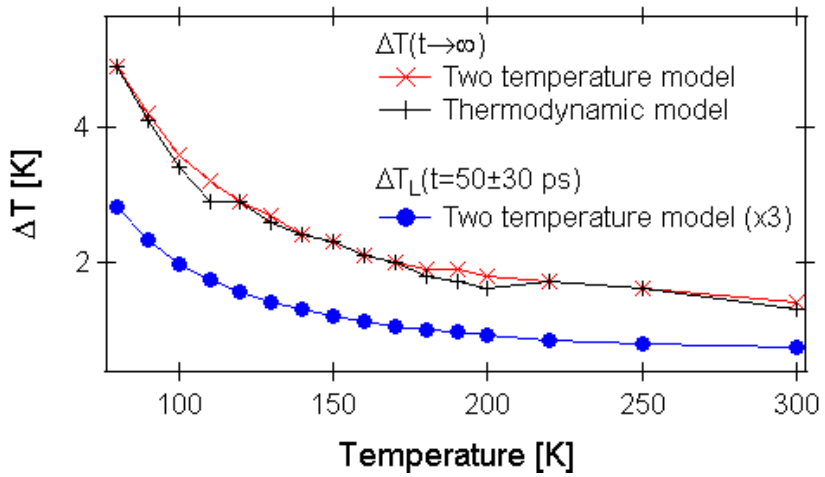

Figure 5.12: Comparison of the two thermodynamic models at equilibrium or long pump-probe delay. The blue dots represent the calculated lattice temperature used to calculate the non-thermal contribution to the SW variations at different temperatures.

Chapter 6

Non-thermal CT dynamics in La_2CuO_4 after ultra-fast selective excitation

Here we present and discuss ultra-short pump and broadband probe measurements on La_2CuO_4 and show that, by tuning the pump wavelength in the visible range (at $1300\,nm$ and at $400\,nm$) across the energy of the charge-transfer (CT) gap of $2\,eV$, dramatic effects on the transient optical response of the CT gap can be observed, even when the detected relative variation of the reflectivity is in the linear regime. The anomalous time domain "hardening" of the CT gap can be rationalized introducing a new selective excitation mechanism at optical frequencies, where the electronic charge is redistributed between the $La-O$ and the $Cu-O$ planes.

6.1 Introduction

The exotic properties of transition metal oxides (TMOs) are the result of the complex interactions between the intertwined fundamental electronic, vibrational, and magnetic degrees of freedom. The strong electron-electron correlation together with the interplay between electronic and the other degrees of freedom is at the origin of the onset of collective electronic phases in TMOs. Among those, the most interesting phenomena is the high T_C superconductivity in the family of the cuprates. In spite of the great effort devoted to the problem, after 26 years of studies a comprehensive theory is still missing.

The cuprates have been extensively studied with several techniques[8]. Fig.2.1 displays the phase-diagram upon doping. The physics of these systems is well understood at both very low and very high doping. At zero doping, the so-called parent compound is a Mott insulator of charge-transfer that orders AFM below a certain temperature. At high doping a Fermi-liquid metallic phase is present above T_C, and a BCS-like superconductor appears

below T_C. However, the underdoped region is poorly understood: a non-BCS SC phase at low temperatures, a strange metallic phase at high temperatures, and a peculiar "pseudogap phase" for intermediate temperatures are present ($T_C < T < T^*$)[7].

The unconventional nature of the superconducting phase in the family of the cuprates is shown by the anomalous behavior of the optical properties at the onset of superconductivity. In BCS systems the spectral weight (SW)[1] is redistributed upon entering the superconducting (SC) phase: a Dirac's delta at zero frequency appears in the real part of the optical conductivity. Such delta depletes SW from the FIR region of the spectrum extending up to 2Δ, with Δ SC gap value[8] of few meV. In other words, a BCS superconductor follows the Tinkham-Ferrell-Gloverm sum rule[8]. This is not the case for the cuprates: upon entering the SC phase the SW in the cuprates is depleted up to few eV, i.e. up to the optical range, and the Tinkham-Ferrell-Gloverm sum rule is violated. Hence, the optical response of HTSC in the visible range has been extensively studied as a direct tool to probe the superconducting phase, also in pump-probe measurements[156].

In the time-resolved experiments on the cuprates, an excess of photo-carriers is suddenly injected by the pump pulses and (partially) melts the SC gap[16–18, 26]. The transient optical response of the cuprates in the visible range can be rationalized if significant perturbations of the charge-transfer transitions occur[26]. In these studies, however, the effect of the pump is often considered as a simple ultra-fast heating of the electronic degree of freedom[16–18, 26]. Here we study the effect of the energy content of the pump pulses on the optical transient. We demonstrate that the interpretation of free-electron-heating might be oversimplified by studying the CT dynamics free from the response of the condensate.

We performed time-resolved reflectivity measurements on the parent compound of the cuprates La_2CuO_4. We measured the photo-induced dynamics of the CT transition comparing excitation with photon energy lower and higher than the CT edge revealing that different photon energy can stimulate different dynamics. By tuning the pump energy, we demonstrate the possibility of selectively-exciting orbital transitions leading to an effective transfer of charges from out-of-plane to in-plane orbitals. This orbital excitation leads, on timescales faster than the thermalization ones ($100\,fs$), to a non-thermal hardening of the CT transition possibly related to the ultra-fast formation of polaronic states.

La_2CuO_4 is a Mott insulator which undergoes a phase transition from tetragonal to orthorhombic structure at $530\,K$ upon cooling[158] (Fig.6.1a), and exhibits an AFM ordering at $T_{N\acute{e}el} = 325\,K$[158]. The copper ions have coordination 2+, hence there are nine electrons in the outer $3d$ shell. The d levels are split by the oxygen octahedral environment and the single hole occupies the

[1]The SW is related to the number of quasi-particles associated to an optical transition. For the definition see Par.3.1.3

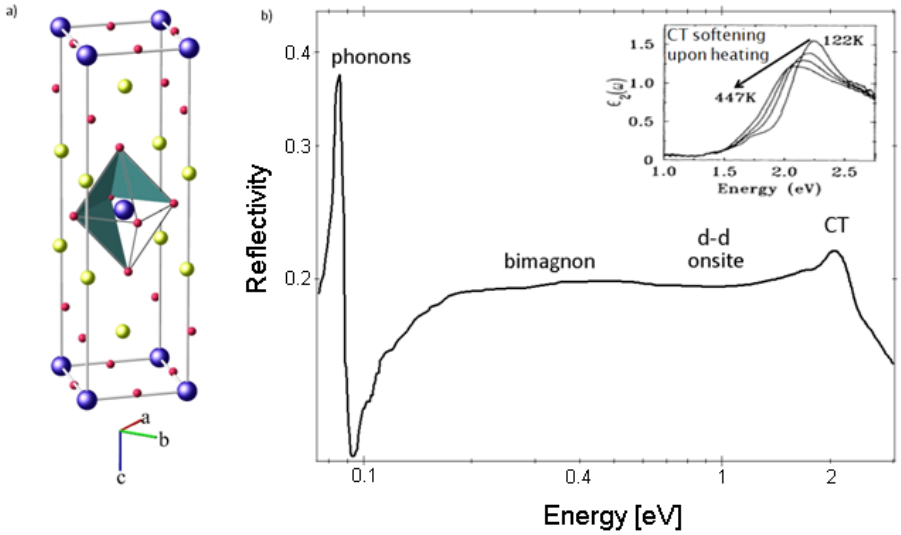

Figure 6.1: a) Orthorhombic phase of La_2CuO_4 at $325\,K$ obtained from neutron scattering measurements[157]. The oxygen octahedron surrounding each copper ion is slightly elongated along the c axis. b) Reflectivity of La_2CuO_4 measured with polarization parallel to the $Cu-O$ $(a-b)$ planes obtained by matching published data[48, 54]. Insert: temperature evolution of the CT peak as reported by Falck et al.[48].

e_g level with higher electronic energy. As the octahedra are slightly elongated along the c axis, the hole belongs to the $3d_{x^2-y^2}$ orbital (Fig.6.1a)[159–161].

In Fig.6.1b the in-plane optical reflectivity of La_2CuO_4 is reported up to $3\,eV$: in this spectral region the optical response is dominated by excitations in the $Cu-O$ plane[54]. Apart from the phonons at low energies[54], features are evident from $0.4\,eV$ to $1.2\,eV$, around $1.5\,eV$, $1.7\,eV$ and at $2\,eV$. The transition at $0.4\,eV$ has been attributed to the absorption of two magnons and one phonon[159, 160, 162]: this is the so called bimagnon state. The broad structure in the $0.4\,eV$ $-$ $1.2\,eV$ range has been attributed to magnon and phonon sidebands of both the bimagnon and the onsite $d-d$ excitation of the hole from the $d_{x^2-y^2}$ orbital to the $d_{3z^2-r^2}$ orbital[161]. Character of onsite $d-d$ excitation is also attributed to the optical transition at $1.5\,eV$[161], while the shoulder at $1.7\,eV$ has been rationalized as an excitonic state[48]. The energy gap in the plane is of charge-transfer origin between the occupied $O\,2p$ states and the half filled $Cu\,3d_{x^2-y^2}$ orbitals[163]. The noticeable shift of the CT transition energy upon cooling is attributed to polaronic effects[48, 164, 165], while the hardening with hole doping by Sr substitution can be interpreted as an effective decrease of the external pressure due to the bigger radius of the Sr^{2+} ion respect to La^{3+}[158, 163].

6.2 Methods

In order to address the effect of the pump wavelength on the transient response of La_2CuO_4 we performed time-resolved experiments with broadband probe

pulses and ultra-short pumps with energies of $0.95\,eV$ and $3\,eV$. The duration of both pump pulses was measured by autocorrelation and found to be smaller than $100\,fs$ for both wavelengths. Freshly polished $a-b$ oriented samples were mounted on the cold finger of a helium-flow cryostat. The reflectivity changes $\Delta R(\omega,t) = \frac{R(\omega,t)-R(\omega)}{R(\omega)}$, with $R(\omega,t)$ time dependent perturbed reflectivity and $R(\omega)$ static reflectivity, were measured in the $1.6-2.7\,eV$ range at $250\,KHz$ of repetition rate and temperatures ranging from $330\,K$ to $50\,K$. The pump fluence is equal to $326\,\mu J/cm^2$ and $169\,\mu J/cm^2$ for the $3\,eV$ and $0.95\,eV$ pumps, respectively. The amplitude of the photo-induced variation of the reflectivity is linear with the pump fluence up to twice the values reported above.

The measurements at $130\,K$ are reported in Fig.6.2. The $3\,eV$ pump leads to negative changes of the reflectivity in the wavelength region across the CT edge ($1.8-2.4\,eV$). The dotted curve in Fig.6.2c reports the time-dependent reflectivity at $2.1\,eV$ probe energy for $3\,eV$ pump pulses: a negative transient is detected at zero pump-probe delay with a rise time of about $300\,fs$. On the other hand, the wavelength dependence of the transient reflectivity for $3\,eV$ excitation does not show a significant evolution as a function of pump-probe delay (Fig.6.2b). It is evident that the reflectivity variation in the first few hundreds of femtoseconds is completely different for the two pump energies (Fig.6.2d): the transient response is delayed of about $300\,fs$ in the $3\,eV$ pump data, while it is "instantaneous" (i.e. below the temporal resolution) for $0.95\,eV$ pumping (Fig.6.2c). At longer pump-probe delays ($t > 300\,fs$) the transient responses following above and below gap pumping are identical within the experimental error (see Par.6.5).

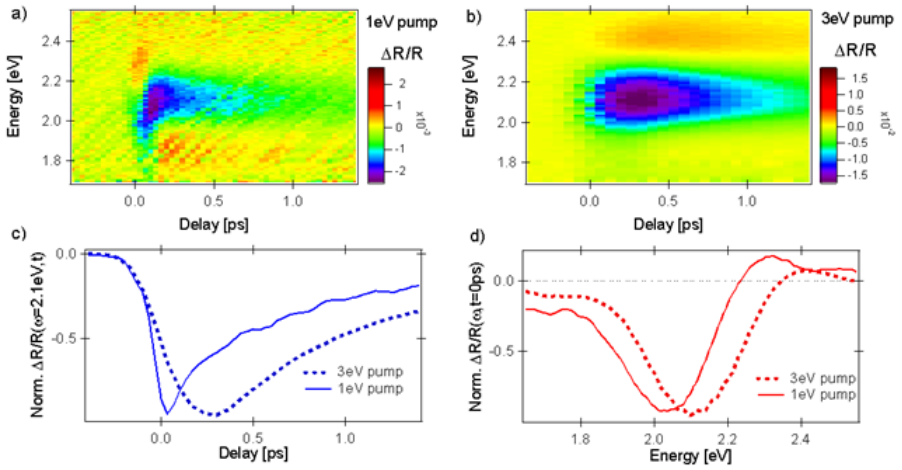

Figure 6.2: Pump-probe measurements performed at $130\,K$ with pump energy equal to $0.95\,eV$ (a) and $3\,eV$ (b). c) Comparison of the $\Delta R/R$ temporal dispersions at $\omega = 2.1\,eV$ for the two pump energies. d) Transient reflectivity at the temporal coincidence of pump and probe pulses for $3\,eV$ pump (dotted red) and $0.95\,eV$ (solid red).

In order to extract important physical quantities out of time-resolved measurements, such as the time evolution of the spectral weight, it is possible to adopt a differential fit approach based on a Lorentz-like model[166]. Here,

on the contrary, we develop a novel methodology of data analysis that has the advantage of being model independent. Our analysis, founded on the Kramers-Kronig relations that links the real and imaginary parts of the optical constants by the causal relationship, proceed as follow. The procedure requires the knowledge of the static reflectivity $R(\omega)$ over a broad energy range, from a few meV up to several tens of eV. In the case of La_2CuO_4 the reflectivity measurements used are obtained by matching published reflectivity data on the different energy ranges[48, 54, 167]. Once $R(\omega)$ is known we can readily calculate the real and imaginary part of the static dielectric constant. At first, the phase $\rho(\omega)$ of the complex reflectance $\widetilde{R(\omega)} = R(\omega)e^{i\rho(\omega)}$ is calculated from the reflectivity $R(\omega)$ through the proper Kramers-Kronig relation[40]. Once $\rho(\omega)$ is obtained, the real and imaginary parts of the dielectric constant, $e_1(\omega)$ and $e_2(\omega)$, follow from eq.3.17.

The time-resolved $\Delta R(\omega, t)$, on the other hand, is measured over a limited energy range. Nevertheless, for small variations of the reflectivity as the ones detected in our pump-probe experiments (up to 10^{-2} as shown in Fig.6.2), we can assume that the Kramers-Kronig are local relations. In other words, we presume that the relative variation of the reflectivity is negligible outside the probed energy range. Starting from this assumption it is possible to calculate the pump-perturbed optical constants $e_1(\omega, t)$ and $e_2(\omega, t)$ from the time-dependent $R(\omega, t)$, in turn calculated from the static $R(\omega)$ and the measured $\Delta R(\omega, t)$.

The results of this analysis performed on the $130\,K$ data are reported in Fig.6.3, where the photo-induced variation of the real part of the optical conductivity, $\Delta s_1(\omega, t) = s_1(\omega, t) - s_1(\omega)$, is shown.

6.3 Results

In Fig.6.3a the photo-induced variation of $s_1(\omega, t)$ with $0.95\,eV$ pump at $130\,K$ is reported. In the first few hundreds of femtoseconds we notice striking differences with respect to the time-resolved data with pump energy exceeding the CT gap (Fig.6.3b).

In Fig.6.3c the transient optical conductivity for probe energy close to the value of the CT gap ($2.1\,eV$) measured with pumps at $3\,eV$ (dotted blue) and $0.95\,eV$ (solid blue) at $T = 130\,K$ is shown. The optical response of the system at the CT edge following excitation with $3\,eV$ pump pulses is delayed from the arrival of the pump. On the contrary, a smooth rise time of about $300\,fs$ has been detected. This is consistent with previous works on either La_2CuO_4[168, 169], $YBa_2Cu_3O_y$ and Nd_2CuO_4[170], and $BSSCO$[17]. We stress that in both Okamoto's[168, 169] and Matsuda's[170] works the pump energy is higher than the value of the CT gap at equilibrium: this suggests that the CT edge is not directly coupled to the transient population of free quasi-particles. The slow $\approx 300\,fs$ rise time can be rationalized as an electron-phonon relaxation process[17]. The solid blue curve in Fig.6.3c reports $s_1(\omega = 2.1\,eV, t)$ for

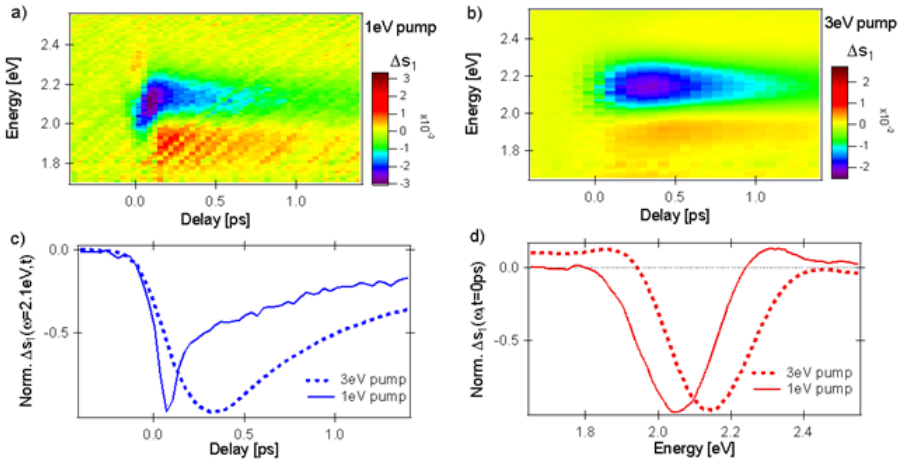

Figure 6.3: Variation of s_1 (colours) as a function of probed energy and pump-probe delay. a) For pump pulses of energy $0.95\,eV$. b) For $3\,eV$ pump pulses. c) The transient optical conductivity for probe energy at $2.1\,eV$ for both pump energies (dotted $3\,eV$, solid $0.95\,eV$). d) The variation of the optical conductivity $\Delta s_1(\omega, t = 0ps)$ at zero pump-probe delay is shown.

$0.95\,eV$ pump pulses: the response at the CT edge is "instantaneous" after below gap excitation.

In 1992 Falck et al.[48] developed a model to describe the static dependence of the CT edge as a function of temperature that includes polaronic effects, i.e. a strong coupling of the electronic charges with the phonons. Our results push this interpretation to its limits: the photo-injected excess free quasi-particles are not as strongly coupled as the low-lying excitations to the CT transition, i.e. it is much more direct to manipulate the optical response at $2\,eV$ by $1\,eV$ excitations than by $3\,eV$ excitations. It's like saying that my cat could move the closet in my bedroom much faster than me.

The energy dispersions at two fixed pump-probe delays are reported in Fig.6.3d for both pump energies ($3\,eV$, dotted red, $0.95\,eV$, solid red). For $3\,eV$ pumping, $\Delta s_1(\omega, t)$ is positive at lower energies and negative at higher ones, and crosses zero at about $2\,eV$ (close to the value of the unperturbed CT gap). We argue that this zero-crossing behaviour can be attributed to pump-induced heating. In fact in static measurements the position of the CT edge softens on increasing the temperature, as sketched in the insert of Fig.6.1. Hence, if the pump effect consists only in heating the sample, one would expect a positive response at lower energies and a negative response at higher ones. Secondly, this positive to negative response upon increasing the probed energy has been already rationalized as a thermal effect[168–172]. Gin et al.[172] measured the steady-state variation of the transmission $\Delta T/T$, that is proportional to the opposite of the absorption for small ΔT[171], at $15\,K$ after photo-irradiation with a continuous laser source with energy above the CT gap ($2.54\,eV$, $0.8\,W/cm^2$). Okamoto et al.[168, 169] detected a similar feature in room temperature time-domain experiments with $200\,fs$ and $2.25\,eV$ pump

pulses with a repetition rate of $1\,KHz$. By comparison with the expected thermal response of the optical density, they assign the positive-to-negative response to pump-induced heating.

The solid red curve in Fig.6.4d shows the energy dispersion of Δs_1 in the $0 - 0.1\,ps$ range after $0.95\,eV$ pumping: the positive-to-negative trend upon increasing of the probe energy is actually reversed. This suggests an ultra-fast photo-induced hardening of the gap, opposed to the softening expected from thermodynamic considerations. In this sense, it's as if the below-gap pumping induces an ultra-fast cooling of the CT edge.

6.4 Discussion

We know from the literature that the CT edge is softened not only upon heating[48] but also upon increasing the external pressure applied on the $Cu - O$ planes[163]. The pressure effect in La_2CuO_4 is the opposite of what is predicted for simple semiconductors, where the increase of the Madelung potential enlarges the value of the gap.

The mechanism proposed to explain this anomalous pressure dependence of the CT peak in La_2CuO_4 is the following. In La_2CuO_4, the compression of the $a - b$ planes can effectively increase the hopping of the atomic orbitals ($Cu\,3d_{x^2-y^2}$ and $O\,2p$) involved in the CT transition, leading to an effective decrease of the gap. The results of Tokura et al.[163] are fairly consistent with the observed hardening of the (residual) CT edge in La_2CuO_4 upon slight doping by substituting La^{3+} with Sr^{2+}[54, 173]. The radius of Sr^{2+} is larger than the one of La^{3+} bringing, naively, an expansion of the lattice that would be the result of an "applied negative pressure": the hopping of the Cu and O orbitals is decreased and the gap hardens. Here we speculate that the photo-excitation at $0.95\,eV$ acts as an effective negative pressure, responsible for the gap hardening in the first few hundreds of femtoseconds (Fig.6.3).

As already mentioned, Cu is $3d^9$ and at equilibrium the hole occupies the $3d_{x^2-y^2}$ orbital (Fig.6.4a). We recall that the absorption in the $0.4 - 1.2\,eV$ range (Fig.6.1b) has been attributed to magnon and phonon sidebands of the lowest lying excitonic excitation of onsite dd character[161]. In this picture, when the system is perturbed by $0.95\,eV$ pump pulses, few holes are excited from the $3d_{x^2-y^2}$ to the $3d_{3z^2-r^2}$ orbital, leaving an excess of negative charge in the $a - b$ plane (Fig.6.4b). We speculate that the excess of negative charge is the source of the observed ultrafast hardening of the CT gap. In a simplified model, if the $0.95\,eV$ pump "fills" the $3d_{x^2-y^2}$ orbital, the CT from the $O\,2p$ must have a different final state. This can be identified as the $3d_{3z^2-r^2}$, that is half-filled after the ultra-fast excitation. The $2p - 3d_{3z^2-r^2}$ hopping integral is expected to be smaller, inducing a hardening of the CT edge. In other words when a small fraction of electronic charge is instantaneously injected in the $a - b$ plane, the $O\,2p - Cu\,3d_{x^2-y^2}$ hopping is decreased from $\mathbf{t}$ to t, inducing a blue shift of the CT edge (Fig.6.4b).

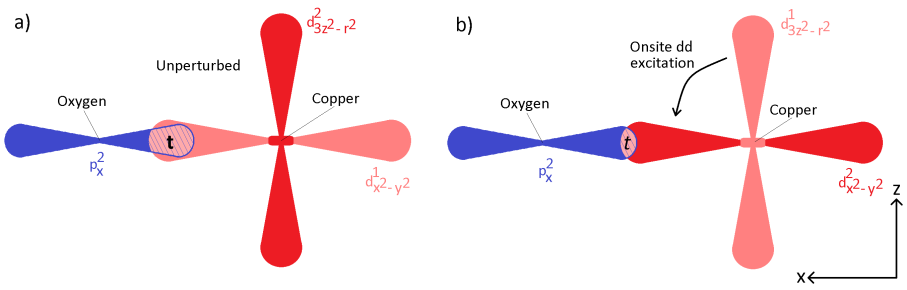

Figure 6.4: Sketch of the proposed mechanism of the CT hardening after photo-irradiation at $0.95\,eV$. a) Unperturbed orbitals of copper and oxygen in the xz plane. b) After onsite excitation, where $\mathbf{t}$ is the hopping parameter.

In conclusion, we performed ultra-fast reflectivity measurements on the parent compound La_2CuO_4 with time resolution of $80\,fs$ by combining broad-band optical probes in the visible range with pump pulses at different energies ($0.95\,eV$, $3\,eV$). We develop a novel methodology of data analysis, founded on the Kramers-Kronig relations (see Par.6.2), that allows to obtain a model-free temporal evolution of all the optical properties over the probed range.

The main result of our study is that the transient optical properties of La_2CuO_4 are dramatically modified upon tuning the pump energy from above to below the value of the CT gap. This result demonstrates that in pump-probe experiments on the cuprate family the pump effects cannot be always treated simply as heating of the electronic degree of freedom. This evidence calls for a revision of the multiple temperatures thermodynamic models in these systems. Our findings indicate that pumping with $3\,eV$ pulses results in a dynamic of the CT edge characterized by a $300\,fs$ rise time that is consistent with previous works[17, 168, 168–170]. Our broadband measurements of the CT transition confirm that the overall transient response in this excitation conditions can be qualitatively interpreted as simple photo-induced heating[169, 171, 172]. On the other hand, the photo-excitation with $0.95\,eV$ ultra-short pump pulses leads to a strikingly different ultra-fast dynamics. First of all, the CT edge is instantaneously perturbed by such below-gap excitations and no slow rise time is observed, indicating a strong coupling between the CT transition and the low energy excitations. More interestingly, the transient response observed in the first $300\,fs$ consists of an ultra-fast hardening of the CT gap as if the sample would be instantaneously "cooled" by the ultra-short laser pump pulses. We propose that this effect could be explained in term of selective dd local excitation which transfers electrons between different Cu orbitals. The observed non-thermal dynamic of the CT in our model is the result of a sudden injection of excess negative charges in the $Cu-O$ planes.

6.5 Appendix

The transient reflectivity data collected for both pumps and several temperatures are reported in Fig.6.5. It is evident that the overall dynamical response is similar within the $3\,eV$ pump measurements (Fig.6.5a,c,e) and $0.95\,eV$ (Fig.6.5b,d,f). Fig.6.6 shows selected energy dispersions of $\Delta R/R$ at 0 and $2\,ps$ pump-probe delays, that are normalized for the sake of comparison. The $3\,eV$ pump data are shown in blue, the $0.95\,eV$ pump data in red. Fig.6.6a,c,e compares the zero delay transients: qualitatively, the response after below-gap pumping peaks at lower energies than the response for above-gap pumping. On the other hand, the transient response for $3\,eV$ pump pulses does not show any significant time evolution, apart from a decaying intensity. At $t = 2\,ps$ the $0.95\,eV$ pump data are consistent with the $3\,eV$ ones, suggesting that the thermal contribution dominates at longer times.

Fig.6.7 displays the shift of the CT edge, at several temperatures, as a function of pump-probe delay after $0.95\,eV$ pumping. No trivial trend of such shift is observed vs. temperature but, qualitatively, the CT edge hardens by a smaller quantity at higher temperatures. The non-thermal response of the CT gap is lost within $100\,fs$ of the pump arrival, at all temperatures. This suggests a fast relaxation mechanism possibly of electronic origin[158].

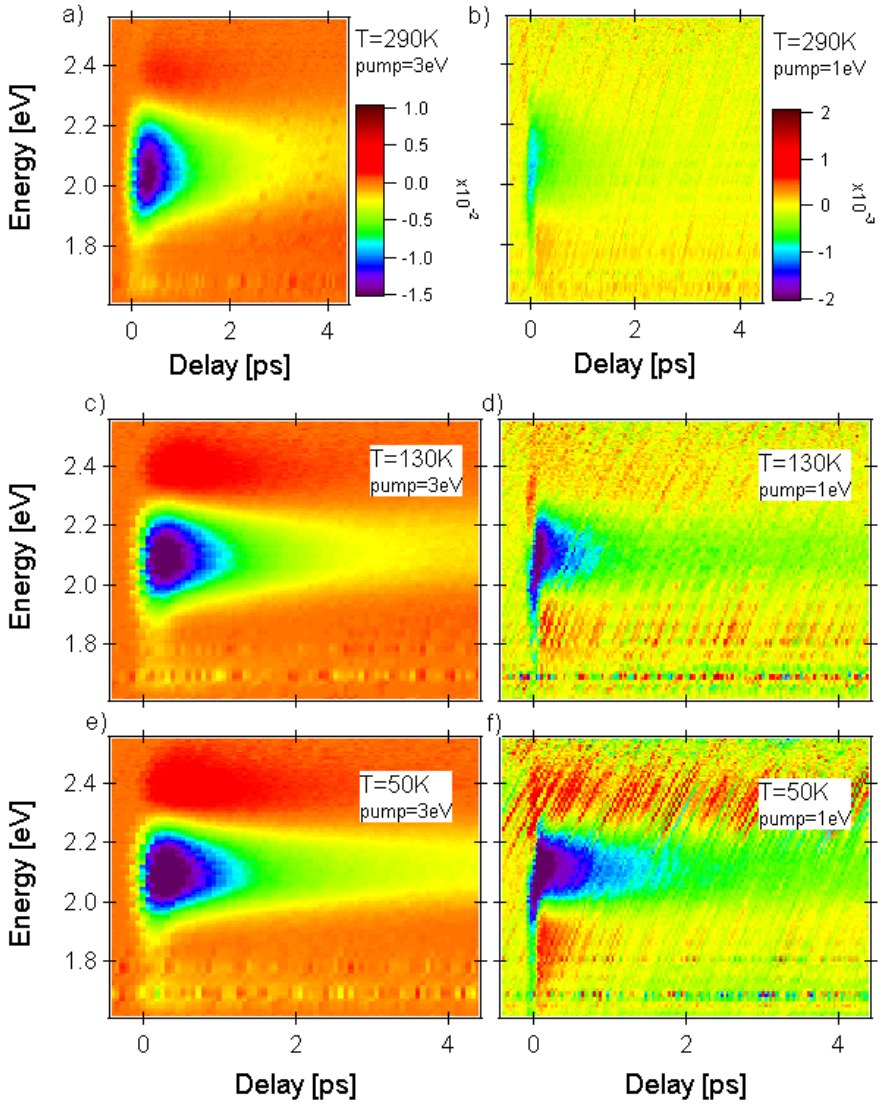

Figure 6.5: Relative variation of the reflectivity (colours) measured by pump-probe spectroscopy at various temperatures ($290\,K$, $130\,K$, and $50\,K$) and for two different pumps energies. a), c), e) for $3\,eV$ and b), d), and f) for $0.95\,eV$. Each graph shares the same Energy and Delay axes. The $3\,eV$ pump data share also the same colour plot (a), c), and e)), as well as the $0.95\,eV$ measurements (b), d), and f)).

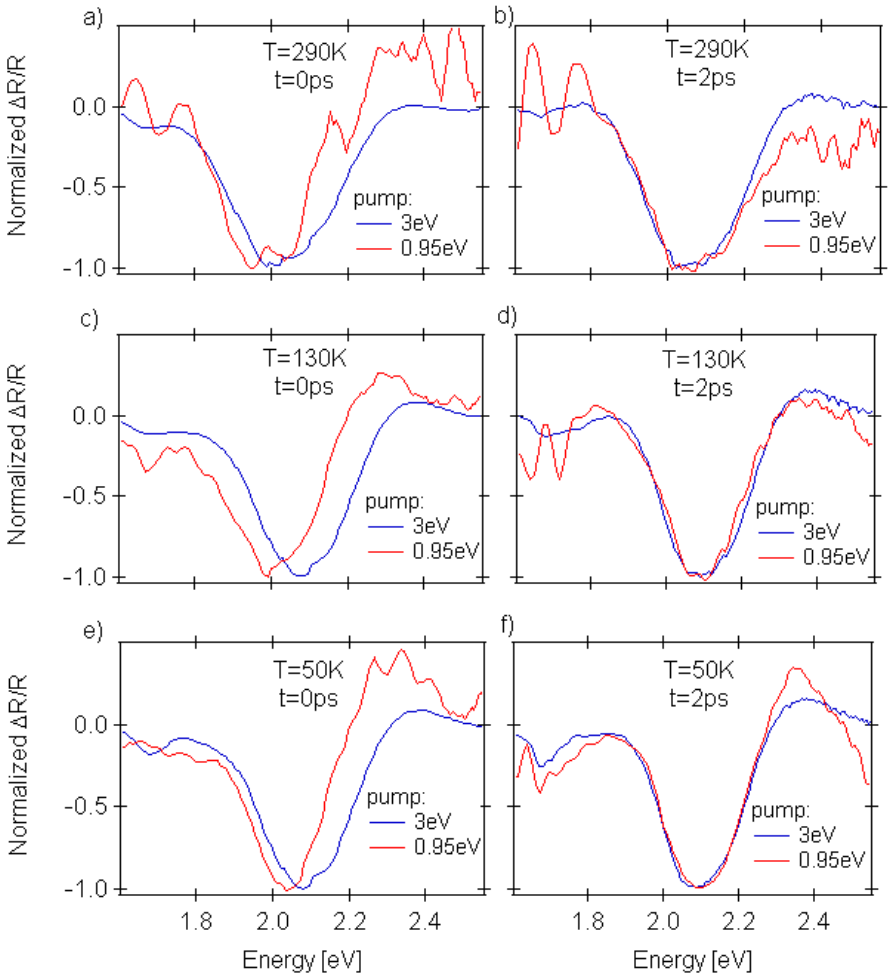

Figure 6.6: Selected energy dispersions of the transient reflectivity data in Fig.6.6. Temperatures (T) and pump-probe delays (t) are shown. In red the $0.95\,eV$ pump measurements, in blue the $3\,eV$ ones.

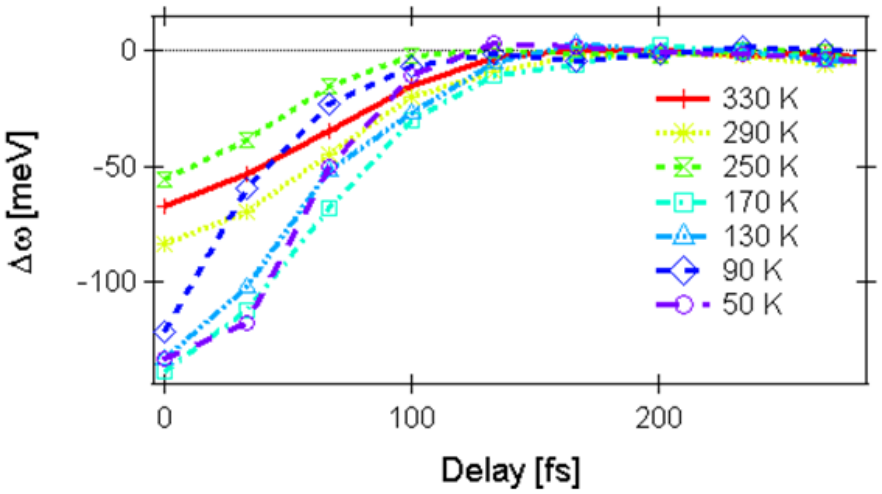

Figure 6.7: Energy shift as a function of pump-probe delay, for $0.95\,eV$ pump pulses and various temperatures. $\Delta\omega$ is calculated as the probe energy at which the transient has a minimum at time t, $\omega(\Delta R^{max}(t))$, minus the probe energy at which the transient reflectivity has a minimum at longer times, $\omega(\Delta R^{max}(t \to \infty))$.

Chapter 7

Coherent phonons in superconducting $YBa_2Cu_3O_{7-\delta}$

The role played by phonons and electronic excitations on the eV energy scale for the formation of the superconducting phase in the cuprates is still controversial. In fact the phonon mediated pairing cannot solely account for the high critical temperatures observed in the cuprates, although strong anomalies are visible in the phonon subsystem upon entering the superconducting phase. Here we study the interplay between phonon modes and high energy electronic transitions by means of time resolved broadband spectroscopy. For the first time our technique allows a direct comparison between electronic transitions and the excitation of coherent phonon modes in the material. This chapter begins with a brief introduction, followed by the results and the methods.

7.1 Introduction

The onset of superconductivity in optimally doped $YBa_2Cu_3O_{7-\delta}$ (YBCO) ($T_C = 88\,K$) thin films is revealed in time domain reflectivity measurements by an increase of $\Delta R(\omega, t)/R_0$ in the visible region[174, 175]. Together with this, the formation of the superconducting phase results in the appearance in the transient reflectivity of an oscillation ascribed to the Ba vibrational mode ($\nu = 3.6\,THz$)[175–179]. As opposed to other vibrational modes, whose response are only weakly influenced by the appearance of superconductivity, the amplitude of the Ba out of plane vibrational mode, which is within the noise level at high temperature, sets in at T_C and increases upon cooling.

It is generally believed that the oscillations observed in time resolved reflectivity measurements are due to the displacive excitation of coherent phonons (DECP)[180]. In DECP the sudden off-equilibrium electronic population modifies the position of the ions inducing breathing vibrational modes[180]. The DECP has been extensively used in order to describe coherent phonons in YBCO[175, 181, 182]. In such a framework, calculations of the amplitude of

the oscillations based on microscopic parameters given by the density functional theory rationalized the different behavior of the low frequency phonon modes[181]. More recently, however, a novel experimental approach questioned the validity of DECP in YBCO. The analysis of the relation between the nonlinearities in the electronic and phononic contributions indicates that the coherent response could arise from a collection of localized lattice oscillations allegedly generated by polarons melted by photoexcitations[183].

7.2 Results

We performed broadband probe ($450 - 900\,nm$) and NIR pump ($1300\,nm$) measurements on optimally doped YBCO. The relative variation of the reflectivity $\frac{\Delta R}{R}(\omega, t) = \frac{R(\omega,t)-R_0(\omega)}{R_0(\omega)}$, with $R_0(\omega)$ static reflectivity and $R(\omega, t)$ the pump-perturbed one, was measured as a function of temperature and pump fluence. A typical measurement is shown in Fig.7.1 at low temperature and low pump fluence. The advantages of broadband probing are evident: besides the typical temporal traces of single colour pump-probe experiments (i.e. the black curve in Fig.7.1), also the wavelength dispersion at each pump-probe delay is collected (the red curve in Fig.7.1, for example). The amplitude of the relative variation of the reflectivity is displayed with a colour scale.

We notice that $\Delta R/R$ is characterized by both a non-oscillating part, in the following named transient, and a coherent phonon contribution. In the next two paragraphs we address separately these two components.

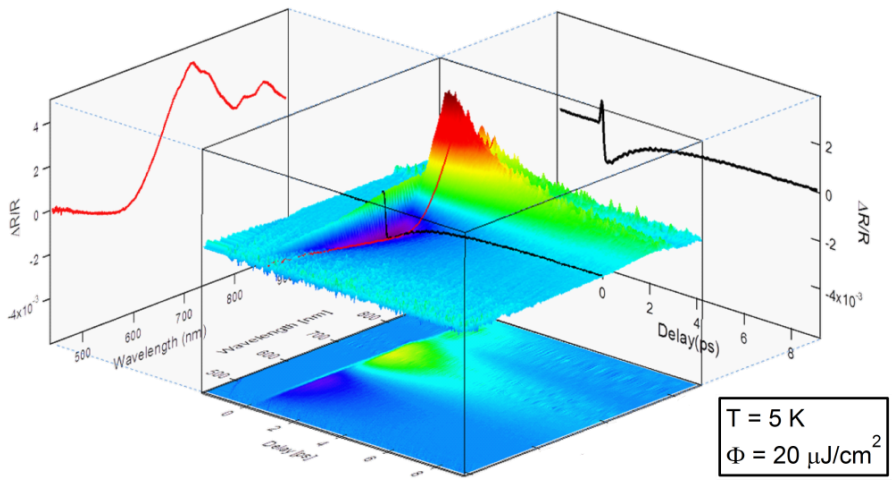

Figure 7.1: $0.95\,eV$ pump and broadband probe measurements on optimally doped YBCO, at $5\,K$ and $20\,\mu J/cm^2$.

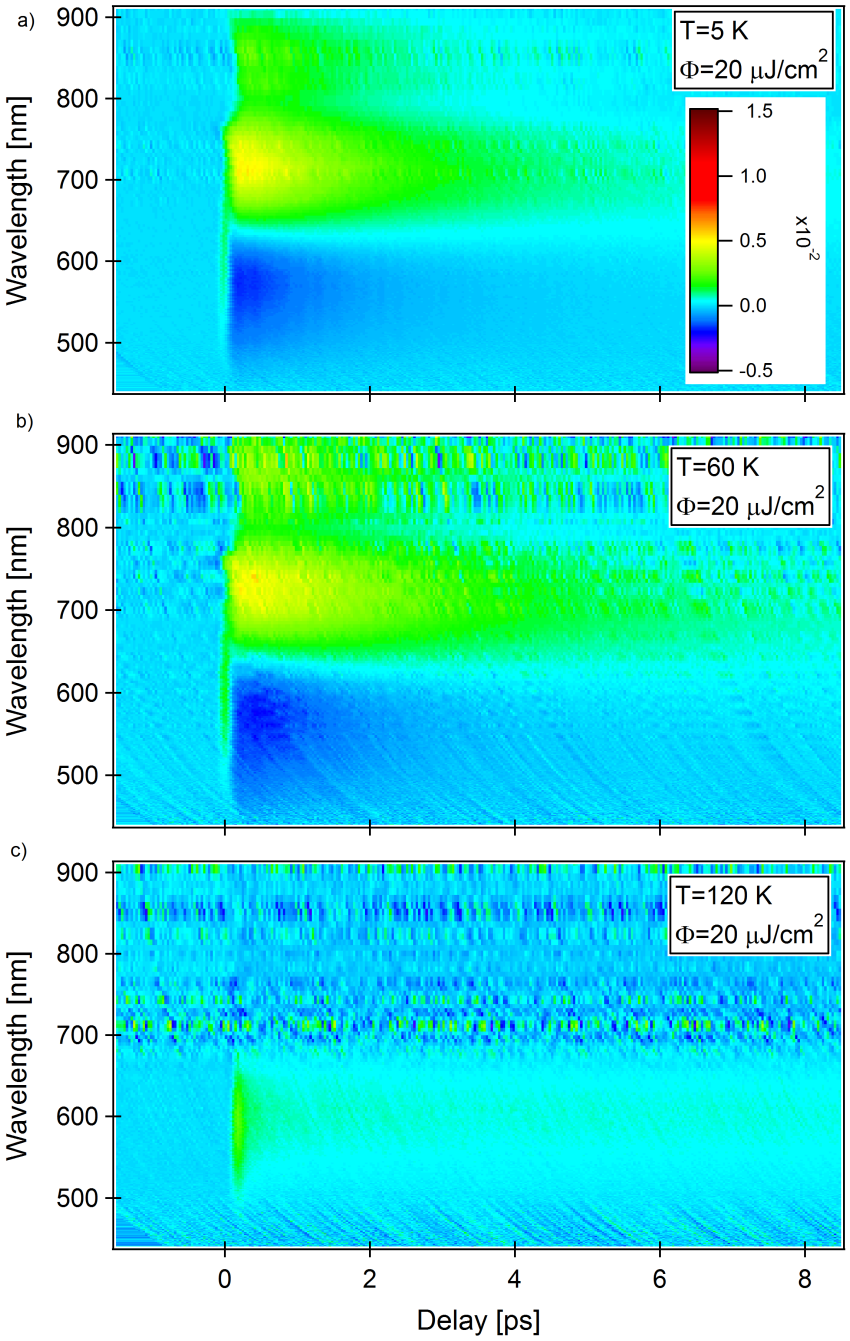

Figure 7.2: Pump and probe measurements based on 1300 nm pump and white light supercontinuum probe as a function of temperature. The transient reflectance in the visible region with low pump intensity ($20\,\mu J/cm^2$) at $5\,K$ (a), $60\,K$ (b), and $120\,K$ (c) is shown.

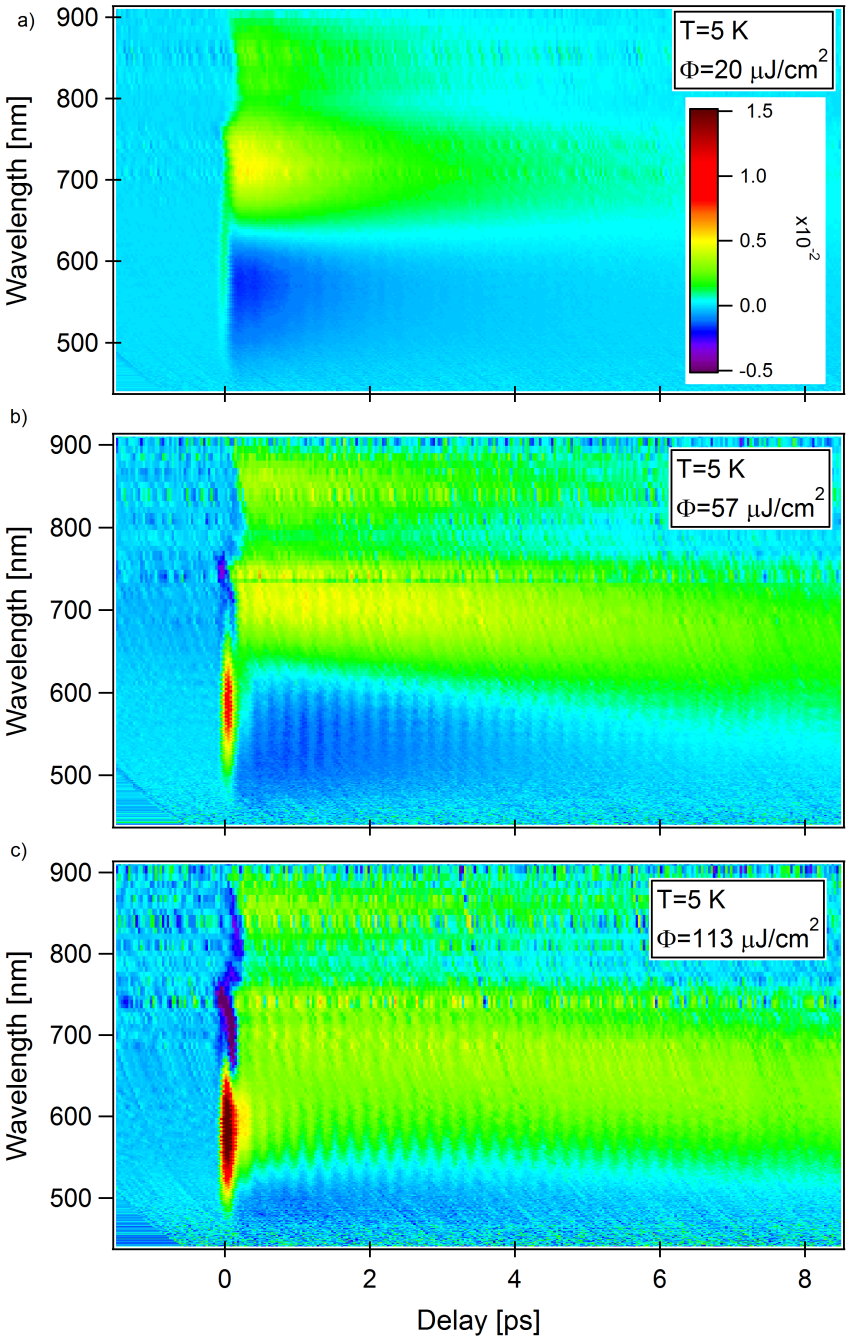

Figure 7.3: Pump and probe measurements based on 1300 nm pump and white light supercontinuum probe as a function of fluence. The transient reflectance in the visible region at 5 K and different pump fluences is reported: 20 $\mu J/cm^2$ (a), 57 $\mu J/cm^2$ (b), and 113 $\mu J/cm^2$ (c).

7.2.1 Transient reflectivity

Fig.7.2,7.3 shows a series of pump-probe data collected as a function of both temperature and pump fluence. In Fig.7.2, the low fluence ($20\,\mu J/cm^2$) data are reported for various temperatures ($5\,K$, $60\,K$, and $120\,K$). In the normal state (Fig.7.2c) $\Delta R/R$ has a positive and fast response in the $500-700\,nm$ range. The dynamics are characterized by a double exponential decay with times $\tau_1 < 0.1\,ps$ and $\tau_2 \approx 1\,ps$. In the superconducting phase ($T < T_C$) the transient reflectivity displays slower dynamics: a negative response appears below $\approx 600\,nm$, and a positive one above (Fig.7.2a,b). This negative-to-positive response for increasing wavelengths might be the result of the shift of the underlying interband transition at about $1.9\,eV$. In fact, if such transition softens, we expect a negative response at higher energies (lower wavelengths) and a positive transient at lower energies (higher wavelengths). This is consistent with the static data[8], as the formation of the superconducting (SC) state affects the high-energy static optical response in the cuprates. In fact, in time-resolved measurements the pump perturbs the population of condensed Cooper pairs[26] and, hence, the reflectivity in the visible range.

In Fig.7.3 the measurements at $5\,K$ and different pump fluences ($20\,\mu J/cm^2$, $57\,\mu J/cm^2$, and $113\,\mu J/cm^2$) are shown. The effect of increasing the pump energy at low temperature is evident: the typical transient response associated to the condensate is progressively washed out (Fig.7.3b,c). In particular, the slower negative dynamic below $\approx 600\,nm$ is quenched, while the respose approaches the one of the normal state at longer timescales.

In Fig.7.4 we compare the non-oscillating contribution to the transient response at the pump-probe delays of $0\,ps$, $1\,ps$, and $5\,ps$ for different values of temperature and pump fluence. The non-superconducting response is shown in orange ($120\,K$ and low fluence), in blue and green the low-fluence data below T_C, associated to the optical response of the condensate, are reported. The high-fluence relative variation of reflectivity in the superconducting state is depicted in purple and red ($T = 5\,K$, $\Phi > 57\,\mu J/cm^2$). Fig.7.4a shows the data for zero pump-probe delay: the normal response is positive in the $\approx 500-700\,nm$ range (orange) while the condensate displays a broadband positive transient for low fluence (green and blue curves for $T = 60\,K$ and $T = 5\,K$, respectively.). From the comparison of the high fluence (purple and red) and high temperature data (orange) it's evident that, when the pump fluence is increased in the SC phase, the transient response closely resembles the normal one. This suggests that for high fluences (higher than $\approx 50\,\mu J/cm^2$) the condensate is instantly vaporized by the pump pulses. This is qualitatively consistent with previous works on $La_2Sr_{2-x}CuO_4$[16] and $Bi_2Sr_2Ca_{1-x}Y_xCu_2O_{8+\delta}$[18]. The energy dispersion of the relative variation of reflectivity for pump-probe delays equal to $1\,ps$ and $5\,ps$ is shown in Fig.7.4b and Fig.7.4c, respectively. For both delays the condensate response is negative below $\approx 600\,nm$ and positive above (blue and green curves). The transient reflectivity when the SC state is photo-destroyed (purple and red curves) ap-

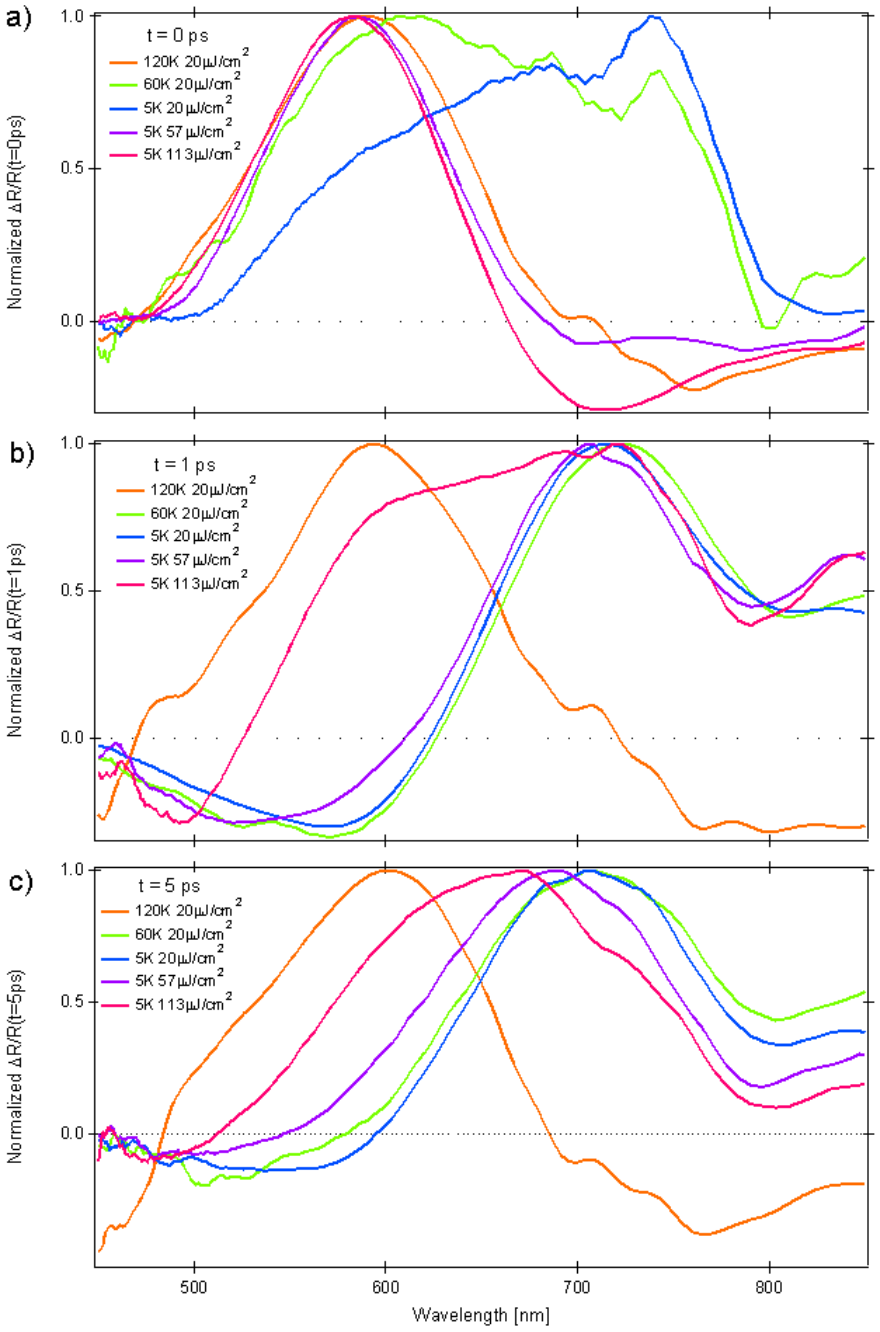

Figure 7.4: Wavelength dependence of the transient reflectivity $\frac{\Delta R}{R_0}(\omega, t)$ for pump-probe delays equal to $t = 0\,ps$ (a), $t = 1\,ps$ (b), and $t = 5\,ps$ (c) for measurements performed at different temperatures and pump intensities. The $\Delta R/R$ is normalized in order to allow a visual comparison. The measurements for different temperatures at low fluence ($20\,\mu J/cm^2$) and for different fluences at low temperature ($5\,K$) are reported. Note that the measurements at $120\,K$ (orange curves) are not reliable for $\lambda > 700\,nm$.

proaches the superconductor response for longer pump-probe delays. This suggests that the condensate is reforming after the pump arrival with a timescale of few picoseconds.

7.2.2 Coherent phonons

In this section we analyze the oscillating contribution to the relative variation of the reflectivity displayed in Fig.7.2,7.3. We introduce the discussion starting from the simplified case of a single colour probe data, the detailed analysis of the broadband data is reported in the following paragraph. Fig.7.5a display the transient reflectance at $\lambda = 540\,nm$ above and below T_C. We perform a multi-exponential fit, subtract it to the data, and obtain the coherent residual contribution shown in the insert of Fig.7.5c.

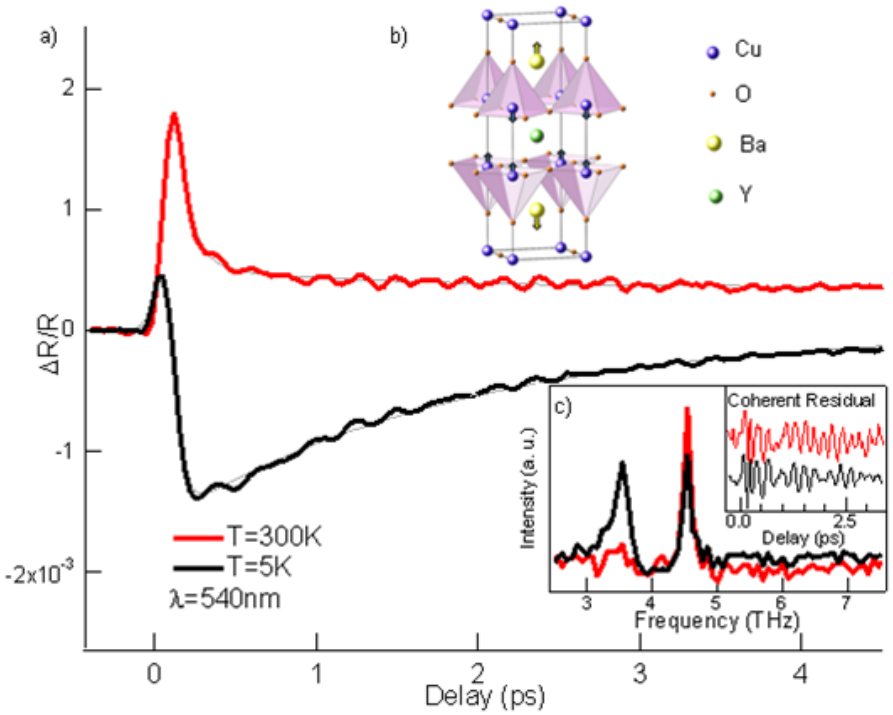

Figure 7.5: a) Transient reflectivity representative of the normal (red) and the superconducting phase (black). b) Sketch of the structure of YBCO. The arrows represent the displacement associated to the phonon modes under investigation. c) The coherent contribution to the reflectivity is different for the normal and superconducting phase. While in the normal state only one vibrational mode is identified (red), upon entering the superconducting phase two phonons are observed (black).

The oscillating part is characterized by one principal frequency above T_C, while there are beatings (i.e. two frequencies) below the critical temperature. Two phonon modes at about $3.6\,THz$ and $4.5\,THz$ can be easily detected. These two modes, already observed in static Raman[177, 184–186] and in time resolved experiments[176, 178, 182], are assigned to A_g modes, only weakly mixed with oxygens, and represent almost pure Ba and Cu off-plane

vibrations[177] (see Fig.7.5b). Now we exploit the broadband probe. Fig.7.6 reports the normalized residual coherent response for the two phonon modes versus wavelength and temperature (see Par.7.3 for the complete analysis procedure). The wavelength dispersion of the two modes is different: the Ba mode ($3.6\,THz$) peaks at $540\,nm$ (Fig.7.6c) and the Cu mode ($4.5\,THz$) at about $580\,nm$, as shown in Fig.7.6a and Fig.7.6b. It is evident that the Cu vibration is barely sensible to the formation of the condensate, as either the temperature (Fig.7.6a) and pump intensity (Fig.7.6b) dependence of the energy dispersion of this mode is not affected. On the other hand, the Ba mode is strictly related to the superconducting phase, as evidenced by Fig.7.7. The ratio of the integrals of the wavelength dispersions (from $620\,nm$ to $785\,nm$) of the Ba mode over the Cu one is reported as a function of temperature in Fig.7.7a, and as a function of fluence in Fig.7.7b. The Ba vibration is strongly enhanced upon entering the superconducting phase and vanishes above T_C (Fig.7.7a).

The fluence scan at very low temperature (Fig.7.7b) reveals that the Ba mode is depleted in comparison to the Cu mode when the density of Cooper pairs is reduced by photo-exctation and the condensate is partially melted. This evidence underlines the strong coupling of the Ba off-plane vibration to the superconducting phase. Moreover, we stress that while the amplitude of the Ba mode vanishes at $T > T_C$, it does not vanish at low temperature and high fluences (see Fig.7.7b).

The energy dispersion of the Cu mode ($4.5\,THz$) is unaffected by either temperature (Fig.7.6a) and fluence (Fig.7.6b) variations. On the contrary, the wavelength distribution of the low-frequency coherent phonon is both quenched above T_C (Fig.7.6c) and dramatically perturbed upon increasing the pump fluence, as shown in Fig.7.6d. In Par.7.2.1 we interpreted the negative-to-positive transient reflectivity at low temperatures and fluences (Fig.7.2a,b, Fig.7.3a,b) as the result of the softening of an underlying interband optical transition. In this framework, the distribution of wavelengths of the Ba mode may be linked to the shift of the intraband oscillation upon perturbing the SC phase[26]. In a naive picture, we expect that the shift of the interband transition increases as a function of the pump fluence, and that the softening is mapped on the wavelength dispersion of each coherent phonon directly coupled to that transition. This simple interpretation is confirmed by Fig.7.6d: upon increasing the pump fluence, the wavelength dispersion of the Ba mode peaks at higher (lower) wavelength (energy). The Ba mode is hence a direct probe for the underlying interband transition, and its behaviour can be used to shine new light on the anomalous spectral weight distribution of the intergap and Drude bands in the cuprates below T_C. However, this intriguing scenario lacks a theoretical framework: several possibilities are currently under inversigation, ranging from structural effects to pump-induced oscillations of the SC gap[187].

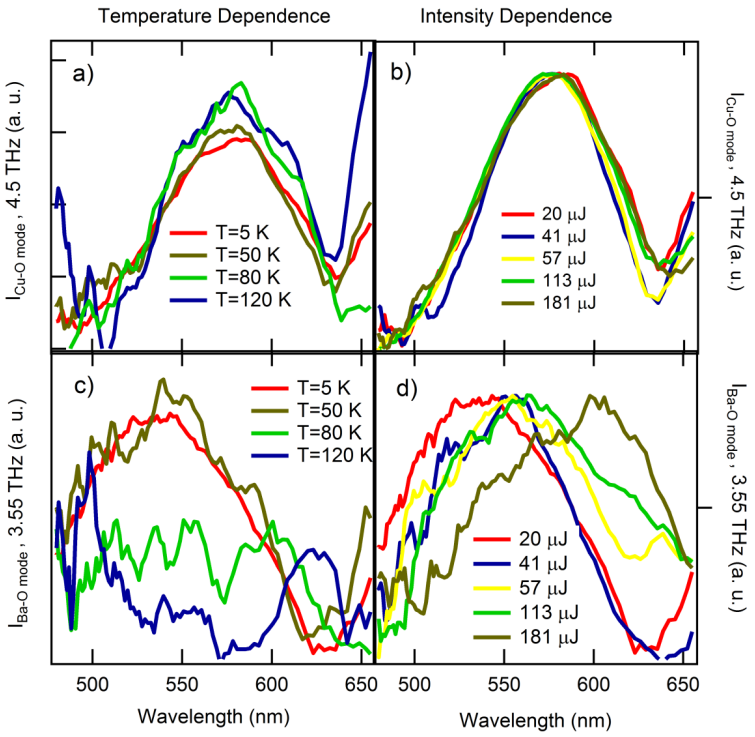

Figure 7.6: a) and c) report the amplitudes of the vibrational modes as a function of temperature and wavelength. b) and d) report the amplitudes of the modes depending on the pump intensity. Note that the amplitudes in b) and d) are normalized in order to highlight the different behavior of the two modes. The temperature data (a,c) are shown for pump fluence equal to $20\,\mu J/cm^2$. The fluence data (b,d) are shown at $5\,K$.

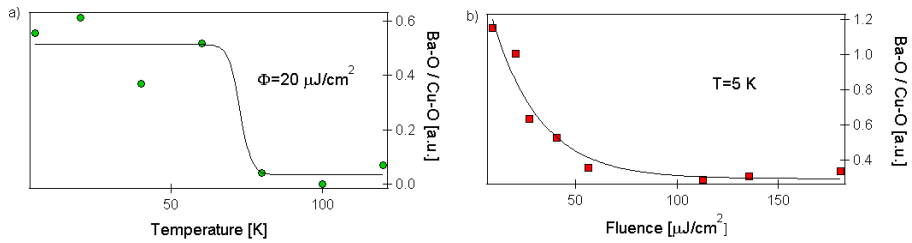

Figure 7.7: Ratios of the integrated dispersion of the phonon modes as a function of temperature (a) and fluence (b). The wavelength dispersion is integrated between $620\,nm$ and $785\,nm$. In a) the ratio between the integration of the Ba phonon and the integration of the Cu vibration is reported as a function of temperature and for fixed fluence $\Phi = 20\,\mu J/cm^2$. In b) the same ratio is reported as a function of fluence for the fixed temperature of $T = 5\,K$. The solid black lines are guides for the eyes.

7.3 Methods

The YBCO films of $(100 \pm 10)\,nm$ where grown by hetero-epitaxy on STO and have the same orientation as the substrate, i.e. the c-axis points out of the plane. The oxygen content is close to the optimal doping level with T_C between $88\,K$ and $90\,K$. The pump and probe experiments were based on white light supercontinuum probes. The pump pulses where $80\,fs$ long with central wavelength of $1300\,nm$. The transient reflectance was measured with broadband white-light (WL) probes generated in a sapphire crystal by non-linear optical effects ($400 - 1000\,nm$, $< 5\,\mu J/cm^2$, see Ch.4). The data presented are corrected of a linear chirp accounting for the dispersion of the WL generation process. The fluence and temperature at which the measurements were collected are reported in the captions of Fig.7.1-7.3.

The coherent phonon contribution to the reflectivity has been extracted from the data by means of the following procedure. At first, the data have been fitted with a multi-exponential decay multiplied by a step function. Secondly, the fit obtained have been subtracted to the data. Fig.7.8a shows, as an example, the residual wavelength-dependent coherent contribution in the time domain for the measurement at $5\,K$ and $20\,\mu J/cm^2$. On the residual a Fourier analysis is performed in order to obtain the amplitude of the phonon modes at each wavelength, and its wavelength dependence is plotted in false colours in Fig.7.8b. The Fourier analysis reveals two modes at frequencies of about $3.5\,THz$ and $4.5\,THz$. The wavelength dispersion of these modes is readily obtained from Fig.7.8b by integration of the Fourier amplitude over the limited frequency ranges of $3.4 - 3.6\,THz$ and $4.4 - 4.6\,THz$: the amplitude of the phonon modes as a function of energy is shown in Fig.7.8c.

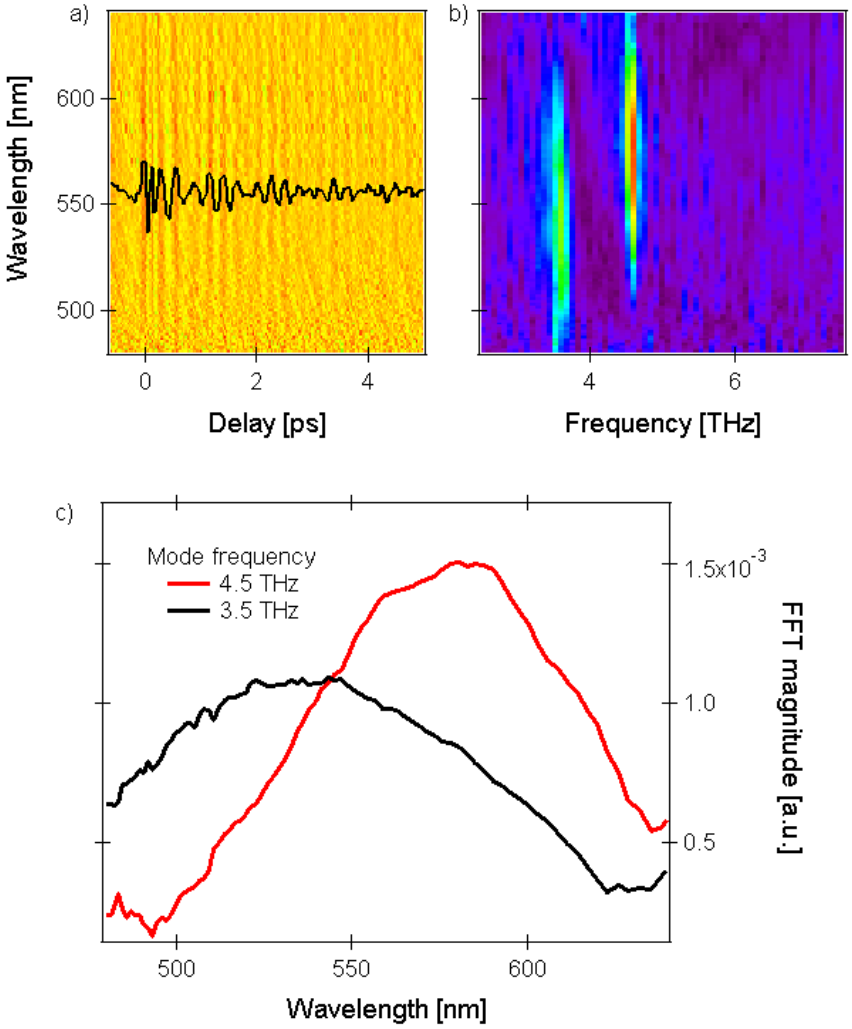

Figure 7.8: a) Coherent part of the transient reflectivity at $5\,K$ and $20\,\mu J/cm^2$. The amplitude of the phonon modes in the frequency domain at all wavelength (b) is obtained by Fourier transforming the time traces (a). The amplitude of the phonon modes at the different wavelengths is reported in c).

Chapter 8

Phase sensitive measurements of a novel light-matter interaction regime in $GaAs$

The speed of ultra-fast optical switches is generally limited by the intrinsic electronic response time of the material. Here we show that the phase content of selected electromagnetic pulses can be used to measure the timescales characteristic for the different regimes of matter-light interaction. By means of combined single cycle THz pumps and broadband optical probes, we explore the field-induced opacity in GaAs (the Franz-Keldysh effect). The first paragraph of this chapter recalls the basic concepts of matter-light interaction and of the Franz-Keldysh effect on simple semiconductors. The THz pump and broadband probe data are reported in the following, as the discussion where a novel regime of matter-light interaction with unexpected quantum memory effects is suggested.

8.1 Introduction

The intrinsic charge carrier dynamics limits the speed at which material properties can be manipulated by an electromagnetic (EM) pulse[19, 20, 38]. When the characteristic electronic timescale is comparable to the duration of a single cycle of the EM field, the details of the field carrier-envelope phase determine the material response. Under these conditions matter can be excited into the non-perturbative regime[188–191] and a full quantum mechanical treatment is needed. An important quantity describing the "strength" of the field-matter interaction is the ponderomotive energy[192, 193]

$$U_P = \frac{e^2 E_0^2}{4m\Omega^2} = h\Omega \cdot \gamma, \tag{8.1}$$

which is defined as the mean kinetic energy of a particle of mass m and charge e which oscillates in the ac-electric field $E(t) = E_0 cos(\Omega t)$. For $\gamma \ll 1$ the

matter-field interactions can be described perturbatively while for $\gamma \gg 1$ the field strength is much larger than the photon energy and the field-induced effects are dominant.

Here we report a study of the dynamical Franz Keldysh effect (DFKE) in the transition region between those two limits ($1 < \gamma < 30$). Single-cycle THz electromagnetic pulses with maximum field amplitudes between $30\,kV/cm$ ($\gamma \approx 2$) and $100\,kV/cm$ ($\gamma \approx 27$) are used to gate the transmission in bulk gallium arsenide. The changes in transmission are dramatic and equal 60% transmission loss through a $0.4\,mm$ sample. Our amplitude and phase-dependent study of the THz-induced opacity in bulk GaAs allows for the identification of a novel anomalous regime of the Franz Keldysh effect (FKE), that has a static intensity dependence but a highly non-trivial phase evolution.

The static Franz Keldysh effect can be described as follows: in a semiconductor, the relative motion of an electron-hole pair in a uniform and static electric field F is described by a one-dimensional and time-independent Schrödinger equation,

$$\left(\frac{h^2}{2\mu}\frac{\partial^2}{\partial z^2} + |e|Fz + E_z\right)\phi(z) = 0, \tag{8.2}$$

whose solution is an Airy function[41, 194–196] $\phi(z) \rightarrow \phi(\xi) \propto Airy(\xi)$ obtained by the substitution $z \rightarrow \xi = -\frac{E_z}{\sigma(F)} - z(\frac{2\mu|e|F}{h^2})^{1/3}$, with $\sigma(F) = (\frac{e^2h^2F^2}{2\mu})^{1/3}$ the "electro-optical energy" of the field. The Airy function contains the salient features of the static FKE: it has an exponential tail for small and negative values of the argument (that can be related to below-gap field-induced absorption), and it approaches a plane-wave like solution for positive and increasing arguments (implying the above-gap oscillations). Fig.8.1a shows the absorption of a conventional semiconductor in a static and uniform electric field. The standard "square root" absorption (black curve) in the presence of an electric field (red curve) is strongly perturbed in the energy region across the band-gap E_{Gap}[197, 198]: an exponential-tail absorption appears below E_{Gap} (also known as electroabsorption) and an oscillatory behaviour in frequency of the optical properties of the semiconductor is revealed above the energy of the gap.

When the static electric field is replaced by a time dependent one (Fig.8.1b) the response of the system is described by the Dynamical Franz-Keldysh effect (DFKE)[199, 200]. The DFKE is qualitatively similar to the static FKE below the gap (i.e. both effects exhibit an exponential absorption tail[201]) but the above-gap oscillations are much weaker and the absorption edge is blue-shifted by the ponderomotive energy U_P[193, 202]. When U_P is of the same order of magnitude of the photon energy ($\gamma \approx 1$) the conduction and valence bands cannot follow adiabatically the applied EM field and the field-induced opacity is better described by the DFKE. On the other hand, for growing U_P ($\gamma \gg 1$) the effects become better and better described by a quasi-static FKE, which is the proper model for a uniform dc field ($\gamma \rightarrow \infty$).

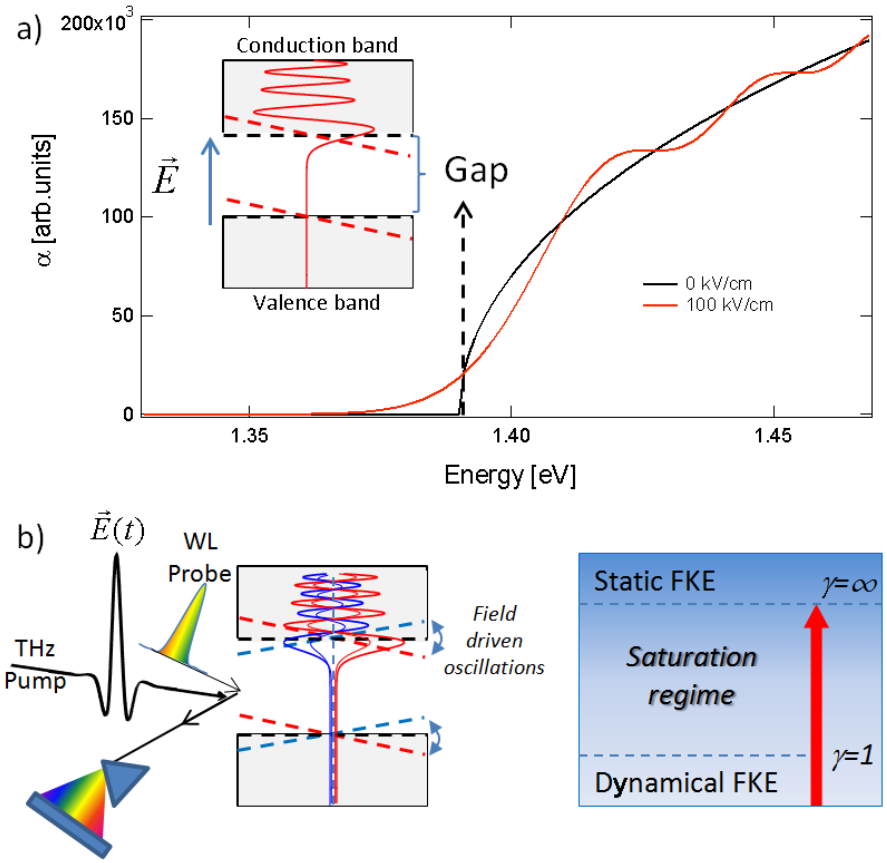

Figure 8.1: The Franz-Keldysh effect. a) The unperturbed absorption edge of a semiconductor (black curve) displays, in a uniform electric field, below-gap absorption and above-gap oscillations (red curve). Insert: a static electric field tilts the bands improving the sub-gap tunnelling that leads to below-gap absorption. b) Dynamical Franz-Keldysh effect detected by pump-probe THz spectroscopy. The bands are tilted with a non-trivial phase relation with the applied ac field. Right: sketch of the two limits of the FKE, that is static for infinite γ and dynamic for γ close to 1 (see text).

8.2 Results

8.2.1 Field induced optical absorption experiments

Here we study the FKE at the transition between a dynamical ($\gamma \approx 1$) and a quasi-static regime ($\gamma = 30 \gg 1$). To this purpose we developed a pump-probe experiment which uses strong almost single cycle EM pulses at THz frequencies as pump and broadband pulses as probe. It is important to note that the probe pulses used in our experiments are shorter than the THz wavelengths so that our technique allows the phase sensitive measurement of the DFKE. Fig.8.2 shows the THz electric field in the time domain (Fig.8.2a) and a spectrogram of the observed transmission change $\Delta T(t)/T$, where $\Delta T(t)$ is the time-dependent perturbed transmission and T is the field-free transmission in GaAs (Fig.8.2b). At the peak of the THz field the transmission is reduced by up to 60% (Fig.8.2b) at photon energies just below the band gap. This large modulation is caused by the strong sub-gap absorption as shown for the static FKE in Fig.8.1a.

Fig.8.2c shows the measured $\Delta T(t = 0ps)/T$ as function of photon energy (red curve) compared to the transmission change calculated from eq.8.2[67] assuming a static electric field of $100\,kV/cm$ (black curve) and a square-root gap. The only free parameter of the calculation is a phenomenological scaling factor accounting for the size of the matrix elements of the dipole transitions. It should be noted that taking into account realistic shapes of the equilibrium absorption (including excitonic effects), rather than a simple square-root gap, gives only minor differences in the field driven absorption.

While the shape of the changes as a function of the photon energy is accurately described at every time step, a comparison between Fig.8.2a and Fig.8.2b reveals that we cannot reproduce the observed temporal dependence of the transient transmission by calculating the static FKE with the THz field profile shown in Fig.8.2a. Nontheless, this suggest that an effective electric field can describe the temporal evolution of the transients, as will be discussed in the following.

8.2.2 THz pump reflectivity probe

In order to study the transition region between the static and dynamical FKE, and to elucidate the phase evolution of the field-induced variations of the optical properties, we carried out single-colour reflectivity measurements for different pump intensities ($1 < \gamma < 30$). Reflection geometry experiments increase temporal resolution by avoiding the dephasing of pump and probe pulses due to the slightly different group velocities in a bulk sample.

Fig.8.3b shows the reflectivity change $\Delta R(t)/R$ at $900\,nm$ induced by the presence of the strong field in Fig.8.3a. The shape of the transient reflectivity changes dramatically as a function of the pump field strength (Fig.8.3b). In order to highlight the main result of this report, i.e. the different phase content

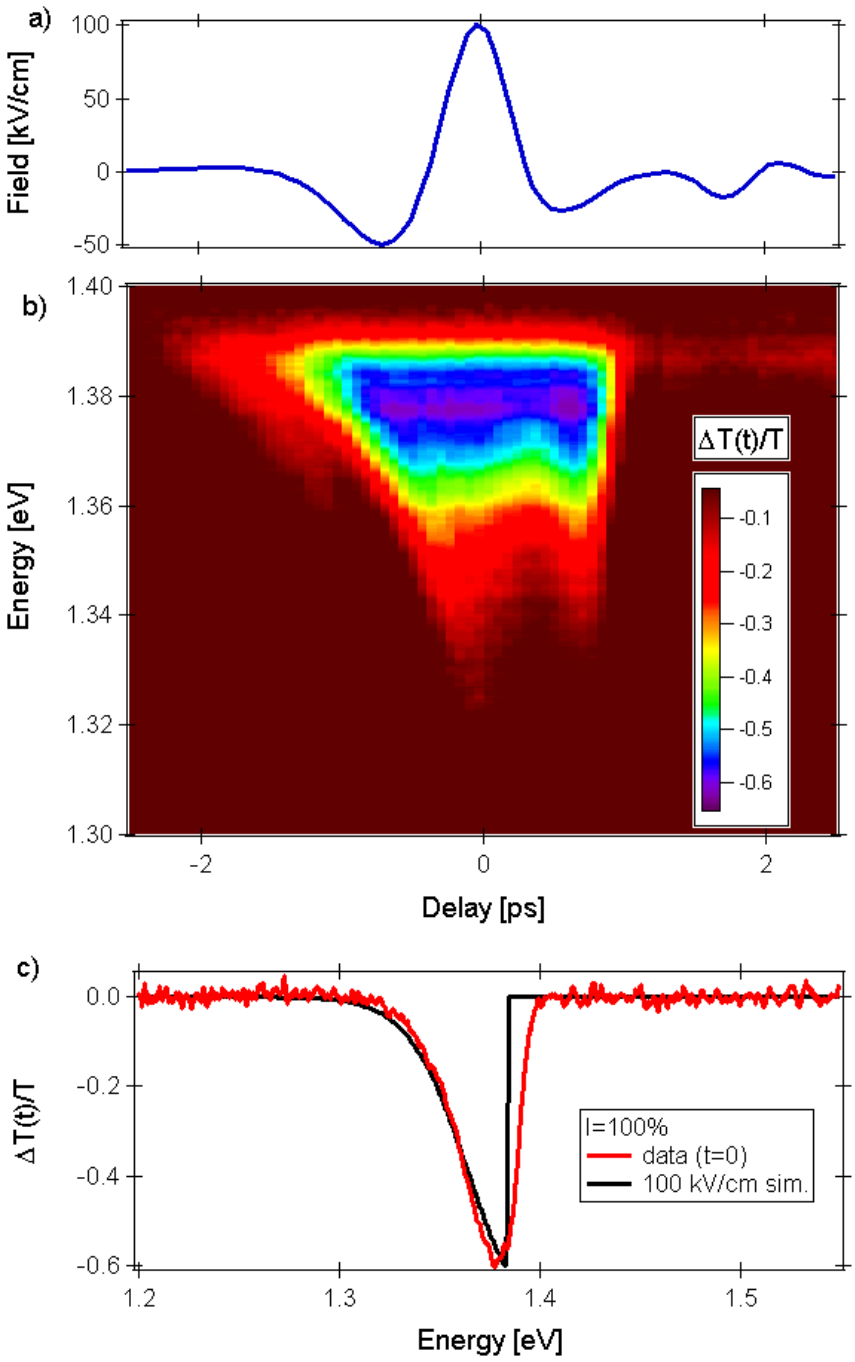

Figure 8.2: THz-driven Franz-Keldysh effect. (a) THz field detected by electro-optical sampling. (b) Time-resolved variation of the transmission in GaAs as a function of pump-probe delay and probed energy. (c) Wavelength-dependent Franz-Keldysh effect. Vertical section at t=0 (red curve) and simulation based on the static FK effect with an applied field of $100\,kV/cm$ (black curve). Note that (a) and (b) have the same abscissa.

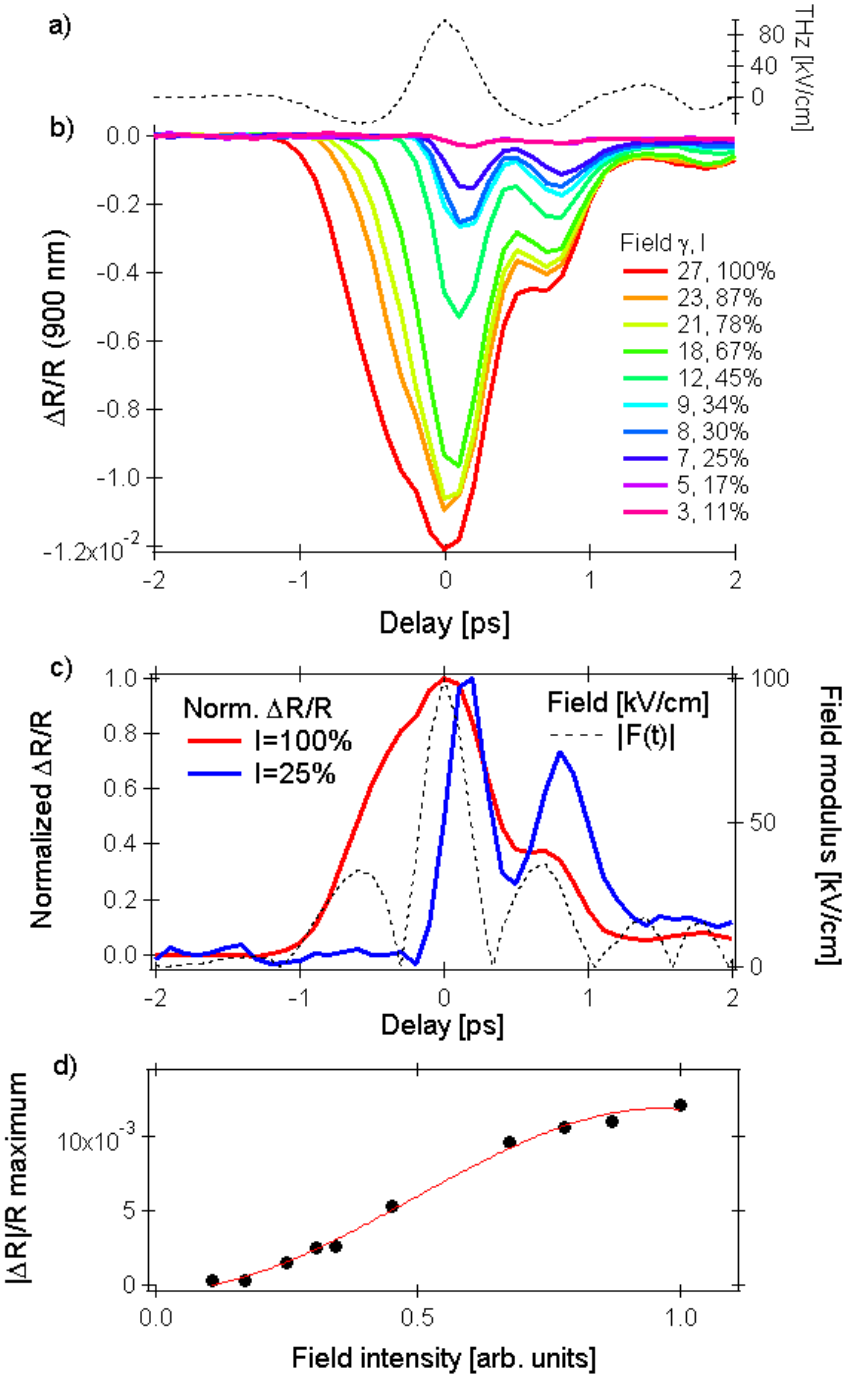

Figure 8.3: THz driven reflectivity changes. a) Pump electric field temporal profile measured by electro optical sampling. b) Transient reflectance induced by electric field of different intensity (γ is the Keldysh parameter, see text for details). c) Normalized relative variation of the reflectivity at $900\,nm$ ($1.38\,eV$) for highest (red) and lowest (blue) pump intensities. The absolute value of the THz field, whose phase content is independent on the intensity of the pump, is reported for comparison (dashed black curve). d) Maximum value of $\Delta R(\omega,t)/R_0(\omega)$ as a function of pump amplitude. The red line is a guide for the eyes.

of the response to fields with different intensities, in Fig.8.3c we plot the normalized $\Delta R(t)/R$ at low and high pump intensity together with the modulus of the THz field (dashed line). Fig.8.3d shows the maximum $\Delta R/R$ versus THz field strength. We observe an almost linear dependence for $\Delta R/R$ up to $I \approx 50\%$, while a sub-linear behaviour appears at higher field strengths. From the theory of the static FKE we expect that the pump-induced opacity scales with the amplitude of the applied electric field[203], while the DFKE predicts a linear dependence with pump intensity[201]. Hence, from the maximum amplitude of the transient reflectivity (Fig.8.3d), we can identify a dynamical Franz-Keldysh regime for low THz fields and an anomalous behaviour for field strengths higher than $70\,kV/cm$. The analysis of the transient reflectance in this regime reveals a "static-like" behaviour, i.e. a linear dependence of the maximum of ΔR on the field amplitude.

8.3 Discussion

As indicated earlier, a static FKE model can describe the transient transmission at all wavelengths at each time delay (Fig.8.2c) once a parameterized electric field is provided. This evidence leads us in the search of a phenomenological expression for an effective ac field that, once used within the static FKE theoretical framework, reproduces the fluence and phase dependent evolution of the transient reflectivity reported in Fig.8.3b.

In order to describe the anomalous regime investigated we follow an heuristic approach. When the potential in eq.8.2 is a function of time, the corresponding one-dimensional time-dependent Schrödinger equation[204–206], with a potential that is linear in the space variable, has a solution known as Airy packet[206]. The Airy packet is similar to the Airy function, which is the solution to the static case, but its argument depends on the integral of the potential over time.

By inspection of the blue curve in Fig.8.3c ($\gamma \sim 7$) we notice that for low intensity the peak in the THz field at $t = -0.6\,ps$ (dashed line) has no effect on the transient reflectivity. Moreover, at later times ($t = +0.7\,ps$) the second peak in the field gives rise, slightly shifted, to a large variation of the reflectivity. The ratio of the THz field at $t = +0.7\,ps$ over the one at $t = 0\,ps$ is much smaller than the ratio of the two highest variations in reflectivity $\Delta R(t = 0.9\,ps)/\Delta R(t = 0.1\,ps)$. This indicates that, for low pump intensities, the optical response at time t has memory of the THz field at all previous times or, equivalently, that an integral function of the potential is governing the transient optical properties. This behaviour is consistent with the solution of Berry[206] and with the expectation in the dynamical regime of the Franz-Keldysh effect.

The phase dependence of the transient reflectivity is dramatically modified upon increasing the strength of the ac field (red curve in Fig.8.3a). For $\gamma >> 1$ we expect to move towards the static regime with a response that follows

adiabatically the THz electric field. However, our measurements in strong field (red curve in Fig.8.3c) reveal that the relative variation of the reflectivity does not follow the THz amplitude, but shows mixed character between the static and dynamical regimes as highlighted by the non-vanishing response in the minima of the applied electric field ($t \approx -0.2\,ps$ and $t \approx +0.2\,ps$). As expected for a quasi-static FKE the transient reflectivity is maximum for the field peaks ($t \approx -0.6\,ps$, $t \approx 0\,ps$, and $t \approx +0.7\,ps$). Nevertheless $\Delta R(t)/R$ is non zero on the overall THz envelope and moreover the transient at $t \approx -0.6\,ps$ is much higher with respect to the one due to the central THz peak ($t \approx 0\,ps$). This indicates that for strong fields we are exploring a saturation regime of the dynamical Franz Keldysh where memory effects are of relevance.

Led by all the previous consideration we could formulate a phenomenological expression for the effective ac field $F_{eff}(p,t)$ to be used within a dc FK model that allows to describe our observations

$$F_{eff}(p,t) = \alpha(p)(|F(t)|\frac{A(I^2(t))}{1+B(I^4(t))}g(p,t)), \tag{8.3}$$

where $F(t)$ is the THz field amplitude (which is an experimental input measured by electro-optical sampling), $I(t) = F^2(t)$ is the time-dependent intensity, A and B are integral functions of their respective arguments, p is the normalized peak intensity, $\alpha(p)$ a phenomenological analytical function of p, and $g(p,t)$ a convoluted gaussian function. The explicit form of eq.8.3 can be found in the appendix.

In Fig.8.4a we plot the measured $\Delta R(t)/R$ and the results of the simulation with the effective field given in eq.8.3 for different pump intensities. Apart from the slow dynamics observed at delays higher than $2\,ps$, that are related to incoherent pump-induced heating effects not included in eq.8.3, our model contains the main features of the temporal and intensity dependence of the transient reflectivity probed at $900\,nm$. At low intensities the effective field is dominated by the contribution $A(I^2(t))$ which is consistent with the DFKE regime where the solution of the time-dependent Schrödinger equation depends on the integral of the potential over time[206]. On the other hand, when the intensity is increased, F_{eff} is suppressed by the renormalization due to higher order corrections at the denominator, leading to the recovery of the sub-linear dependence in the field intensity characteristic of the static FKE. The anomalous phase-dependence of the FKE with strong pump originates in our model from both the gaussian convolution, that phenomenologically takes into account the "broadening" at high fields (see the red curve in Fig.8.3c), and the integral of the higher order power of the intensity at the denominator. This renormalization describes how the optical response of GaAs at time t still carries a memory of the history of the applied electric field for $\gamma \approx 30$.

In conclusion, we performed a systematic study of the transition region between the dynamical and quasi-static regimes of matter-light interaction by detecting the ac field induced opacity in bulk GaAs. The analysis of the dependence of the reflectivity at $900\,nm$ on the EM field amplitude and phase

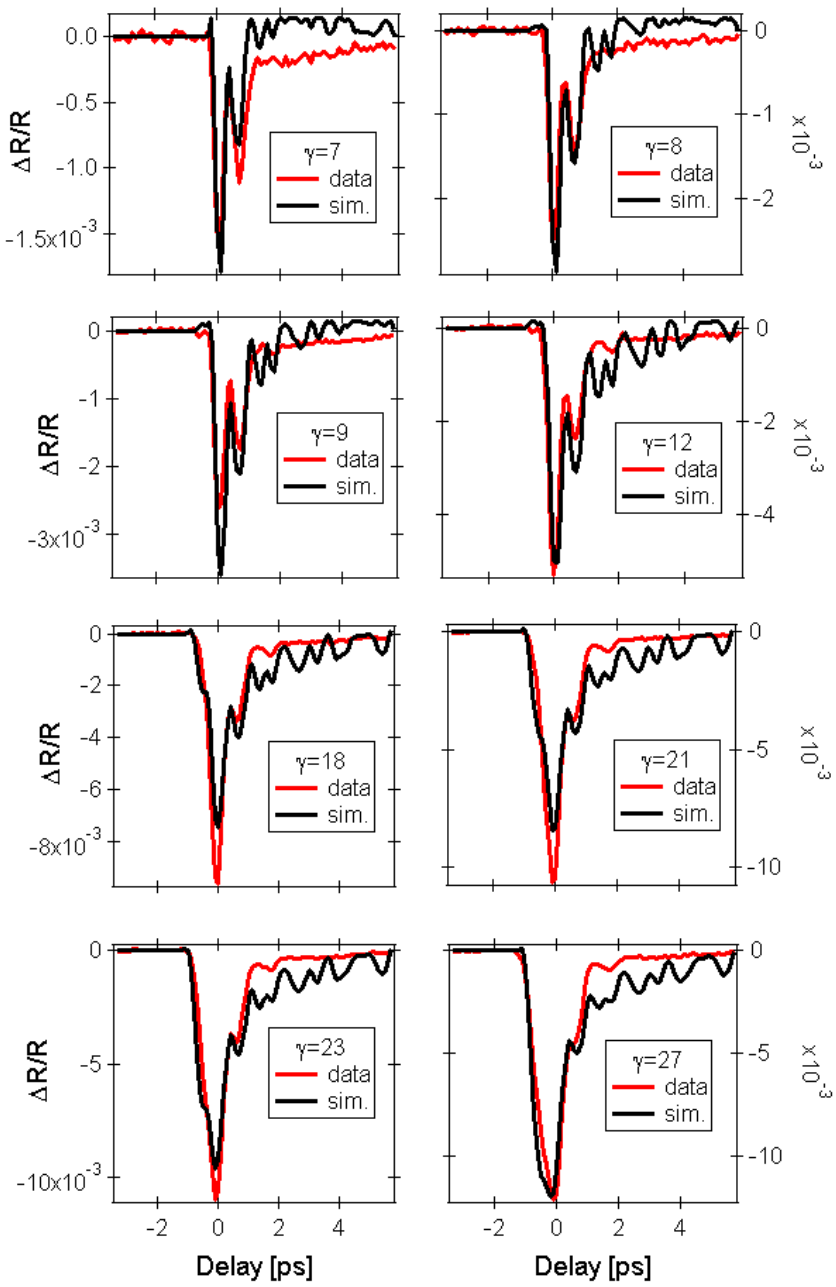

Figure 8.4: Transition from dynamical to quasi-static FKE. a) $\Delta R(\omega, t)/R_0(\omega)$ at $900\,nm$ as a function of γ and time delay, data (red) and model (black).

revealed the existence of a novel regime of saturation for the dynamical Franz-Keldysh effect. Our phase-resolved technique allows to observe directly the memory effects and to establish a phenomenological model that uses the static FKE solution combined with an effective field to describe the new regime. We demonstrate, by tuning the amplitude of single cycle pump pulses, that the temporal response of the optical properties of GaAs exhibits a highly non trivial phase content. Finally, we suggest that this novel regime will be of relevance for ultra-fast optical gating devices.

8.4 Methods

The single-cycle THz pulses, with energies of $2\,\mu J$ and field strengths exceeding $100\,kV/cm$, were generated by optical rectification in $LiNbO_3$ using the tilted pulse front technique[74] (see Ch.4). The pulses were characterized by electro-optical sampling using a $150\,\mu m$ GaP crystal, revealing their field strength and spectral content which is peaked at $0.8\,THz$. The total pulse energy was measured independently with a calibrated pyroelectric detector. A pair of wiregrid polarizers was used for controlled attenuation of the THz field without changing its temporal profile.

We can estimate from eq.8.1, in the free electron approximation and for central frequency $\Omega \approx 1\,THz$, that γ for the EM pulses used in the experiments range from $\gamma \approx 1$ for maximum field strength of $30\,kV/cm$ up to $\gamma \approx 30$ for the pulses with the highest energy ($100\,kV/cm$). As reported in Fig.8.1b, with this field parameters we expect to cross the boundaries between the DFKE and a quasi-static regime upon increasing the field amplitude.

The femtosecond laser pulse was split off to generate white light in a $2\,mm$ thick sapphire plate. The white light was focused onto the sample using a thin CaF_2 lens. The chirp of the probe continuum in the near IR region of interest is estimated to be less than $100\,fs$. A fiber-coupled spectrometer was used to measure the time dependent transmission change $\Delta T(t)/T$. We used a lightly doped n-type GaAs ($8 \cdot 10^{15}\,cm^{-3}$) in order to suppress THz reflections within the sample that would lead to echo artifacts in the time domain data. Additionally, we carried out single-colour pump-probe measurements in reflectivity with bandpass filters ($10\,nm$ FWHM) between the sample and photodetectors.

8.5 Appendix

8.5.1 Complete model for the static Franz-Keldysh effect

We know from textbooks[1, 41] that in the dipole approximation the dielectric function of a crystal is proportional to a sum of matrix elements $|P_{if}|^2 \propto$

$|\langle i|\boldsymbol{r}\cdot\boldsymbol{E}|f\rangle|^2$

$$\epsilon_i(\omega) \propto \frac{1}{\omega^2}\sum_{i<f}\sum_{\boldsymbol{k}_c<\boldsymbol{k}_v}|P_{if}|^2\delta(E_f(\boldsymbol{k}_c)-E_i(\boldsymbol{k}_v)-h\nu). \tag{8.4}$$

If only vertical transitions are allowed we must consider, for each couple of initial and final bands, their entire dispersion at the same $\boldsymbol{k}$. For direct transitions the matrix element P_{if} can be written as[194] $P_{if}=\phi(\boldsymbol{0})\cdot C_0$ with C_0 constant and $\phi(\boldsymbol{r})$ solution of the two-particle electron-hole pair Schrödinger equation with $\boldsymbol{r}$ relative coordinate. $|\phi(\boldsymbol{0})|^2$ represents the probability to find the electron and hole pair within the same primitive cell: the probability to photoexcite such a pair is proportional to the overlap of the electron and hole wavefunctions[41]. To modelize the effect of a static electric field $\boldsymbol{F}||\boldsymbol{z}$ we consider the following time-independent Schrödinger equation:

$$\left(\frac{h^2}{2\mu}\nabla^2+|e|\boldsymbol{F}z+E\right)\phi(\boldsymbol{r})=0. \tag{8.5}$$

By separating variables, $\phi(\boldsymbol{r})=\phi(x,y)\phi(z)$, we get $E=E_{xy}+E_z$ with $\phi(x,y)=\frac{1}{2\pi h}e^{i(k_xx+k_yy)}$ and $E_{xy}=\frac{h^2(k_x^2+k_y^2)}{2\mu}$. In order to solve the monodimensional equation for the z component, that describes the relative motion of an electron-hole pair in a strong, uniform and static electric field F,

$$\left(\frac{h^2}{2\mu}\frac{\partial^2}{\partial z^2}+|e|Fz+E_z\right)\phi(z)=0, \tag{8.6}$$

we define $\xi=-\frac{E_z}{\sigma(F)}-z\left(\frac{2\mu|e|F}{h^2}\right)^{1/3}$ where $\sigma(F)=\left(\frac{e^2h^2F^2}{2\mu}\right)^{1/3}$ is the electro-optical energy. We can write $z=\left(-\xi-\frac{E_z}{\sigma(F)}\right)\left(\frac{h^2}{2\mu|e|F}\right)^{1/3}$, $\frac{d\xi}{dz}=-\left(\frac{2\mu|e|F}{h^2}\right)^{1/3}$ and $\frac{d\xi^2}{dz^2}\frac{d^2\phi(\xi)}{d\xi^2}=\left(\frac{2\mu|e|F}{h^2}\right)^{2/3}\frac{d^2\phi(\xi)}{d\xi^2}$. The following comes by substitution

$$\frac{h^2}{2\mu}\left(\frac{2\mu|e|F}{h^2}\right)^{\frac{2}{3}}\frac{d^2\phi(\xi)}{d\xi^2}=\left[-E_z-|e|F\left(-\xi-\frac{E_z}{\sigma(F)}\right)\left(\frac{h^2}{2\mu|e|F}\right)^{\frac{1}{3}}\right]\phi(\xi), \tag{8.7}$$

$$\sigma(F)\frac{d^2\phi(\xi)}{d\xi^2}=\left[-E_z-\sigma(F)\left(-\xi-\frac{E_z}{\sigma(F)}\right)\right]\phi(\xi), \tag{8.8}$$

$$\frac{d^2\phi(\xi)}{d\xi^2}=\phi(\xi). \tag{8.9}$$

The solution of this differential equation is the well-known Airy function $\phi(\xi)=Ai(\xi)$[194–196]. We now recall that the dipole matrix element P_{if} is proportional to $\phi(\boldsymbol{r}=\boldsymbol{0})$, thus $P_{if}\propto Ai\left(-\frac{E_z}{\sigma(F)}\right)$ and

$$\epsilon_i(\omega,F)\propto\frac{1}{\omega^2}\sum_{i<f}\sum_{\boldsymbol{k}}\left|Ai\left(-\frac{E_z}{\sigma(F)}\right)\right|^2\delta\left(E_f(\boldsymbol{k})-E_i(\boldsymbol{k})-h\nu\right). \tag{8.10}$$

The k-dependence is only for the x and y components and the energy variation depends only on E_z, so

$$\epsilon_i(\omega, F) \propto \frac{1}{\omega^2} \sum_{E_z} \sum_{k_x,k_y} \left| Ai\left(-\frac{E_z}{\sigma(F)}\right)\right|^2 \delta\left(E_{xy}(k_x,k_y) + E_z - h\nu\right), \tag{8.11}$$

where we have replaced $E_f(\boldsymbol{k}) - E_i(\boldsymbol{k}) = E = E_{xy} + E_z$. Now, by use of the density-of-states definition, $D(h\nu) = 2\sum_{\boldsymbol{k}} \delta(E(\boldsymbol{k}) - h\nu)$[1], and substitution of the sum over energy with an integral we get

$$\epsilon_i(\omega, F) \propto \frac{1}{\omega^2} \int dE_z \left| Ai\left(-\frac{E_z}{\sigma(F)}\right)\right|^2 D(h\nu - E_z). \tag{8.12}$$

If we perform a change of variable $g = -\frac{E_z}{\sigma(F)}$, $dg \propto dE_z$, and assume a step-like DOS, $D(h\nu - E_z) = constant\ if\ h\nu - E_z > E_G \leftrightarrow \frac{-E_z}{\sigma(F)} > \frac{E_G - h\nu}{\sigma(F)} \leftrightarrow g > g_0 = \frac{E_G - h\nu}{\sigma(F)}$, we're left with

$$\epsilon_i(\omega, F) \propto \frac{1}{\omega^2} \int_{g_0}^{\infty} |Ai(g)|^2 dg. \tag{8.13}$$

The real part of the dielectric function $\epsilon_r(\omega, F)$ can be obtained through the transformations of Kramers and Kroning: $\epsilon_r(\omega, F) = \frac{1}{\pi} P \int \frac{\epsilon_i(\omega', F)}{\omega' - \omega} d\omega'$ with P Cauchy's principal value. Exploiting the mathematical properties of the Airy function it's possible to write the field-induced variations of the optical properties of a square-root gap semiconductor in a more straightforward way[41]:

$$\Delta\epsilon_r(\omega, F) = \epsilon_r(\omega, F) - \epsilon_r(\omega, 0) \propto \frac{\sqrt{\sigma(F)}}{(h\nu)^2} \cdot G\left(\frac{E_G - h\nu}{\sigma(F)}\right), \tag{8.14}$$

$$\Delta\epsilon_i(\omega, F) = \epsilon_i(\omega, F) - \epsilon_i(\omega, 0) \propto \frac{\sqrt{\sigma(F)}}{(h\nu)^2} \cdot F\left(\frac{E_G - h\nu}{\sigma(F)}\right), \tag{8.15}$$

$$G(x) = \pi[Ai'(x)Bi'(x) - xAi(x)Bi(x)] + \sqrt{x}H(x), \tag{8.16}$$

$$F(x) = \pi[Ai'^2(x) - xAi^2(x)] - \sqrt{-x}H(-x), \tag{8.17}$$

with $Ai(x)$ the Airy function, $Bi(x)$ its modified form, $Ai'(x)$ and $Bi'(x)$ their derivatives and $H(x)$ the Heaviside step function

$$H(x) = \begin{cases} 1 \ \ if \ \ x \geq 0 \\ 0 \ \ if \ \ x < 0 \end{cases}. \tag{8.18}$$

As can be grasped by F' and G's plots in Fig.8.5a, this model predicts an oscillating behaviour of the optical properties at energies above the gap and an exponential tail below E_G (Fig.8.5b). It is important to note that the field-induced variations of the optical properties scale almost linearly with the applied field amplitude[203]. In a naive picture, the below gap field-induced opacity can be regarded as a photon-assisted tunnelling: the electrical field tilts the band spatially and softens the gap, thus the electrons tunnel from the valence to the conduction band through a field-dependent distance.

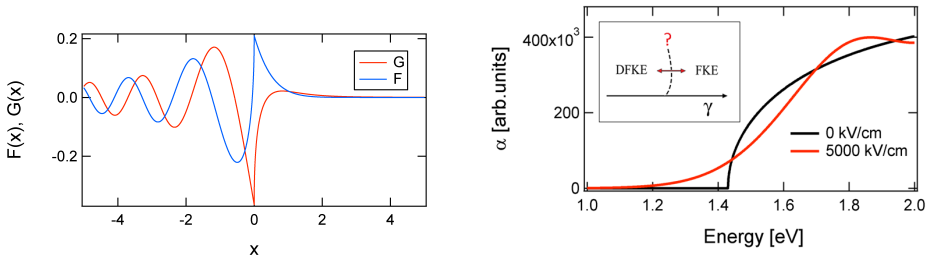

(a) *(b)*

Figure 8.5: a) F and G as functions of the adimensional variable $x = \frac{E_G - h\nu}{\sigma(F)}$. b) Static Franz-Keldysh effect. The unperturbed absorption edge of a semiconductor (black curve) displays, in a uniform electric field, below-gap absorption and above-gap oscillations (red curve). Insert: sketch of the static and dynamic Franz-Keldysh regime as a function of the parameter γ.

8.5.2 The effective field

The explicit form of the effective field in eq.8.3 is

$$F_{eff}(t,p) = \frac{0.02+p^4}{10^3} \int (|F(t'')| \frac{\frac{1}{t''}\int_0^{t''} |I(t')|^2 dt'}{1 + \frac{p^4}{1.2\cdot 10^{12}} \frac{1}{t''} \int_0^{t''} |I(t')|^4 dt'}) e^{-(t-t'')/(1+3p^2)} dt'', \tag{8.19}$$

hence

- $\alpha(p) = \frac{0.02+p^4}{10^3}$,
- $A(I^2(t)) = \frac{1}{t''}\int_0^{t''} |I(t')|^2 dt'$,
- $B(I^4(t)) = \frac{p^4}{1.2\cdot 10^{12}} \frac{1}{t''} \int_0^{t''} |I(t')|^4 dt'$,
- $g(p,t) = e^{-(t-t'')/(1+3p^2)}$.

Chapter 9

Concluding remarks

This thesis reports on ultra-fast pump-probe experiments for studying the quasi-equilibrium states of complex materials, in search of novel selective excitation mechanisms. We extensively used broadband pulses as probes and several pumping techniques. Among them, we generate THz pump pulses with the tilted-wavefront scheme (Ch.4). In order to extract significant physical quantities out of the broadband time-resolved reflectivity data, such as the time evolution of the specral weight of each optical band, we proposed two novel methodologies either founded on the Drude-Lorentz model and on the Kramers-Kronig relations (Ch.3).

By combining optical pumps and white light probes we identified a novel excitonic state in the Mott insulator YVO_3. Such Hubbard exciton has a kinetic-energy contribution, that we were able to measure for the first time. This result is particularly important to address the exotic physical phenomena of strongly correlated electrons systems: for example, a kinetic-energy based mechanism has been proposed for the condensation of the Cooper pairs in the cuprates[131].

We found exciting experimental evidences in the parent compound of the high temperature superconductors $La_{2-x}Sr_xCuO_4$. The pump pulses were tuned from $0.95\,eV$ to $3\,eV$, revealing a novel non-thermal dynamic of the charge-transfer (CT) gap. The CT gap seems to cool down following excitations at pump wavelengths which do not excite free quasi-particles. Such result can be rationalized in a localized vs. delocalized excitation mechanism, that stress the importance of the onsite *dd* transitions in the physics of the cuprates. Moreover, our measurements strongly suggest that a detailed review of many pump-probe experiments on HTSC might be carried on, as the pump effect should not be always treated as electronic heating.

The optical properties of the cuprates are strongly perturbed upon formation of the condensate at either very low frequencies, as in BCS systems, and optical ones[8]. We studied the interplay of the low and high energy scales by broadband probing the coherent phonon response in optimally doped YBCO. We revealed a novel wavelength dependence of the response of Ba and Cu off-

plane vibrations, and demonstrated that such coherent phonons may be used to identify the dynamics of the interband transitions involved in the formation of the superconducting phase.

FIR pumps have been extensively used to drive strongly correlated electrons systems into metastable non-thermal states and to manipulate the coherence of a superconducting state (see Ch.2). We adopted intense THz pump pulses in order to perform phase-sensitive measurements on the cuprates. As a mean to characterize this novel spectroscopic tool we used THz pump and broadband probe to study a mixed regime of electroabsorption (the Franz-Keldysh effect) in bulk GaAs where memory effects are surprisingly important. This result might be of relevance in gating optical devices.

Our work opens new perspectives in the study of the coherent manipulation of collective quantum states such as high temperature superconductivity. High energy photo-excitation is known to result in partial melting of the superconducting phase above a threshold fluence[16]; moreover a recent study on optimally doped YBCO[207] suggests that the superconducting phase is also destroyed as a consequence of below gap excitations, i.e. by pumping in the THz range. We performed preliminary measurements dedicated to understand the similarities and differences between the two excitation schemes: the results are shown in Fig.9.1. Ultra-short $\approx 800\,nm$ probe pulses were used in combination with either $800\,nm$ (Fig.9.1a) or THz (Fig.9.1b) pumps. It is evident that the optical properties are very weakly perturbed by the THz pulses. This is consistent with a time-resolved ARPES experiment[208] that suggests that quasi-particles are piled up in antinodal positions after optical pumping, and that such excess seems to be responsible for the variation of the optical properties in the visible range. Further studies are needed to verify the interesting scenario where excitation of different region of the k-space superconducting gap are differently coupled to the high energy response.

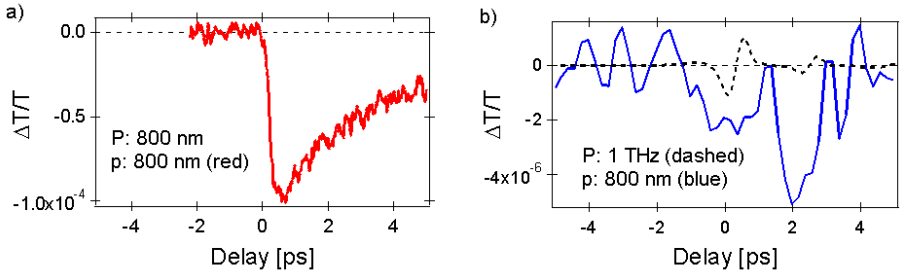

Figure 9.1: Time-resolved transmission measurements on optimally doped YBCO film at low temperature, performed with $800\,nm$ pump - $800\,nm$ probe (a), or THz pump - $800\,nm$ probe (b). In b), the THz field is shown as the dashed line in arbitrary units. "p" is the shorthand for probe, "P" for pump.

Bibliography

[1] G. Grosso and G. Pastori Parravicini. *Solid state physics.*

[2] A. Damascelli et al. *Rev. Mod. Phys.*, 75:473, 2003.

[3] A. Mann. *Nature*, 280:475, 2011.

[4] J. Zaanen. *arXiv:1012.5461*, 2011.

[5] F. Cilento. *Non-equilibrium phase diagram of BSCCO cuprate superconductors revealed by ultrafast optical spectroscopy, PhD thesis, Università degli studi di Trieste*, 2012.

[6] A. Kirilyuk A. Kimel and T. Rasing. *Rev. Mod. Phys.*, 82:2742, 2010.

[7] D.N. Basov et al. *Reviews of Modern Physics*, 83:471, 2011.

[8] M.R. Norman and C. Pepin. *Rep. Prog. Phys.*, 66:1547, 2003.

[9] E. Beaurepaire J.C. Merle A. Daunois and J.Y. Bigot. *Phys. Rev. Lett.*, 76:4250, 1996.

[10] Y. Tokura. *Physics Today*, 56(7):50, 2003.

[11] N. Gedik et al. *Science*, 316:425, 2007.

[12] H. Ehrke et al. *Phys. Rev. Lett.*, 106:217401, 2011.

[13] H. Ichikawa et al. *Nat. Mat.*, 10:101, 2011.

[14] A. Cavalleri et al. *Phys. Rev. Lett.*, 87:237401, 2001.

[15] L. Perfetti et al. *Phys. Rev. Lett.*, 97:067402, 2006.

[16] P. Kusar et al. *Phys. Rev. Lett.*, 101:227001, 2008.

[17] C. Giannetti et al. *Phys. Rev. B*, 79:224502, 2009.

[18] G. Coslovich et al. *Phys. Rev. B*, 83:064519, 2011.

[19] M. Rini et al. *Nature*, 449:72, 2007.

[20] R.I. Tobey et al. *Phys. Rev. Lett.*, 101:197404, 2008.

[21] D.N. Basov and T. Timusk. *Reviews of Modern Physics*, 77:721, 2005.

[22] K. McElroy et al. *Nature*, 442:592, 2003.

[23] P.A. Lee et al. *Rev. Mod. Phys.*, 78:17, 2006.

[24] P. Monthoux et al. *Nature*, 450:1177, 2007.

[25] T. Moriya and K. Ueda. *Rep. Prog. Phys.*, 66:1299, 2003.

[26] C. Giannetti et al. *Nat. Comm.*, 2:353, 2011.

[27] S. Dal Conte et al. *Science*, 335:1600, 2012.

[28] F. Carbone et al. *Proc. Natl. Acad.*, 51:20161, 2008.

[29] E.J. Nicol and J.P. Carbotte. *Phys. Rev. B*, 67:214506, 2003.

[30] N. Gedik et al. *Phys. Rev. Lett.*, 95:117005, 2005.

[31] G.P. Segre et al. *Phys. Rev. Lett.*, 13:137001, 2002.

[32] P.W. Anderson. *Science*, 317:1705, 2007.

[33] D. Fausti et al. *Science*, 331:189, 2011.

[34] D.N. Basov et al. *Phys. Rev. B*, 50:3511, 1994.

[35] S. Kaiser et al. *arxiv:1205.4661.*

[36] S. Hufner et al. *Rep. Prog. Phys.*, 71:062501, 2008.

[37] G. Baskaran. *arxiv:1211.4567v1*, 2012.

[38] A. Dienst et al. *Nature Photonics*, 5:485, 2011.

[39] H.J.A. Molegraaf C. Presura D. van der Marel P.H. Kes and M. Li. *Science*, 295:2239, 2002.

[40] F. Wooten. *Optical properties of solids, Academic press*, 1972.

[41] P. Y. Yu and M. Cardona. *Fundamentals of Semiconductors Physics and Materials Properties.*

[42] J. W. Allen and J. C. Mikkelsen. *Phys. Rev. B*, 15:2952, 1977.

[43] H. J. Kaufmann E. G. Maksimov and E. K. H. Salje. *Journal of Superconductivity*, 11:755, 1998.

[44] D. De Sousa et al. *J. Non Crystalline Sol.*, 352:769, 2006.

[45] S.A. MacDonald et al. *J. Non Crystalline Sol.*, 275:72, 2000.

[46] J. Tauc R. Grigorovici and A. Vancu. *Phys. Stat. Sol.*, 15:627, 1966.

[47] J. Reul et al. *Phys. Rev. B*, 86:125128, 2012.

[48] J.P. Falck A. Levy M.A. Kastner and R.J. Birgenau. *Phys. Rev. Lett.*, 69:1109, 1992.

[49] G.E. Jellison and F.A. Modine. *Appl. Phys. Lett.*, 69:371, 1996.

[50] G.E. Jellison and F.A. Modine. *Appl. Phys. Lett.*, 69:2137, 1996.

[51] P.F. Maldague. *Phys. Rev. B*, 16, 1977.

[52] D. Baeriswyl et al. *Phys. Rev. B*, 35, 1987.

[53] M.M. Qazilbash et al. *Nat. Phys.*, 5:647, 2009.

[54] S. Uchida et al. *Phys. Rev. B*, 43, 1991.

[55] B. Ferguson et al. *Nature Materials*, 1:26, 2002.

[56] H.B. Liu et al. *Proceedings of the IEEE*, 95:1514, 2007.

[57] M. Tonouchi. *Nature Photonics*, 1:97, 2007.

[58] A. Dobroiu et al. *Applied Optics 30*, 43:5637, 2004.

[59] S. Kumar et al. *Appl. Phys. Lett.*, 88:121123, 2006.

[60] J. Devenson et al. *Appl. Phys. Lett.*, 91:251102, 2007.

[61] Z. Jiang et al. *Appl. Phys. Lett.*, 72:16, 1998.

[62] *New Sources for Terahertz Research, Workshop, Trieste, Elettra laboratory, October 4-5 2012.*

[63] J.M. Byrd et al. *Phys. Rev. Lett.*, 96:164801, 2006.

[64] S. Bielawski et al. *Nat. Phys.*, 4:390, 2008.

[65] A.J. Taylor et al. *Optics Letters*, 18,16:1340, 1993.

[66] S. Sirbu. *Induced excitations in some metal oxides, PhD thesis, Zernike Institute, Groningen*, 2008.

[67] X.C. Zhang and J. Xu. *Introduction to THz Wave Photonics, Springer*, 2009.

[68] A. Nahata et al. *Appl. Phys. Lett.*, 69:16, 1996.

[69] W. Shi et al. *Opt. Lett.*, 27:16, 2002.

[70] K.L. Yeh et al. *Opt. Comm.*, 281:3567, 2008.

[71] A. Schneider et al. *J. Opt. Soc. Am. B*, 23:1822, 2006.

[72] E. Hecht. *Optics, Fourth edition, Addison Wesley, International edition.*

[73] J. Hebling et al. *Appl. Phys. B*, 78:593, 2004.

[74] J. Hebling et al. *J. Opt. Soc. Am. B*, 25:B6, 2008.

[75] H.J. Bakker et al. *J. Opt. Soc. Am. B*, 15:1795, 1998.

[76] T. Bartel et al. *Opt. Lett.*, 30:20, 2005.

[77] I. Wilke and S. Sengupta. *Nonlinear Optical Techniques for Terahertz Pulse Generation and DetectionŮOptical Rectification and Electrooptic Sampling, Rensselaer Polytechnic Institute.*

[78] A. Segura. *Phys. Rev. B*, 56:7, 1997.

[79] A. S. Barker and R. Loudon. *Phys. Rev. B*, 158:443, 1967.

[80] C. Thierfelder. *Phys. Status Solidi C*, 7:362, 2010.

[81] E.D. Palik. *Handbook Of Optical Constants Of Solids*, 1998.

[82] M. Walther et al. *Opt. Lett.*, 25:12, 2000.

[83] K. Jagannathan and S. Kalainathan. *Materials Research Bulletin*, 42:1881, 2007.

[84] D. J. Cook and R. M. Hochstrasser. *Opt. Lett.*, 25:1210, 2000.

[85] M. Kress T. Löffler S. Eden M. Thomson and H.G. Roskos. *Opt. Lett.*, 29:1120, 2004.

[86] T. Löffler M. Kress M. Thomson and H.G. Roskos. *ACTA PHYSICA POLONICA A*, 1, 2004.

[87] N. Dean. *Electronic and Structural Dynamics of Complex Material, PhD Thesis, Jesus College, Oxford*, 2011.

[88] L. Pálfalvi et al. *J. Appl. Phys.*, 95:902, 2004.

[89] Zs. Bor and B. Rácz. *Optics Communications*, 54:165, 1985.

[90] J. Hebling et al. *Optical and Quantum Electronics*, 28:1759, 1996.

[91] A.G. Stepanov et al. *Appl. Phys. Lett.*, 2003.

[92] M.C. Hoffmann et al. *Opt. Expr.*, 2007.

[93] A.G. Stepanov et al. *Opt. Expr.*, 2005.

[94] M.C. Beard et al. *Phys. Rev. B*, 62:15764, 2000.

[95] M.C. Beard et al. *Journal of Applied Physics*, 90:5915, 2001.

[96] M.C. Hoffmann et al. *J. Opt. Soc. Am. B*, 26:A29, 2009.

[97] R.D. Averitt et al. *J. Opt. Soc. Am. B*, 17:327, 2000.

[98] J. Kitagawa et al. *J. Phys. Condens. Matter*, 19:406224, 2007.

[99] J.T. Kindt et al. *Journal of Chemical Physics*, 110:8589, 1999.

[100] G.M. Turner et al. *J. Phys. Chem. B*, 106:11716, 2002.

[101] P. Kuzel et al. *Journal of Chemical Physics*, 127:024506, 2007.

[102] C. Nagura et al. *Appl. Opt.*, 41:18, 2002.

[103] R.W. Boyd. *Nonlinear Optics, Third edition, Academic Press*, 2007.

[104] F. Cilento et al. *Appl. Phys. Lett.*, 96:021102, 2010.

[105] A. Damascelli et al. *Phys. Rev. B*, 61:18, 2000.

[106] M. Hase et al. *Phys. Rev. Lett.*, 70:3651, 1993.

[107] J.P. Boucher and L.P. Regnault. *J. Phys. I France*, 6:1939, 1996.

[108] P.H.M. van Loosdrecht et al. *Phys. Rev. B*, 54:6, 1996.

[109] P.H.M. van Loosdrecht et al. *Phys. Rev. Lett.*, 76:2, 1996.

[110] D. Fausti. *Dinamiche elettroniche di superficie, Tesi di laurea, Università Cattolica, Brescia*, 2002.

[111] F. Giusti. *Studio dell'effetto Franz-Keldysh tramite tecniche spettroscopiche nel dominio dei tempi in GaAs, Tesi triennale, Università degli studi di Trieste*, 2012.

[112] G. Coslovich. *Disclosing the ultrafast dynamics of competing phases in high-temperature superconductors by time-resolved optical spectroscopy, PhD thesis, Università degli studi di Trieste*, 2011.

[113] M. Imada A. Fujimori and Y. Tokura. *Rev. Mod. Phys*, 70:1039, 1998.

[114] A. Fujimori and Y. Tokura. Spectroscopy of mott insulators and correlated metals. 1994.

[115] J. van den Brink M.B.J. Meinders J. Lorenzana R. Eder and G.A. Sawatzky. *Phys. Rev. Lett.*, 75:25, 1995.

[116] R. Neudert et al. *Phys. Rev. Lett.*, 81:657, 1998.

[117] A. Hubsch J. Richter C.Waidacher K.W. Becker and W. vonderLinden. *Phys. Rev. B*, 63:205103, 2001.

[118] S. Wall et al. *Nat. Phys.*, 7:114, 2011.

[119] R. G. Leigh and P. Phillips. *Phys. Rev. B*, 79:245120, 2009.

[120] F.H.L. Essler F. Gebhard and E. Jeckelmann. *Phys. Rev. B*, 64:125119, 2001.

[121] H. Matsueda T. Tohyama and S. Maekawa. *Phys. Rev. B*, 71:153106, 2005.

[122] A. Gössling et al. *Phys. Rev. B*, 78:075122, 2008.

[123] Y. Matiks P. Horsch R.K. Kremer B. Keimer and A.V. Boris. *Phys. Rev. Lett.*, 103:187401, 2009.

[124] F.B. Gallagher and S. Mazumdar. *Phys. Rev. B*, 56:15025, 1997.

[125] E. Jeckelmann. *Phys. Rev. B*, 67:075106, 2003.

[126] F.C. Zhang and K.K. Ng. *Phys. Rev. B*, 58:13520, 1998.

[127] D.G. Clarke. *Phys. Rev. B*, 48:7520, 1993.

[128] P. Wrobel and R. Eder. *Phys. Rev. B*, 66:035111, 2002.

[129] Y.Y. Wang et al. *Phys. Rev. Lett.*, 77:1809, 1996.

[130] E. Collart A. Shukla J.P. Rueff P. Leininger H. Ishii I. Jarrige Y.Q. Cai S.W. Cheong and G. Dhalenne. *Phys. Rev. Lett.*, 96:157004, 2006.

[131] J.E. Hirsch. *Science*, 295:2226, 2002.

[132] P. Phillips. *Rev. Mod. Phys.*, 82:1719, 2010.

[133] Y. Ren et al. *Nature*, 396:441, 1998.

[134] G.R. Blake T.T.M. Palstra Y. Ren A.A. Nugroho and A.A. Menovsky. *Phys. Rev. B*, 65:174112, 2002.

[135] C. Ulrich et al. *Phys. Rev. Lett.*, 91:257202, 2003.

[136] M. Noguchi et al. *Phys. Rev. B*, 62:R9271, 2000.

[137] H.F. Pen et al. *Phys. Rev. B*, 59:7422, 1999.

[138] A.A. Tsvetkov et al. *Phys. Rev. B*, 69:075110, 2004.

[139] M. Reehuis et al. *Phys. Rev. B*, 73:094440, 2006.

[140] T.A.W. Beale et al. *Phys. Rev. B*, 82:024105, 2010.

[141] H. Sawada N. Hamada K. Terakura and T. Asada. *Phys. Rev. B*, 53:12742, 1996.

[142] Z. Fang and N. Nagaosa. *Phys. Rev. Lett.*, 93:176404, 2004.

[143] Z. Fang N. Nagaosa and K. Terakura. *Phys. Rev. B*, 67:035101, 2003.

[144] M. DeRaychaudhury E. Pavarini and O.K. Andersen. *Phys. Rev. Lett.*, 99:126402, 2007.

[145] R.J.O. Mossanek and M. Abbate. *Phys. Rev. B*, 76:035101, 2007.

[146] R.J.O. Mossanek et al. *Phys. Rev. B*, 80:195107, 2009.

[147] Y. Otsuka and M. Imada. *J. Phys. Soc. Jpn.*, 75:124707, 2006.

[148] S. Miyasaka Y. Okimoto and Y. Tokura. *J. Phys. Soc. Jap.*, 71:2086, 2002.

[149] G. Khaliullin P. Horsch and A.M. Oles. *Phys. Rev. B*, 70:195103, 2004.

[150] A.M. Oles G. Khaliullin P. Horsch and L.F. Feiner. *Phys. Rev. B*, 72:214431, 2005.

[151] D.A. Mazurenko et al. *Phys. Rev. Lett.*, 101:245702, 2008.

[152] R.V. Yusupov D. Mihailovic C.V. Colin G.R. Blake and T.T.M. Palstra. *Phys. Rev. B*, 81:075103, 2010.

[153] S.K. O'Leary and P.K. Lim. *Solid State Comm.*, 104:17, 1997.

[154] H. Weihe and U. Güdel. *Inorg. Chem.*, 36:3632, 1997.

[155] C. Marquina M. Sikora M.R. Ibarra A.A. Nugroho and T.T.M. Palstra. *Journal of Magnetism and Magnetic Materials*, 290:428, 2005.

[156] J. Orenstein. *Physics Today*, Sept. 2012.

[157] M. Reehuis et al. *Phys. Rev. B*, 73:144513, 2006.

[158] M.A. Kastner and R.J. Birgeneau. *Reviews of Modern Physics*, 70:897, 1998.

[159] J.D. Perkins et al. *Phys. Rev. B*, 71:1621, 1993.

[160] J.D. Perkins et al. *Phys. Rev. B*, 52:9863(R), 1995.

[161] J.D. Perkins et al. *Phys. Rev. B*, 58:9390, 1998.

[162] J. Lorenzana and G.A. Sawatzky. *Phys. Rev. Lett.*, 74:1867, 2005.

[163] Y. Tokura K. Kikuchi T. Arima and S. Uchida. *Phys. Rev. B*, 45:7580, 1992.

[164] D.S. Ellis et al. *Phys. Rev. B*, 77:060501R, 2008.

[165] O. Rösch. *Phys. Rev. Lett.*, 95:227002, 2005.

[166] F. Novelli et al. *Phys. Rev. B*, 86:165135, 2012.

[167] J.R. McBride L.R. Miller and W.H. Weber. *Phys. Rev. B*, 49:12224, 1994.

[168] H. Okamoto et al. *Phys. Rev. B*, 82:060513(R), 2010.

[169] H. Okamoto et al. *Phys. Rev. B*, 83:125102, 2011.

[170] K. Matsuda et al. *Phys. Rev. B*, 50:4097, 1994.

[171] Y.H. Kim et al. *Phys. Rev. B*, 36:7252R, 1987.

[172] J.M. Ginder et al. *Phys. Rev. B*, 37:7506, 1988.

[173] G. De Filippis et al. *Phys. Rev. Lett.*, 109:176402, 2012.

[174] G.L. Eesley J. Heremans M.S. Meyer and G.L. Doll. *Phys. Rev. Lett.*, 65:3445, 1990.

[175] O.V. Misochko N. Georgiev T. Dekorsy and M. Helm. *Phys. Rev. Lett.*, 89:067002, 2002.

[176] W. Albrecht Th. Kruse and H. Kurz. *Phys. Rev. Lett.*, 69:1451, 1992.

[177] R. Henn T. Strach E. Schonherr and M. Cardona. *Phys. Rev. B*, 55:3285, 1997.

[178] O.V. Misochko et al. *Phys. Rev. B*, 59:11495, 1999.

[179] H. Takahashi et al. *Sol. State Comm.*, 149:1955, 2009.

[180] H.J. Zeiger et al. *Phys. Rev. B*, 45:768, 1992.

[181] I.I. Mazin et al. *Phys. Rev. B*, 49:9210, 1994.

[182] O.V. Misochko K. Kisoda K. Sakai and S.Nakashima. *Phys. Rev. B*, 61:4305, 2000.

[183] A.I. Lobad and A.J.Taylor. *Phys. Rev. B*, 64:180301(R), 2001.

[184] B. Friedl et al. *Solid State Comm.*, 78:291, 1991.

[185] A. Mascarenhas et al. *Phys. Rev. B*, 39:4699, 1989.

[186] F. Slakey et al. *Phys. Rev. B*, 39:2781, 1989.

[187] A.P. Schnyder D. Manske and A. Avella. *Phys. Rev. B*, 84:214513, 2011.

[188] A. Mysyrowicz et al. *Phys. Rev. Lett.*, 56:2748, 1986.

[189] A. Rundquist et al. *Science*, 280:1412, 1998.

[190] T.E. Glover R.W. Schoenlein A.H. Chin and C.V. Shank. *Phys. Rev. Lett.*, 76:2468, 1996.

[191] A.D. Jameson et al. *Appl. Rev. Lett.*, 95:201107, 2009.

[192] K.B. Nordstrom et al. *Phys. Rev. Lett.*, 81:457, 1998.

[193] A. Srivastava R. Srivastava J. Wang and J. Kono. *Phys. Rev. Lett.*, 93:157401, 2004.

[194] K. Tharmalingam. *Phys. Rev.*, 130:2204, 1963.

[195] D.E. Aspnes. *Phys. Rev.*, 147:554, 1966.

[196] D.E. Aspnes. *Phys. Rev.*, 153:972, 1967.

[197] W. Franz. *Z. Naturforsch*, 13a:484, 1958.

[198] W.L. Keldysh. *Zh. Eksperim. i Teor. Fiz.*, 34:1138, 1958.

[199] A. P. Jauho and K. Johnsen. *Phys. Rev. Lett*, 76:4576, 1996.

[200] Y. Yacoby. *Phys. Rev.*, 169:610, 1968.

[201] A.H. Chin J.M. Bakker and J. Kono. *Phys. Rev. Lett.*, 85:3293, 2000.

[202] K. Shinokita et al. *Appl. Rev. Lett.*, 97:211902, 2010.

[203] B.O. Seraphin and N. Bottka. *Phys. Rev.*, 139:A560, 1965.

[204] H. Bekkar F. Benamira and M. Maamache. *Phys. Rev. A*, 68:016101, 2003.

[205] M. Feng. *Phys. Rev. A*, 64:034101, 2001.

[206] M.V. Berry and N.L. Balazs. *Am. J. Phys.*, 47:264, 1979.

[207] A. Glossner et al. *arxiv:1205.1684v1*, 2012.

[208] R. Cortés et al. *Phys. Rev. Lett.*, 107:097002, 2011.

List of publications

- ***Ultrafast optical spectroscopy of the lowest energy excitations in the Mott insulator compound YVO_3: Evidence for Hubbard-type excitons***

  Authors: Fabio Novelli, Daniele Fausti, Julia Reul, Federico Cilento, Paul H. M. van Loosdrecht, Agung A. Nugroho, Thomas T. M. Palstra, Markus Grüninger, and Fulvio Parmigiani

  Phys. Rev. B 86, 165135, Published 31 October 2012

- ***Mixed regime of light-matter interaction revealed by phase sensitive measurements of the dynamical Franz-Keldysh effect***

  Authors: Fabio Novelli, Daniele Fausti, Francesca Giusti, Fulvio Parmigiani, and Matthias Hoffmann

  Scientific Reports 3, 1227, Published 6 February 2013

- ***Non-thermal charge-transfer dynamics in La_2CuO_4 after ultrafast selective excitation***

  Authors: Fabio Novelli et al.

  in preparation

- ***Coherent phonons in superconducting $YBa_2Cu_3O_{7-\delta}$***

  Authors: Fabio Novelli et al.

  in preparation